FACULTY OF SCIENCE
UNIVERSITY OF COPENHAGEN

Master Thesis

Kasper Elm Heintz

Exploring New Methods of Selecting Quasars

Dark Cosmology Centre - The Niels Bohr Institute

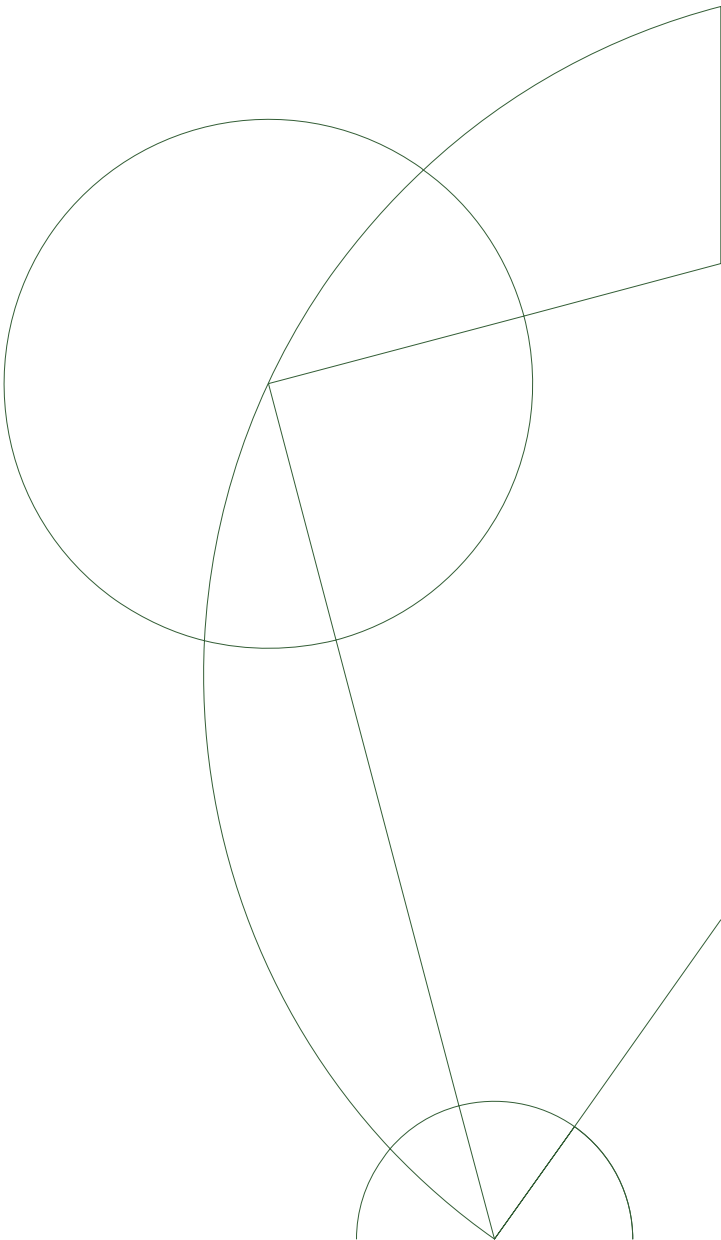

Supervisor: Johan P. U. Fynbo

August 26, 2016

Abstract

About 50 years ago, in the early 1960's, it was discovered that some galaxies harbored an active nuclei, systems in which the light observed was not originating from the stellar population of the galaxy but from the inner most region. The energy source is gravitational potential energy released from matter falling onto super massive black holes located in the galaxy centres. The most luminous of these active galactic nuclei obtained the name of quasi-stellar radio sources (quasars for short) due to their optical stellar-like morphology and the emitting radio lobes of which these were first detected. After this discovery, the focus has been on further classifying this peculiar type of object and although more than a hundred thousand sources have been observed to this day still more and more are being classified, some more spectacular than the other. Due to the complex nature of quasars it has so far been impossible to account for all the various sub-types, which is required to have a full understanding of the true nature and the cosmic evolution of quasars.

As an attempt of further illuminating parts of these issues in modern day astrophysics this thesis aims at exploring the incompleteness of current quasar samples. Most quasars are selected using methods that rely on photometric properties of the sources, e.g., the high UV excess of quasars compared to that of stars. This implies biases in the selection whereby some quasars evade selection in large photometric surveys and are hence underrepresented in the samples. Two well-known examples are quasars reddened by dust in the host galaxies harboring the active galactic nuclei or quasars reddened by dust-rich, intervening galaxies in the line-of-sight to the background source.

Acknowledgements

First of all I would like to thank my Master thesis project supervisor, Johan, for being very helpful and supportive in this academic quest. Without his excellent supervision, guidance and our weekly (sometimes daily) discussions, the road to get here would have been a lot more tedious. Thanks for giving me the opportunity to pursue my dream of working in astronomy - for that I am ever grateful.

Then a huge thanks goes to the fellow astronomers at DARK for creating such an inspiring work place. I would also like to thank Palle Møller for hosting me a week at ESO headquarters, showing me that astronomy do exists outside of DARK, and Stefan Geier with his great assistance on my first solo observing run. Also, thanks to the co-authors for the great discussions regarding the formulation and presentation of my first-author papers.

Finally I would like to thank my ever supporting family: my parents for always being there for me and my girlfriend Julie for always encouraging me and believing in me. Thanks for allowing me to work on this project at crazy times during the day and night, even with our newborn son, Oliver. Without you none of this would have been possible.

Contents

Chapter 1

Introduction

Since the discovery of quasi-stellar radio sources/objects (more commonly referred to as quasars or QSOs) some 50 years ago, the selection of these have been of great importance. As the name indicates, these objects appear to be of stellar origin but the nature of these is quite the contrary. In fact, quasars are some of the most luminous extragalactic objects known to this day. Quasars have been discovered and observed out to extreme cosmological distances merely 0.8 Gyr after the Big Bang (at redshift, $z = 7.085$; Momjian et al., 2014). Great effort has already been put into the selection of these bright and powerful objects both due to their own physically interesting nature but also due to the applications of these as cosmic probes. When specifically trying to target and examine the full population of quasars, great caution has to be applied in order to not distort the general view on these luminous objects. There are basically three approaches to limit the bias induced by different selection effects and thereby obtaining the underlying complete sample. The first is to simply select all objects within the magnitude limit of a given survey, which of course will be complete but impossible to follow-up spectroscopically due the large number of contaminants. The second is to detect the missing sub-population of quasars, which are not discovered by existing quasar surveys, to account for the total population by adding these two. The third is to produce new selection techniques that are less biased (or biased in another way) than the present approaches.

In this thesis I focus on the missing sub-population of quasars. The thesis is structered as follows: After this introduction describing the history of quasar detection and selection I in Chapter 2 focus on a my work on the selection of red quasars. In three appendices I include three papers I have authored in the course of my master study. These papers are:

- Heintz et al., 2016, AJ, 152, 13: Serendipitous Discovery of a Projected Pair of QSOs Separated by 4.5 arcsec on the Sky (Appendix A).

- Heintz et al., 2016, accepted for publication in A&A (Appendix B).

- Heintz et al., 2015, A&A, 578, A91: A study of purely astrometric selection of extragalactic point sources with Gaia (Appendix C).

In the introduction I will also briefly describe the main results of these in the context of quasar selection. As my introduction to the topic of this thesis I will in this chapter describe the characteristics of quasars by chronologically outlining the order and technique of which most of these have been discovered. By doing so, the nature of these objects will be understood concurrently. Throughout this thesis I will assume a standard ΛCDM cosmology with $H_0 = 70$ km s^{-1} Mpc^{-1}, $\Omega_M = 0.3$ and $\Omega_\Lambda = 0.7$.

1.1 The Discovery of Quasars

In the beginning of the 1960s, about 40 years after the discovery that the spirals and other nebulae are located outside our local Galactic system (Hubble, 1925), a new class of extragalactic objects were identified. The first quasi-stellar radio sources, or *quasars* for short, were detected by realizing that the luminous radio sources `3C-273, 3C-48, 3C-47` and `3C-147`, had spatial unresolved optical counterparts (Schmidt, 1963; Greenstein & Matthews, 1963; Schmidt & Matthews, 1964) and thus appeared to be of stellar origin (quasi-stellar). Specifically, the first quasar with a spectroscopic redshift measurement (`3C-273`) is an optical stellar-like object of thirteenth magnitude showing a faint wisp or jet extending beyond the optical counterpart. The spectral energy distributions (SEDs) of these first quasars were non-stellar as well. By adopting the extragalactic origin of this object, the visible emission lines in the SED could be explained by being coinciding with the expected Balmer lines for an object at $z = 0.158$ (assuming $v = H \cdot d = z \cdot c, \quad z = \lambda_{\rm obs}/\lambda_{\rm em} - 1$). The other objects were found to be at moderate redshifts as well, ranging between $z = 0.16 - 0.55$. The intrinsic luminosities for the optical counterparts of the two radio sources `3C-47` and `3C-147` were furthermore found to be greater than those of the brightest galaxies known at the time. In addition, the optical properties of all of these four objects were in many ways similar to each other, which further indicates that they belonged to the same, new class of extragalactic, astrophysical objects.

Following these discoveries, Sandage (1965) found that there were many other objects with the same optical properties as the four radio sources but showed no signs of radio emission, i.e., were "radio-quiet". These quasi-stellar objects (QSOs) were examined to have a large ultraviolet (UV) flux and most have strong, broad emission lines as well. A few years later the discovery of this new class of objects were further validated by the study of Arp et al. (1968) and Sargent (1970), identifying multiple objects with the same optical properties and blue (high UV flux) colors in existing catalogs of compact galaxies. These two techniques of identifying QSOs have now set the standard of building large samples, extending the number of known QSOs, to gain further knowledge about the physical nature of these objects.

The Central Engine Powering the AGN

It is now widely believed that indeed these two types of objects, with and without radio emission, have the same origin. Previously, numerous sub-populations, e.g., Seyferts 1 and 2, quasars and QSOs were used to classify objects in terms of their observed properties, with QSOs historically being the most luminous. However, it appear that all of these subgroups seem to have one thing in common; they are all active galactic nuclei (AGN). The energy output from this central region of the galaxy has shown to be enormous so the mechanism of the central engine has to explain this large generation of energy. The idea, originally proposed by Salpeter (1964) and Lynden-Bell (1969), which is now generally accepted, is that this central engine is a supermassive black hole (SMBH) accreting gas and that the energy source is the gravitational potential of the central black hole (see e.g., Peterson, 1997; Mo et al., 2010, for two excellent textbooks on active galactic nuclei and galaxy formation and evolution in general, respectively).

By monitoring stellar orbits around Sgr A* it has been firmly established that a SMBH is located in the centre of the Milky Way (Gillessen et al., 2009). It is now widely believed that all galaxies harbor SMBHs, which may or may not be active in accreting gas from the surrounding material (as is the case for quasars).

In the standard unified AGN model AGN consists of multiple components. In the inner most parts, in the core of the AGN, is the black hole and the surrounding accretion disk fuelling the AGN. In the proximity of this, the broad line region (BLR) is located and surrounding that

is the torus and the narrow line region (NLR). A visual example of this is given in Fig. 1.1, where the different components are shown together with a measure of the relative sizes of each of these. In the unified AGN model all the sub-populations of AGN belong to the same class of objects but are observed at different viewing angles (i.e., the emission from Seyfert 1 and 2 are dominated by the broad and narrow line regions, respectively). The two jets ejected in opposite directions from the central black hole, most likely along the rotation axis, produce the radio lobes used to first identify quasars as mentioned above. The emission from these jets come from relativistic electrons spiraling in a magnetic field and when these charged particles are accelerated they radiate photons at a broad range of wavelengths including radio (this effect is known as synchrotron radiation; Peterson, 1997; Mo et al., 2010).

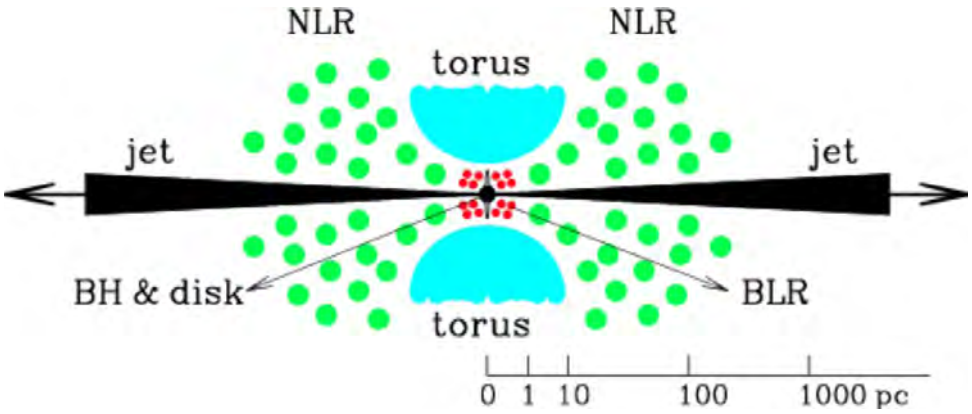

Figure 1.1: The standard model for the different components of an AGN. This figure is from Mo et al. (2010).

QSOs have very broad SEDs often ranging from radio to gamma-ray wavelengths. The spectra can approximately be described by a power law, $F_\nu \propto \nu^{-\alpha}$, with $0 < \alpha < 1$. The broad wavelength range of energy observed in the spectra of AGN suggest that a variety of emission mechanisms are involved (Mo et al., 2010). Describing all of these is beyond the scope of this thesis but I will conclude this section by briefly describing the shape of the SED since this is important in order to understand the UV/optical spectra. Basically, there are several contributors to the UV through the optical and infrared continuum. It has been shown that a model with a combination of a cool thermal spectrum in the infrared in addition to an accretion disk spectrum in the optical can successfully model the broad spectral range of QSOs (see e.g., Peterson, 1997, and references therein). Finally, it is important to note that the large UV excess (UVX) of QSOs should be understood as relative to that of stars. Selection based on the UVX is therefore primarily a manifestation of the power law SEDs of QSOs compared to the standard blackbody SEDs of stars.

1.2 Description of Selection Techniques

Following up on the timeline, a few years after the discovery of the similar optical properties and blue colors of QSOs, Sandage (1971) realized that these objects deviated from the standard, main-sequence stellar "track" in optical UBV color-color diagrams. That is, since stellar types (O to M main-sequence stars) have well-defined blackbody SEDs with shapes depending on the temperature, these will follow a track in optical/near-infrared color-color space. By design, QSOs will then separate from this track due to their relative blue colors (i.e., $U - B < 0$). Specifically, candidate QSOs can be selected from a single color criterion demonstrated by

Schmidt & Green (1983) where the QSO candidates from their sample were selected from digitized photographic plates according to the criterion $U - B < -0.44$. One of the first large scale studies of selection based on the UVX of spatially unresolved objects was done by Green et al. (1986). They, however, experienced severe contamination from Galactic stars and only about 9% of the observed objects were found to be of extragalactic origin (of which 5.4% are QSOs). In the study by Koo & Kron (1988) they further reevaluated how to construct optical color ratios that select extragalactic objects more effectively.

By simultaneously realizing that the infrared part of the spectra of QSOs primarily traces the hot torus surrounding the SMBH, Low & Kleinmann (1968) discuss the possibility of using infrared only selection techniques when targeting QSOs. At the time, however, these were not well understood and some twenty years had to pass for this technique to gain prevalence. de Grijp et al. (1987) executed the first large-scale attempt to find AGNs in the infrared based on the data from the Infrared Astronomical Satellite (IRAS). They showed that a blue (warm) 60 to 25 μm infrared color provides a powerful parameter for discriminating between "normal" galaxies and galaxies with AGNs. Ten years earlier, in the end of the 1970s, Usher & Mitchell (1978) used variability as another survey technique due to the fact that QSOs often show variability in the emitted flux. In the following two years, Wilson (1979) and Ward et al. (1980) found X-ray sources with seemingly Seyfert like nuclei. This further validated the standard model of AGNs, since X-ray emission is expected from the inner most part of the accretion disk. Around the same time an inverse approach of selecting QSOs was investigated as well. Instead of searching for objects of a specific type, Hewett et al. (1984) described an automated system to measure and analyze large numbers of objective prism spectra from photographic plates using the Automated Plate Measuring (APM) facility. The system is being applied in a number of ways including automated QSO detection simply focusing on peculiar objects compared to the distinguishable shape of stars. In particular, this technique is good a identifying objects with strong emission and/or absorption lines. In Osmer & Hewett (1991) this same approach as a survey technique is used.

The final selection technique I will describe in this section is the approach of selecting QSOs based on their excess in the near-infrared K-band compared to that of stars (dubbed KX - by analogy with the UVX method). This method was originally presented in Warren et al. (2000) where it is shown that most QSOs not only show excess in the UV part of the spectrum but also at near-infrared wavelengths. An example of this is shown in Fig. 1.2 where the same kind of visualization can be applied for the UVX technique. Authors of some of the first papers related to the study of QSOs based on the UVX selection often discuss the unbiased nature of this selection. However, the UV/optical part of the spectrum is the most sensitive to dust reddening. Dust can be located either intrinsically in the QSO itself or in intervening clouds along the line-of-sight (which can e.g. appear as damped Lyα absorption features in the spectra of QSOs and these clouds are thus dubbed damped Lyα absorption systems (DLAs), see e.g., Wolfe et al., 2005, for a review). Both types of systems have been found to redden the spectra of QSOs, absorbing a significant fraction of the UV and optical flux from the intrinsically emitting source. These dust-reddened QSOs will then not appear as objects with large UVX and will thereby not be selected by this approach. Furthermore, a more technical problem arises in the UVX selection. At redshifts around $2.2 < z < 3.5$, which constitute a sort of redshift dessert for AGN, the strong Lyα emission line will coincide with the optical B- (or g-)bands thereby removing the observed UV excess (since the $U - B$ colors will be "redder" when large flux is observed in the B- (or g-)band compared to the U-band). At redshifts $z > 4$ the Lyα forest (LyαF) will appear in the U-band as well, with similar effect on the observed optical colors of QSOs. None of these problems arise in the KX selection technique since the near-infrared part of the spectrum will not be as heavily influenced by dust extinction and there will be no effect

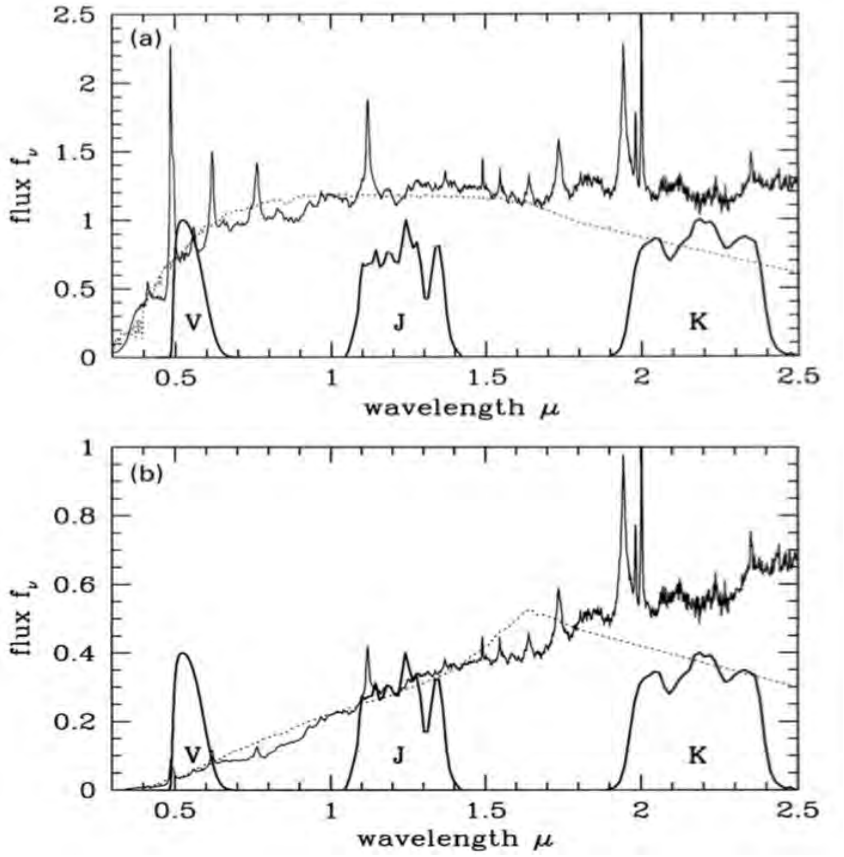

Figure 1.2: Comparison of optical/near-infrared SEDs of stars and QSOs. Each plot show a composite QSO spectrum (solid line) and a star with similar optical $V - J$ colors (dotted line). The upper panel shows the spectra of an unreddened $z = 3$ QSO and an early K star. The lower panel shows the same QSO with extinction and an early M star. In both cases a substantial K-band excess is apparent. From Warren et al. (2000).

of the LyαF.

1.3 Building Large Area Surveys

The first attempts at defining selection techniques have now set the standard of building large area surveys designed to detect much larger samples of QSOs. The main focus, common for all of these surveys, is to efficiently reject Galactic stars since these highly outnumber the sky density of QSOs at bright magnitudes. Otherwise, severe contamination will result when spectroscopically observing the candidates. Some of the following techniques are therefore not specifically designed for a completely unbiased identification of QSOs rather than effectively rejecting the stellar contamination. During the first few years of this millennium large area optical surveys such as the Two Degree Field (2dF; Boyle et al., 2001) and the Sloan Digital Sky Survey (SDSS; York et al., 2000) have been executed. Variations of the UVX technique was adopted by both of these extensive surveys where the 2dF Redshift Survey (2QZ; Croom et al., 2004) utilized a two-color $ubjr$ criterion whereas the SDSS programme based their selection on optical $ugriz$ five-band colors of QSOs (Fan, 1999; Richards et al., 2001, 2002). In particular, the approach of the SDSS was to model a well-defined stellar track in the five-band optical color space from which QSOs could be identified based on their differences in colors compared to stars.

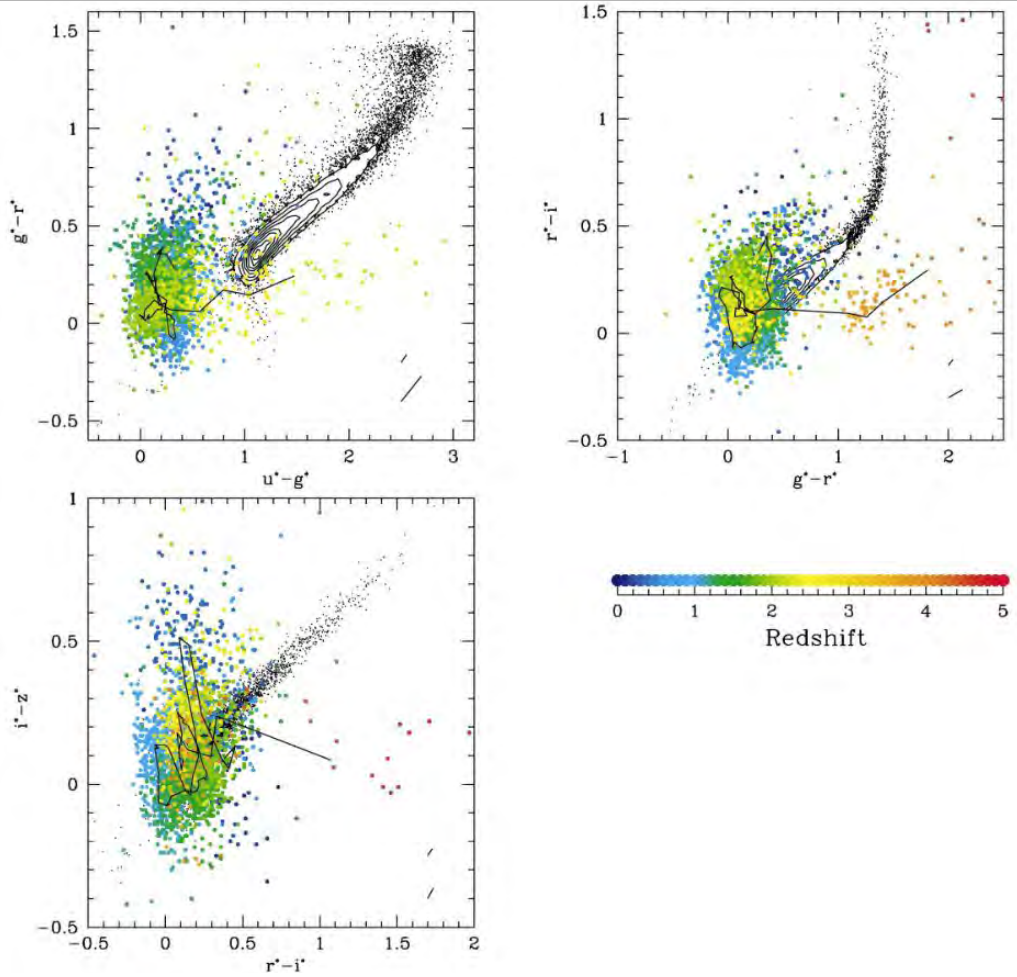

Figure 1.3: Optical five-band color-color plots of 2625 SDSS QSOs (color coded points as function of redshift) and 10,000 stars (black points and contours). The stellar track is clearly illustrated together with the general UV excess of QSOs (e.g., the first *ugr* color-color diagram). This figure is adapted from Richards et al. (2001).

In Fig. 1.3 three optical color-color diagrams from Richards et al. (2001) are shown, illustrating their approach. The stellar track and the general UVX of the SDSS QSOs are clearly seen. Although somewhat separated in the *ugr* color-color diagram, the QSOs begin to overlap with the stellar locus in the *gri* and *riz* colors. The colors of QSOs at redshift $2.2 < z < 3.5$ coincide with the stellar track even in the *ugr* color-color diagram illustrating the disadvantage of the UVX in that redshift range. It can be concluded that even though the stellar track can be well defined in the five-band optical colors, the QSOs are not that easily distinguished from stars. Furthermore, it is important to remember that the selection of these QSOs primarily were based on the UVX criteria, so objects experiencing dust reddening will not appear in these diagrams (more precisely these dust-reddened QSOs will in general overlap even more with the stellar locus - this issue will be further discussed in Chapter 2). Thus, a clear bias against dust-rich QSO systems is to be expected using this technique.

Around the same time, Salzer et al. (2000) applied the slitless spectroscopy technique for the Kitt Peak National Observatory International Spectroscopic Survey (KISS). While this survey does not have any false detections, since the emission line signatures are easily distinguishable on the CCD frames, the completeness of this technique is not very high. First of all, it is hard to

evaluate the actual completeness since the lines observed in the optical depend on the redshifts of the objects and the intrinsic strength of each of these lines can vary. Furthermore, in the last decade numerous obscured QSOs have been detected with few to no appearing emission lines, and such objects will be missed with this approach. Subsequently, Brunzendorf & Meusinger (2001, 2002) and Meusinger et al. (2003) used the technique of observing the variability of QSOs over longer periods of time. Even though this process is long term compared to the other, Veron & Hawkins (1995) have shown that on long enough timescales all AGN are variable thereby making this selection close to being complete down to the flux limits of the survey.

Also in the first few years of this millennium, the search for radio-loud quasars was refined as well. In particular, Sadler et al. (2002) used a combination of the optical 2dF survey and the NRAO VLA Sky Survey (NVSS) to identify the optical counterparts of radio sources. This study was not only focused on QSOs but star-forming galaxies as well and by blindly examining the optical counterparts of the radio sources they find a mixture of active galaxies (60%) and star-forming galaxies (40%). Similarly, Ivezić et al. (2002) used a combination of the newly established SDSS and the Faint Images of the Radio Sky at Twenty Centimeters (FIRST; Becker et al., 1995) survey. Here they found that the majority of the radio sources were optically resolved galaxies, whereas nearly all optically unresolved radio sources had non-stellar colors indicative of QSOs. While this technique is not affected by dust bias (seen e.g., in the UVX approach) it is highly incomplete as only around $\sim$ 10% of QSOs are very luminous in radio emission (White et al., 2000).

Probing QSOs using the X-ray and near-infrared emission has also been revised. In particular, Grazian et al. (2000) find QSOs identified on the basis of their spatially unresolved X-ray emission measured in the ROSAT All-Sky Survey. Their sample was compared to the previously most extensive color-selected Palomar-Green (PG) bright quasar survey (Schmidt & Green, 1983) and they found that their sample was three times larger. X-ray surveys of QSOs appear to be more complete than most other selection methods. The contamination from other sources than AGN in these surveys is very small as well, with most contaminants being either O to A stars and/or starburst galaxies. With the commence of the *Chandra* (Weisskopf et al., 2002) and *XMM-Newton* (Jansen et al., 2001) X-ray satellites this method has been intensively used (see e.g., Brandt & Hasinger, 2005, for a comprehensive review).

In the first couple of years following the study by Warren et al. (2000, see e.g., Fig. 1.2) using the distinct near-infrared colors of QSOs, small-area studies have been executed using this approach as well. In particular, Croom et al. (2001) followed up on the specific KX selection, using the photometric catalogue of the ESO Imaging Survey in the *Chandra* Deep Field South (EIS-CDFS) to select compact objects with $J - K$ colors redder than the stellar sequence. Similarly, Cutri et al. (2002) used the photometric data of the Two Micron All Sky Survey (2MASS; Skrutskie et al., 1997, 2006) to select objects with red $J - K$ colors. However, in their study only objects with $J - K > 2$ are targeted since the primary focus was to select the "missing" red QSOs (and 95% of the known QSOs at the time had $J - K < 2$).

In the first few years of this millennium, large-scale searches for QSOs almost exploded using the selection techniques developed in the preceeding decades. Most of these are based on optical/infrared color selection using the distinctive colors of QSOs compared to the most severe contaminants, e.g., stars and star-forming galaxies. The photometric selection of QSOs has the advantage that it allows to quickly build large samples with surveys covering wide regions of the sky. The short and long wavelength range (X-ray and radio) detections of QSOs have gained prevalence as well, with less (or at least other) biases than the existing photometric surveys. However, for all of these techniques, candidate QSOs have to be spectroscopically verified after identification to be properly classified regarding redshift, extinction etc.

1.4 Modern Selection of Quasars

Following the boom of QSO selection in the early 2000s more and more QSOs are still being detected but to surpass the previous amount of identified QSOs new and more complex selection techniques and/or larger and deeper surveys have to be utilized. In particular, with the launch of the two new mid-infrared satellites (*WISE*; Wright et al., 2010) and (*Spitzer*; Werner et al., 2004), the search for QSOs using this specific wavelength range was further developed. Several studies based on *WISE* (Stern et al., 2012; Mateos et al., 2012; Assef et al., 2013; Secrest et al., 2015) and *Spitzer* (Lacy et al., 2004, 2007; Stern et al., 2005; Donley et al., 2012) mid-infrared colors of QSOs have been executed, using either one- or two-color criteria. All of these mid-infrared color selection techniques rely on the fact that QSOs are easily distinguishable from stars and star-forming galaxies in mid-infrared color-color space (see e.g., Nikutta et al., 2014, for a comprehensive empirical study of how different types of objects differentiate in *WISE* color-color space). As discussed previously the accretion disk of the AGN heats up the surrounding torus causing the dust to obtain temperatures not seen in non-QSO SEDs. Furthermore, the advantage of the *WISE* mission is that it is an all-sky survey so selection using *WISE* colors can yield very large samples of QSOs, see e.g., Secrest et al. (2015), across the full sky.

The commence of the two X-ray telescopes *Chandra* and *XMM-Newton* have further improved the detection of QSOs as well. In particular the identification and study of the optical/near-infrared counterparts have proven to be successful. The depth of these two surveys in especially the approximately two square degree field centered at $(\alpha, \delta) \approx (10^{\rm o}, 02^{\rm o})$ known as the COSMOS field (Scoville et al., 2007) is so far unparalleled. Concurrently, deep optical/near-infrared surveys (see e.g., Capak et al., 2007; McCracken et al., 2012, and references therein) have been executed in the same region of the sky. The *Chandra*-COSMOS (C-COSMOS) (Elvis et al., 2009; Civano et al., 2012) and the XMM-COSMOS (Hasinger et al., 2007; Cappelluti et al., 2009; Brusa et al., 2010) surveys use a combination of these two samples to detect QSOs down to very faint magnitudes. This technique is very robust, with the only bias being towards heavily obscured, Compton-thick QSOs (with column density $N_H > 10^{24}$ cm^{-2}). It is worth noticing that this particular bias is not present in the mid-infrared selection technique, which thereby would allow for selection of extremely obscured QSOs. By robustly identifying the optical/near-infrared counterparts, accurate photometric redshifts can be determined for each of the X-ray detected AGN (Salvato et al., 2009, 2011).

The KX selection technique, previously only applied in a small-area study, has also been revived in the last few years, using the same basic principle of the K-band excess of QSOs compared to that of stars but with a few modifications (Maddox et al., 2008, 2012). First of all, the new KX selected samples are based on photometric data from the UKIRT Infrared Deep Sky Survey (UKIDSS; Lawrence et al., 2007), which is 12 times larger in effective volume than the 2MASS survey and has an ~ 3 fainter magnitude limit in the K-band. Secondly, in the most recent paper by Maddox et al. a custom designed photometric redshift (photo-z) algorithm is applied to determine if the objects with K-band excess have colors consistent with those expected for QSOs. This code basically contains a lot of different templates, e.g., eight QSO templates with and without reddening, seven galaxy templates and several star templates from the Bruzual-Persson-Gunn-Stryker atlas[1]. The code then determines which of the templates provides the best match (lowest χ^2) for the optical and near-infrared magnitudes and if the objects are not reliable QSO candidates they are discarded. The process of the final candidate selection is illustrated in Fig. 1.4. It is based on first rejecting objects with no K-band excess

[1] http://www.stsci.edu/hst/observatory/cdbs/bpgs.html

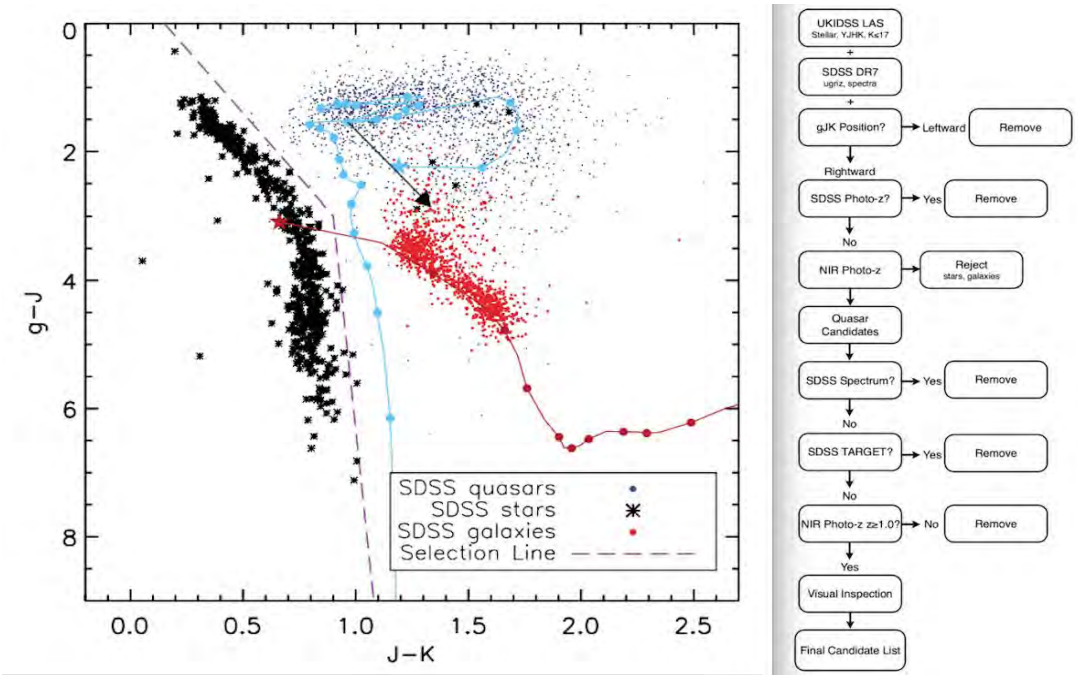

Figure 1.4: The selection criteria of the most recent KX selected QSO survey. From Maddox et al. (2012).

(leftward of the selection line), and then using their near-infrared photo-z algorithm to further eliminate galaxy or stellar contaminants (and unfortunately also some QSOs, see Heintz et al. 2016, Appendix B)

About ten years after the release of the first SDSS QSO survey, the SDSS programme modified their selection as well. The first two phases of SDSS (SDSS-I/II) targeted QSOs for spectroscopy based on the point sources which are separated from the stellar locus in optical color-color space (Richards et al., 2002), as described previously. Furthermore, extended objects with a strong UV excess as well as point sources with radio emission from the FIRST survey were included, and the final QSO sample at the end of phase two (and data release 7; SDSS-DR7) contain more than 100,000 spectroscopically confirmed QSOs (Schneider et al., 2010). The new, third phase of the SDSS (SDSS-III) relies on several other selection techniques, introducing the Baryon Acoustic Oscillations Survey (BOSS; Ross et al., 2012; Dawson et al., 2013). In this new approach of selecting QSOs the sample is divided into two sub categories: A core sample selected only from single-epoch imaging using a uniform selection algorithm similar to the previous UVX selection and a bonus sample selecting candidates using as many methods and additional data as possible. These include e.g., likelihood approaches that determines the likelihood that each object is a quasar given its photometry and models for the stellar and quasar loci, and the continuous use of X-ray and radio surveys. A recent study addresses the issue of bias against dust-rich QSOs in the SDSS selection (Ross et al., 2015) by using a combination of the SDSS and WISE surveys to detect the red QSOs missing in the SDSS-III/BOSS sample. The technique of selection based on the optical variability of QSOs have recently been revived as well (Schmidt et al., 2010; Graham et al., 2014). Both studies are extremely pure and complete, where the former compare their selection to the SDSS QSO sample, with a significant increase in the density of QSOs at redshifts, $2.5 < z < 3$.

To conclude my introduction I will briefly describe the two recent studies leading up to my

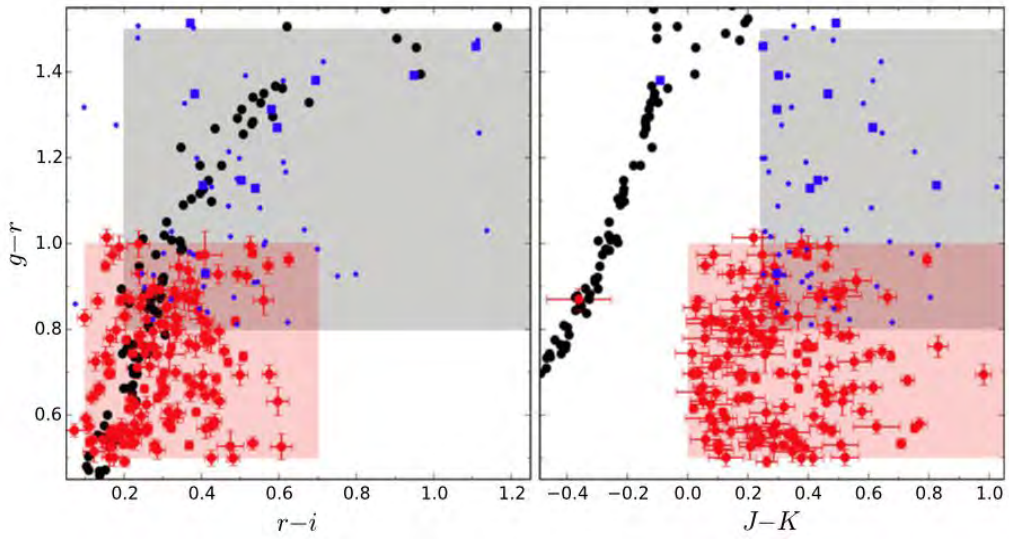

Figure 1.5: The optical and near-infrared selection criteria of Paper I and II in two color-color diagrams. Blue and red dots are confirmed QSOs whereas squares are contaminants. This figure is adapted from Krogager et al. (2015).

Masters project, described fully in Chapter 2. The two studies are by my supervisor Fynbo et al. (2013) and his former PhD student Krogager et al. (2015) (which henceforth just will be denoted as Paper I and Paper II, respectively) dubbed the High A_V Quasar (HAQ) survey. The original focus was to select QSOs reddened by foreground intervening dusty absorbers that, due to dust bias, were not included in the SDSS QSO samples. Similar to the KX method they apply a selection based on the K-band excess of QSOs but with more stringent optical criteria to tailor the search for red QSOs only. They based their selection on optical and near-infrared photometric data from the SDSS and UKIDSS surveys, respectively. The pilot study of Paper I revealed some contamination of mainly galaxies and dwarf stars, so the selection criteria were refined in Paper II and the purity of the HAQ survey was found to be high ∼97% (with the contaminants being either unclassified objects or stars selected by mistake). In Fig. 1.5 I show the gri and $grJK$ criteria utilized in Paper I (grey box and blue symbols) and Paper II (red box and symbols). The degeneracy of stars and QSOs in near-infrared color space compared to optical color space is illustrated as well.

By invoking strict optical selection criteria the HAQ sample is not in any way complete but it has been proven to select dust-reddened QSOs efficiently. This approach is also solely based on color-criteria, compared to the most recent KX selection where they run their KX candidates through a photo-z code as well. This approach is rather troublesome, especially because in the study by Maddox et al. (2012) they first argue how many of their detected QSOs are missing and/or are rare compared to the known samples and *then* they run the candidates through a somewhat standard template fitting code. In the HAQ survey candidates are only selected by their red colors and nothing else, leading to the discovery of peculiar QSO systems, see e.g., Chapter 2, which would possible be discarded by the KX photo-z algorithm (for an example of this, see Heintz et al. 2016, Appendix B).

Even though the original focus of the HAQ survey was to search for dusty DLAs in the spectra of QSOs, very few were actually discovered. The HAQ survey consists mainly of QSOs experiencing intrinsic dust reddening and/or strong broad absorption lines (BALs). This sub-

population of QSOs is interesting in its own way, however, and will be addressed separately in a future study. The fact that most of the candidate QSOs selected by the HAQ criteria have not been observed by the SDSS-III/BOSS survey are an important result as well. Numerous studies regarding the nature of QSOs and how QSOs (and in general all galaxies) evolve through cosmic time will reveal a distorted census on this subject if only a sub-population of the true underlying types of QSOs are examined. This issue has been addressed in Heintz et al. (2016, Appendix B). Here, we (the co-authors and I) found that the HAQ selected QSOs consitute $\sim 20\%$ of the total population of bright ($J < 20$ mag), spatially unresolved QSOs. Moreover, by analysing all the quasars in the parent sample, we found that $\sim 40\%$ of the QSOs are reddened (defined as having $A_V > 1$).

When building large area surveys it is crucial that the sample selected for spectroscopic follow-up consists of the optimal balance between efficiency and completeness. Some surveys, e.g., the HAQ survey does not aim at building a complete sample of reddened QSOs but only focus on objects with colors consistent with QSOs reddened by intervening dust-rich absorbers. This survey was, however, found to be highly efficient with $< 3\%$ contamination. Others, like the KX or SDSS surveys aim at identifying a complete sample of QSOs, allowing for a higher fraction of contaminating sources. The ultimate goal would be to obtain both a complete and reliable sample from which the true population of QSOs could be determined.

Instead of searching for QSOs missed by existing QSO samples, to thereby account for the missing population, an alternative technique could be to define a sample of QSOs unbiased in terms of colors. In that way both the QSOs with red optical colors can be selected, typical UVX QSOs will be selected and possible new and exotic types of QSOs could be identified. As for most other surveys this new approach would have to sufficiently remove stellar contamination. Heintz et al. (2015) (included as Appendix C) propose building such a survey using the recently launched *Gaia* satellite, which will make astrometric measurements of distances, parallaxes and proper motions for 1.1 billion stars in the Milky Way (de Bruijne, 2012). Due to the large cosmological distances to the majority of QSOs these will appear stationary where most stars will show significant proper motions on the sky. In the paper we examined the feasibility of selecting QSOs based on a non-moving criterion below the error limit of *Gaia*, i.e., determine the number of stationary stellar sources compared to the density of QSOs.

In Chapter 3 I will conclude on all the different techniques of selecting QSOs described in this thesis, with specific focus on the eHAQ selected sample and in Chapter 4 I will reveal some of the future projects I am currently involved in which has only recently been commenced.

Chapter 2

A Tailored Search for Red QSOs

Quasi-stellar objects (QSOs) are some of the most luminous, extragalactic objects observed to date, see e.g., Chapter 1. As a consequence, these can be detected out to large cosmological distances thereby making them viable tools in probing the formation and evolution of galaxies and super-massive black holes (SMBHs) through cosmic time. Although QSOs are physically interesting on their own, the cosmological applications of these have shown to be of similar (if not even greater) importance. In particular, the use of these as bright background sources shining through metal-rich and dusty foreground galaxies is of crucial importance to the star formation inventory in the Universe. Such galaxies are expected to be numerous but too faint to be detected in emission. Absorption studies in the spectra of QSOs allow us to illuminate the content of elements and dust in these otherwise concealed young galaxy systems.

If the intervening absorption systems contain large amounts of dust they will redden the background QSO to the point where optical UVX selection will fail to identify this particular system as a QSO. Following, it was recently discovered that intervening absorbers would redden the QSOs to such a degree that the color criteria utilized in the Sloan Digital Sky Survey (SDSS; York et al., 2000) first and second phases (SDSS-I/II), which is the survey where most of the DLAs systems known to date have been found, were on the verge of missing this type of system (Noterdaeme et al., 2009, 2010, 2012; Kaplan et al., 2010; Fynbo et al., 2011; Wang et al., 2012; Krogager et al., 2016). A bias will then emerge toward even more dust-rich and hence metal-rich intervening absorption systems reddening the background QSOs and thereby effectively excluding them from similar large area optical QSO surveys. Selecting QSOs based on their near-infrared colors, as demonstrated in Paper I and II, found that several reddened QSOs were indeed missing in the SDSS DR7 and DR10 QSO samples (Schneider et al., 2010; Pâris et al., 2014, respectively).

Any bias in large area QSO samples will affect the study of these where in particular the samples of QSOs with intrinsic absorption features (e.g., broad absorption line (BAL) QSOs) and QSOs with intervening absorption systems are vulnerable. Studies of reddened QSOs and the selection of these have been extensively executed during the last two decades (see e.g., Webster et al., 1995; Warren et al., 2000; Gregg et al., 2002; Richards et al., 2003; Hopkins et al., 2004; Glikman et al., 2007, 2012, 2013; Maddox et al., 2008, 2012; Urrutia et al., 2009; Banerji et al., 2012, and the introduction in Chapter 1). Most of these, however, relied on detection in either X-ray or radio. As discussed, only about $\sim 10\%$ of QSOs are radio-loud, and thus would be possible to detect in radio, where X-ray selection, although generally very robust (see e.g., Brandt & Hasinger, 2005, for a detailed review), are biased against the most obscured QSOs. Selection of QSOs using their distinct infrared colors is therefore one of the most powerful tools to successfully probe the most reddened and obscured sources.

This initiated the tailored search for reddened QSOs as described in Paper I and II, where

in this chapter I present the third phase, the *extended* High A_V Quasar (eHAQ) survey of which I was part of. In this work they (as in Fynbo, Krogager and collaborators) refined the selection criteria of Paper I and II to allow for selection of even redder QSOs at higher redshifts. Compared to the previous two samples they utilized color selection based on mid-infrared photometry from the *Wide-field Infrared Survey Explorer* (*WISE*) all-sky sample in addition to the optical/near-infrared colors from SDSS/UKIDSS photometry. To describe the recently completed eHAQ survey (see the last co-author statement in the Appendix for my contribution) I have structured this chapter as follows. In Sec. 2.1 I present the new and refined selection criteria. In Sec. 2.2 I summarize the observations and argue for an additional color cut, subsequently invoked after the first night of observing. Then, in Sec. 2.3 I show the results of the eHAQ survey and describe the analysis. Finally, I will compare the sample to other mid-infrared selection criteria of QSOs and in general other large area QSO samples in Sec. 2.4.

2.1 Photometric Data and Selection Criteria

2.1.1 Photometric Data

The targets selected for observation were selected from optical, near-infrared (NIR) and mid-infrared (MIR) photometry and point-like morphology in the SDSS (York et al., 2000) and the UKIDSS (Lawrence et al., 2007) imaging. The candidate red QSOs were first selected from the overlap of the SDSS DR8 (Aihara et al., 2011) and UKIDSS DR10 Large Area Survey (LAS) footprints and then matched with the latest all-sky *WISE* (AllWISE; Cutri et al., 2013) data release and the Faint Images of the Radio Sky at Twenty Centimeters (FIRST; Becker et al., 1995) data. The SDSS photometric data consists of magnitudes in the u, g, r, i, z optical bands at the effective wavelengths 3543Å, 4770Å, 6231Å, 7625Å and 9134Å, respectively. The UKIDSS photometric data at NIR wavelengths are given in the four Y, J, H, K bands with effective wavelengths of 10,305Å, 12,483Å, 16,313Å and 22,010Å. The AllWISE survey provides photometric data in the MIR in four bands with effective wavelengths 3.4, 4.6, 12 and 22 μm, which later will simply be refered to as W1, W2, W3 and W4, respectively.

2.1.2 Selection Criteria

Based on the pilot study in Paper I and the HAQ survey described in Paper II they (as in Fynbo, Krogager and collaborators) refined the selection criteria to target the population of extremely reddened QSOs at higher redshifts and with more extinction, A_V, due to dust than previous. From Paper I to Paper II the aim was to primarly reduce the population of contaminating stars and galaxies, whereas from Paper II to this study they primarly wanted to remove the low redshift ($z < 1.5$) population of intrinsically reddened QSOs. By examining the distribution of the HAQs from Paper II in MIR color-color space, see Fig. 2.1, they defined the eHAQ selection criteria to discard the low-z population illustrated by the shaded region in the figure.

Moreover, by applying these MIR color criteria (compared to only the optical and NIR color criteria of Paper I and II), the population of contaminating stars and galaxies can be further reduced. This is due to the fact that QSOs occupy a distinct region in MIR color-color space, see e.g., Nikutta et al. (2014) for a recent empirical study and the physical interpretation of this in the introductory Chapter 1 of this thesis. The set of optical to MIR color criteria of the eHAQ survey are as follows:

$$J < 20.0, \quad g - r > 0.5, \quad r - i > 0.4, \quad W1 - W2 > 0.6, \quad 2.0 < W2 - W3 < 4.0$$

$$(W2 - W3 < 2.85 \,\&\, W1 - W2 < 1.0) \text{ or } (W2 - W3 > 2.85 \,\&\, W1 - W2 < 1.2 \times (W2 - W3) - 2.42),$$

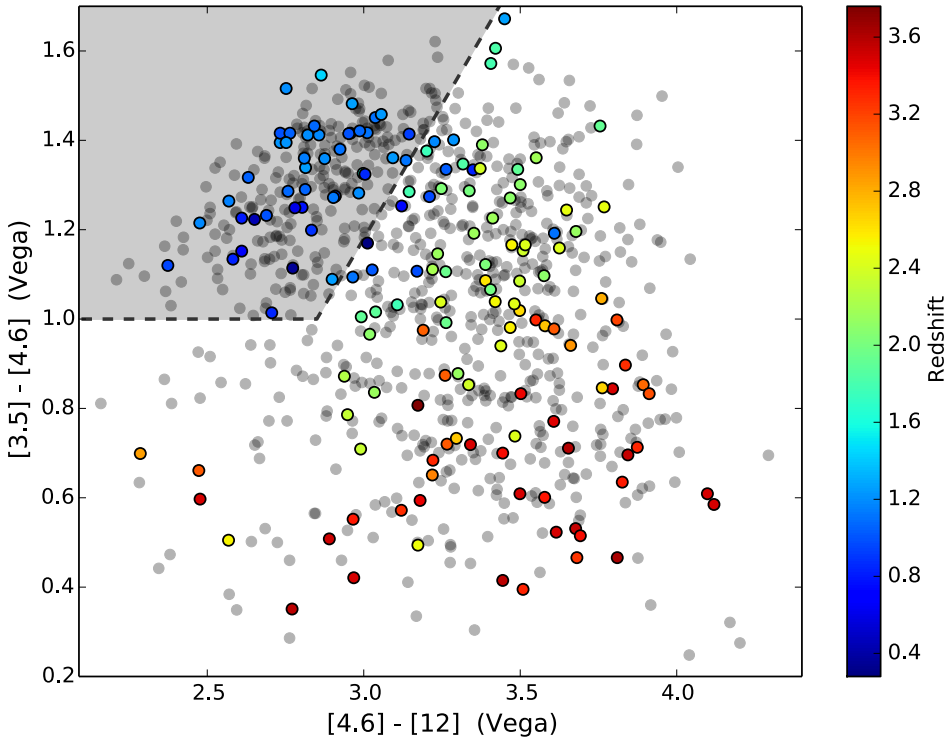

Figure 2.1: A $W2-W3$ vs $W1-W2$ color-color diagram of the HAQ sample from Paper II. The grey dots show the full HAQ sample whereas the colored dots represent the confirmed QSOs color coded as a function of redshift. The grey shaded area show the location of the low-z population of QSOs which was removed in the refined eHAQ criteria. Originally shown in figure 8.1 of the PhD thesis by Krogager (2016).

where the SDSS and UKIDSS optical to NIR colors are on the AB (Oke, 1974) magnitude system and the *WISE* colors are on the Vega magnitude system. Following the same procedure as in Paper I and II they required that the candidates are point sources in both the SDSS and UKIDSS imaging and that the targets have not already been observed spectroscopically by the SDSS/BOSS DR12Q or have been observed before as part of Paper I or II. This set of refined optical to MIR selection criteria were found to improve the selection of high-z QSOs ($z > 1.5$) and do not discard the reddest candidate QSOs with very red optical colors in $g-r$ as was the case for the HAQ survey. In Paper II the limits of $0.5 < g-r < 1.0$ and $0.1 < r-i < 0.7$ were primarily introduced to reduce the galaxy and stellar contamination. However, these will be effectively removed by invoking the strict MIR color criteria and thereby allow for selection of the optically reddest objects with the refined optical color criteria.

In Fig. 2.2 the selection criteria of the eHAQ survey is illustrated and compared with those of Paper I and II. In the right panel I show an additional criterion of $J-K > -0.1$ applied after the first night of observation due to severe stellar contamination. I will address this issue further in Sec. 2.3 and 2.4. It is clear from Fig. 2.2 that part of the eHAQ candidates overlap with the objects from Paper I and II in optical and NIR color-color space and that some eHAQ candidates might already be part of the previous two samples, but these were removed prior to the spectroscopic follow-up campaign. I compare the observed eHAQs with the stellar track of standard stars and M-dwarfs, respectively, from Hewett et al. (2006). The K-band excess of most QSOs compared to that of stars is clearly shown in Fig. 2.2 as well, whereas the optical

colors of reddened QSOs coincides heavily with the stellar locus.

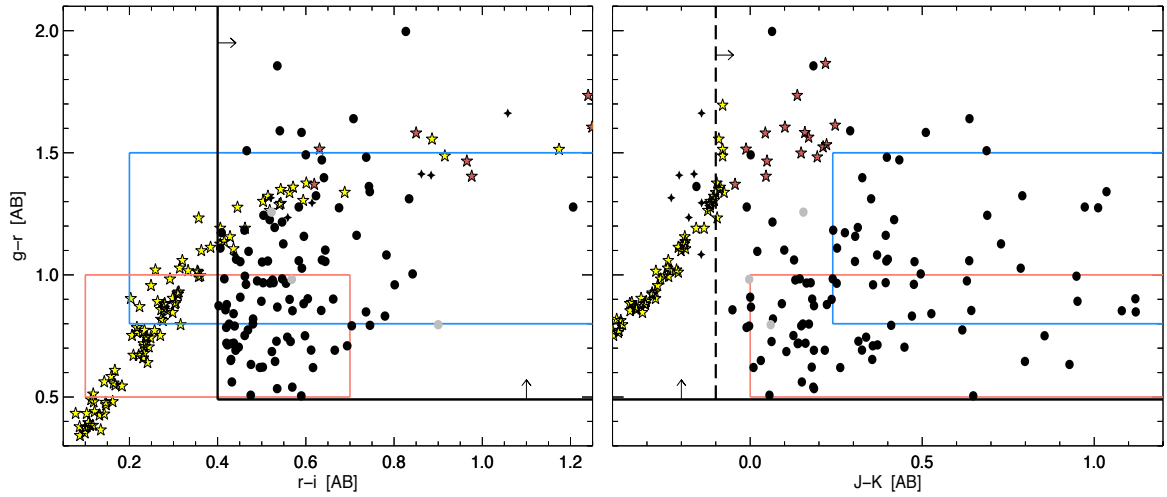

Figure 2.2: Optical/NIR color-color diagrams of the observed eHAQs (black symbols). The black dots show the confirmed QSOs, the grey dots show the unidentified objects and the black star symbols show the contaminating stellar sources. The stellar track from Hewett et al. (2006) is shown by the yellow and indigo star symbols, representing photometry of standard stars and M dwarfs, respectively. The selection criteria of Paper I and II are represented by the blue and red boxes (same as in Fig. 1.5), respectively, and the lower limits in $g-r$ and $r-i$ from the eHAQ criteria is shown by the black solid lines and arrows. The black dotted line in the $grJK$ color-color diagram show the $J-K > -0.1$ cut added subsequently to remove the observed stellar contamination. The MIR criteria of the eHAQ survey effectively removed the galaxy contamination found in Paper I in the reddest part of the optical/NIR color-color diagrams.

2.2 Spectroscopic Observations and Data Reduction

2.2.1 Observational procedure

The observations of the candidate red QSOs were executed during a range of observing runs with the Nordic Optical Telescope (NOT) on La Palma in March 2015 (the observing run I did), August 2015, September 2015 and February 2016 (a run of which I was the principal investigator, P.I.). The NOT is a 2.5 m telescope made for observations at optical and NIR wavelengths. In total we retrieved a secure spectral identification of 111 (of which I observed 34) of the eHAQ candidates, all listed in Table 2.1. The spectra were obtained using the Andalucia Faint Object Spectrograph and Camera (ALFOSC) mounted at the NOT. This instrument has a field of view of 6.4×6.4 arcmin in imaging mode and can be used for low/medium resolution spectroscopy. Following the same setup as in Paper I and II we used grism #4 covering the wavelengths 3200-9100Å with a spectral resolution of $R \sim 300$ and a slit width of 1.3 arcsec for most of the targets. In our observational setup we also applied for the three new grisms, #18, #19 and #20, covering the wavelength ranges of 3530-5200Å, 4510-6670Å and 5850-9840Å, respectively. If some of the QSOs showed interesting or uncertain spectral features, these grisms were used to obtain better resolution in the given wavelength ranges. Blocking filter #94 was used in the grism #4 observations in order to eliminate second-order contamination from wavelengths shorter than 3560 Å. All the spectra were taken aligning the slit at parallactic angle where the

width of the slit used for each specific target were determined based on the seeing at that time. We preselected slits with 0.75, 1.0, 1.3, 1.8 and 2.5 arcsec widths for each of the observing runs. All information regarding the slits and grisms for the ALFOSC instrument can be found at the NOT web page[1].

2.2.2 Data reduction

All the obtained spectra were processed using a combination of IRAF[2] and MIDAS[3] tasks for low resolution spectroscopy using provided `IDL` scripts (from J. Fynbo). First, cosmic rays were removed from the spectra using the software[4] developed by van Dokkum (2001). Simply, this software rejects light with extreme flux compared to the mean spectrum. The wavelength calibration was done using a script, which takes as input the extracted data along with one of the Helium-Neon (HeNe) lamp exposures taken just before and after each science exposure. The flux calibration for each of the spectra was done using a spectrophotometric standard star observed on the same night as the science spectra. We corrected the spectra for Galactic extinction using the extinction maps of Schlegel et al. (1998). To improve the absolute flux calibration we scaled the spectra to be consistent with the r-band photometry from SDSS.

2.3 Results

In Table 2.2 the classifications for the full sample of eHAQs, the determined redshifts and the estimates on the amount of extinction, A_V, due to dust is presented. Following the same procedure as in Paper I (in Paper II they used a fitting code), the redshifts for each of the eHAQs were visually determined from the apparent emission lines in the spectra. In Fig. 2.3 this technique is illustrated on one of the objects, eHAQ1244+0841. Basically, I overplotted a composite QSO template by Selsing et al. (2016) matching the emission lines in the spectra, with and without reddening (solid red and dashed blue line, respectively). This template is constructed by combining spectra of luminous "blue" QSOs at $1 < z < 2.1$ selected from the SDSS. The spectra for the composite were observed with the X-Shooter instrument at the Very Large Telescope (VLT), which simultaneously extract the UV to NIR light. Hence, the observed effect of variability in QSOs is not an issue in this composite. For most QSOs this procedure is very reliable except for the most obscured population with little to no apparent emission line features. The most prominent emission lines observed in QSO spectra are Ly$\alpha\lambda$1216, C IVλ1549, C III]λ1909 and Mg IIλ2800 dependent on the redshift. When these are securely identified in the spectra, the composite template can be overplotted and the exact redshift can (in most cases) easily be determined by eye.

In Fig. 2.4 some more examples of the one-dimensional spectra are shown together with the photometric data points of SDSS and UKIDSS. From the total of 111 eHAQ targets we (Johan and I) were able to securely classify 101 as QSOs. The purity of this sample, i.e., the efficiency of the selection criteria, is then $\sim 91\%$ defined from the ratio of QSOs to the total number of objects in the sample. The two objects, eHAQ1030+1040 and eHAQ1132+1243, are so far unidentified. The spectrum of eHAQ1030+1040 (see e.g., Fig. 2.4) show extreme absorption features and we were thus not able to identify any emission lines and thereby determine a redshift for this

[1] http://www.not.iac.es/instruments/alfosc/

[2] IRAF is the Image Reduction and Analysis Facility, a general purpose software system for the reduction and analysis of astronomical data. IRAF is written and supported by the National Optical Astronomy Observatories (NOAO) in Tucson, Arizona. NOAO is operated by the Association of Universities for Research in Astronomy (AURA), Inc. under cooperative agreement with the National Science Foundation

[3] ESO-MIDAS is a copyright protected software product of the European Southern Observatory. The software is available under the GNU General Public License.

[4] Cosmic-Ray Rejection by Laplacian Edge Detection

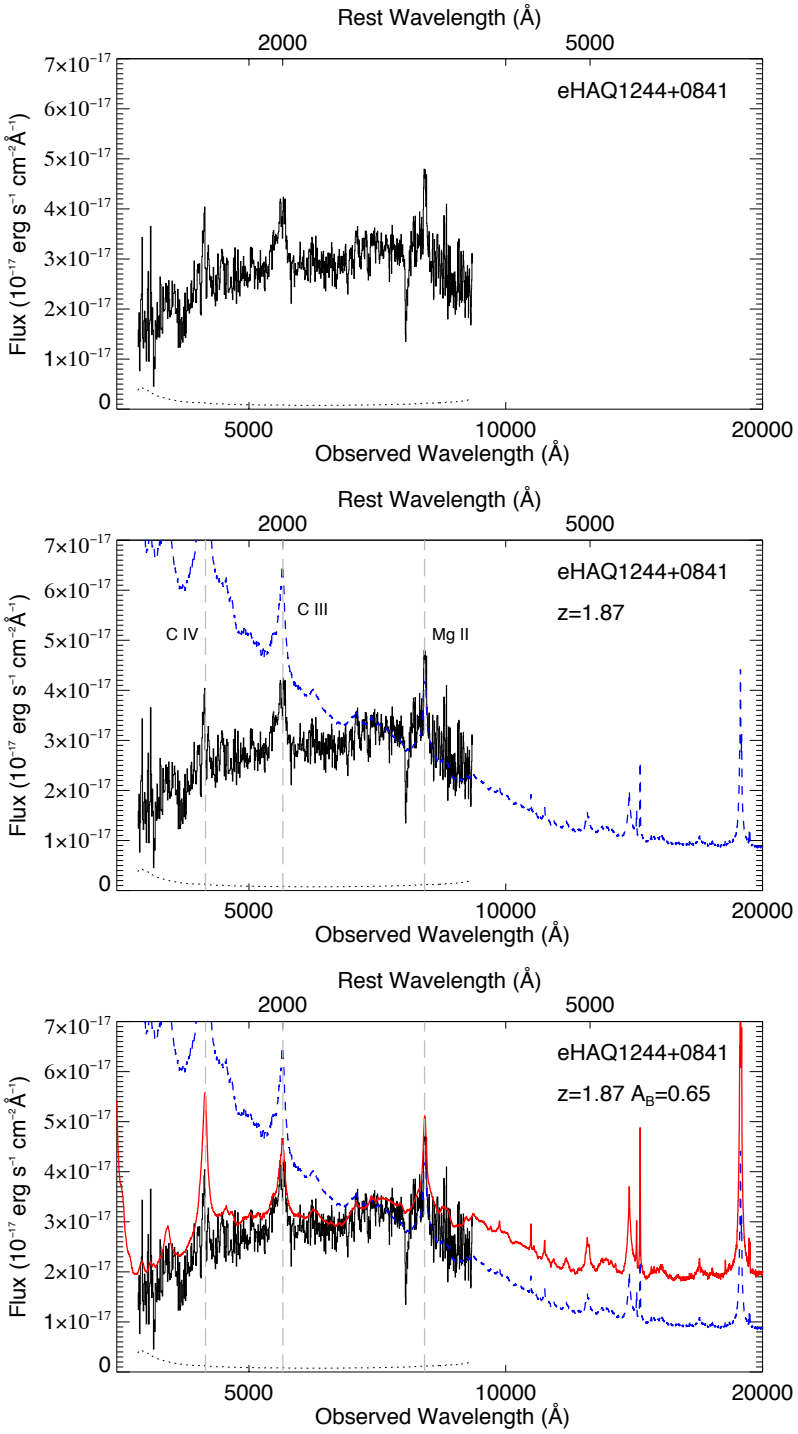

Figure 2.3: The illustrated technique of which the redshift and the amount of reddening, A_B, were determined for each of the observed eHAQs in our sample. In the upper panel is the observed wavelength and flux calibrated spectrum (black solid line). In the middle panel the unreddened composite QSO template is shown (blue dashed line), matched to the emission lines marked in the spectrum. In the lower panel the reddened composite QSO template is shown (red solid line), matched to the slope of the spectrum.

object. My best guess is that this object belongs to the type of extreme broad absorption line (BAL) QSOs. On the contrary, the spectrum of eHAQ1132+1243 shows no signs of emission and absorption features at all. The remaining eight contaminating sources were found to good matches with either G or M type dwarf stars, based on the shape of the SEDs. These entered the selection before the application of the $J-K$ color cut, indicating that the MIR color criteria only do not robustly separate QSOs from this class of stellar contamination. Other hypotherized MIR color selections of QSOs using *WISE*, (see e.g., Stern et al., 2012; Mateos et al., 2012; Assef et al., 2013; Secrest et al., 2015), will be strongly affected by this as well. In Sec. 2.4 I will discuss these different MIR selection criteria in the context of the MIR colors of the HAQ and the eHAQ surveys and explore the completeness of and the contamination observed in each of these.

The amount of reddening for each of the objects is calculated using the Small Magellanic Cloud (SMC) extinction curve as formulated by Gordon et al. (2003), following the same procedure as in Paper I and II. The extinction is determined by again visually fitting the composite QSO template to the photometric data points and the observed spectra, see Fig. 2.3. I disregard photometric data bluewards of the Lyα emission line and in case of strong absorption at individual data points these were excluded as well. In Fig. 2.4 the photometric data points are shown as the red dots at the u, g, r, i, z, Y, J, H and K effective wavelengths. The amount of dust is computed by increasing the dust parameter, A_B, of the composite template until the slope matches that of the observed spectra. The amount of dust is first computed in the B-band (first suggested by Pei, 1992) and then converted to the extinction in the V-band following the reddening law for SMC-like extinction (Gordon et al., 2003):

$$A_V = \frac{A_B}{1 + 1/R_V}, \quad R_V \sim 2.74, \tag{2.1}$$

to match the generally accepted notation. Here R_V is simply the slope of the reddening curve, where smaller values of R_V corresponds to steeper extinction curves. Some authors also use the $E(B-V)$ parameter as an indication of the amount of dust, see e.g., Maddox et al. (2008, 2012). To compare our findings to their studies (and in general other studies using the same notation) the relation for conversion is given by:

$$R_V \equiv A_V / E(B-V) \implies E(B-V) = \frac{A_V}{R_V}, \tag{2.2}$$

following the parametrization of Gordon et al. (2003).

In Fig. 2.5 the distribution of redshifts (left panel) and A_V (right panel) of all the spectroscopically verified eHAQs is shown compared to the samples presented in Paper I and II. First, I wish to highlight the success of applying the MIR color-color cuts which effectively removes the low-z population ($z \lesssim 1.5$) of QSOs. This population of intrinsically reddened QSOs contributed to a substantial part of the samples presented in Paper I and II. Although interesting on their own, the main goal was to search for QSOs with intervening DLA systems which only can be recovered from the spectra of QSOs at $z \gtrsim 2$. At redshifts below, the Lyα emission and absorption features will be at too short wavelengths to enter the observable optical wavelengths around $\sim$3500Å. This limit arises from the atmospheric cut-off which can not be bypassed with ground-based telescopes.

I found a similar peak in the redshift distribution at $z \sim 2.5$ in all three samples. It is worth noting that this was the exact wavelength range of which the SDSS were biased against, revealing a large population of QSOs in this specific range than what has previously been reported in optically selected QSO samples. Compared to the samples of Paper I and II the eHAQ sample do not effectively target the population of QSOs at $z \gtrsim 3$, although the two QSOs at the highest redshifts (at $z = 4.25$) of the three surveys were recovered in this sample. This could indicate

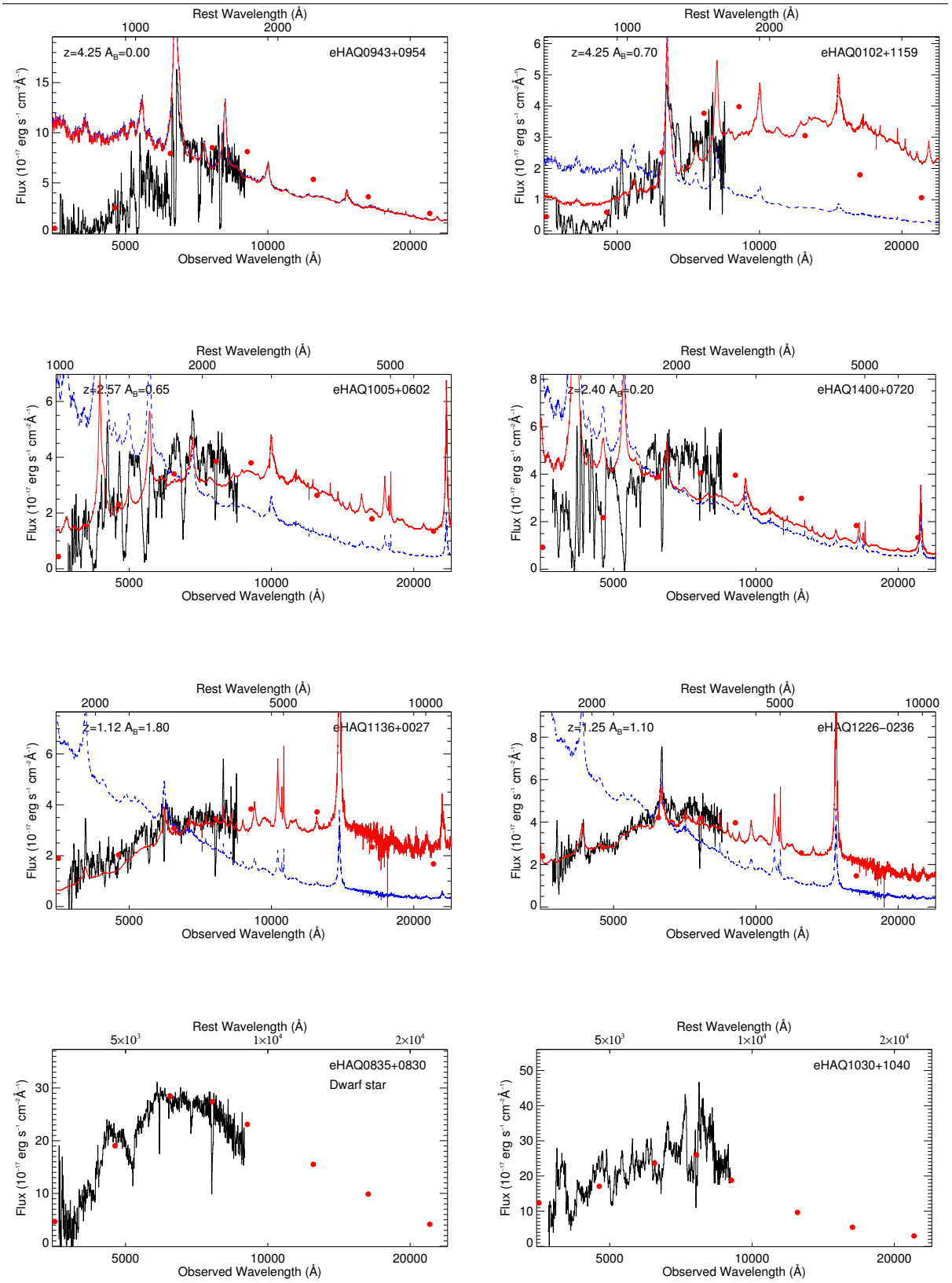

Figure 2.4: Examples of some of the most distant and dust-reddened eHAQs observed, one contaminating dwarf star and one unidentified object. The solid black line in each of the panels is the observed spectrum. The red dots represents the photometric data in the optical/NIR u, g, r, i, z, Y, J, H and K bands and the solid red and the dashed blue lines show the composite QSO template with and without reddening, respectively.

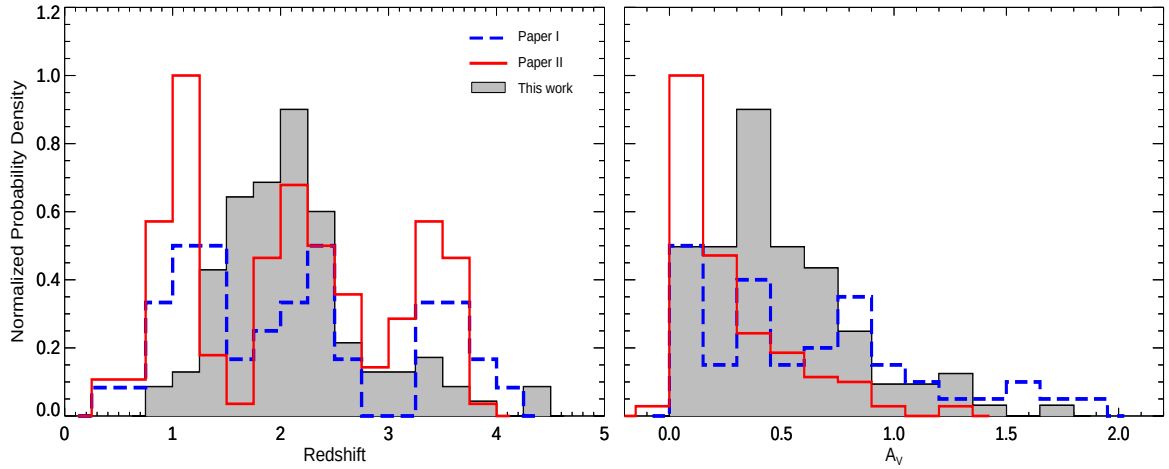

Figure 2.5: Probability density distribution of redshift (left panel) and reddening, A_V (right panel), for the red QSOs in the eHAQ sample (grey filled histogram) compared to the distributions of the red QSOs from Paper I (blue dashed histogram) and II (red solid histogram). The revised eHAQ selection criteria was successful in removing the population of intrisically reddened $z < 1.5$ QSOs. The amount of reddening was found to be higher on average in the eHAQ sample compared to the previous.

the limits induced by the conservatively defined MIR color criteria. From Fig. 2.1 it can be realized that the $W1 - W2 > 0.6$ color cut will effectively remove most of the QSOs at the highest redshifts. I will adress this issue further in Sec. 2.4. The conservative cut in $W1 - W2$ was originally invoked to remove any possible stellar and/or galaxy contamination.

The distribution of the reddening, A_V, of the eHAQ sample in the right panel of Fig. 2.5 shows that the sample in general targets more reddened QSOs than the previous two samples. Unfortunately, I found that this was primarly due to the large fraction of BAL QSOs contained in the eHAQ sample, where the aim was to search for QSOs heavily reddened by dust-rich intervening absorbers. The larger fraction of BALs and the higher mean value of A_V arises from less conservative cut in $g - r$ compared to the HAQ survey in Paper II. By only applying a lower limit in $g - r$ the selection allow for observations of objects with extreme red optical colors. This introduces a lot BALs in this sample but also allow for observations of the two QSOs at the highest redshifts ($z = 4.25$) from all three of the surveys, also having very red colors in $g - r$.

In Fig. 2.6 the full eHAQ sample is shown in four optical/infrared color-color diagrams color coded as a function of redshift and A_V, respectively. There is a clear tendency of high redshift and A_V toward red optical and NIR colors. In the two MIR color-color diagrams the high redshift tendency is towards blue $W1 - W2$ and red $W2 - W3$ colors, whereas the tendency in reddening is towards the red regions in both the $W1 - W2$ and $W2 - W3$ colors instead. This degeneracy was expected since Fynbo et al. (2013) and Krogager et al. (2015) also found an anti-correlation between redshift and reddening of the QSOs selected with their color criteria.

By briefly examing the one-dimensional spectra only, a possible case of a QSO reddened by a foreground galaxy is observed in eHAQ0835+0127, see Fig. 2.7. It certainly has a $z = 2.84$ DLA feature, and there is indications of many strong metal lines. This system, together with any other possible absorbers from this sample, will be discussed in more detail in a future work.

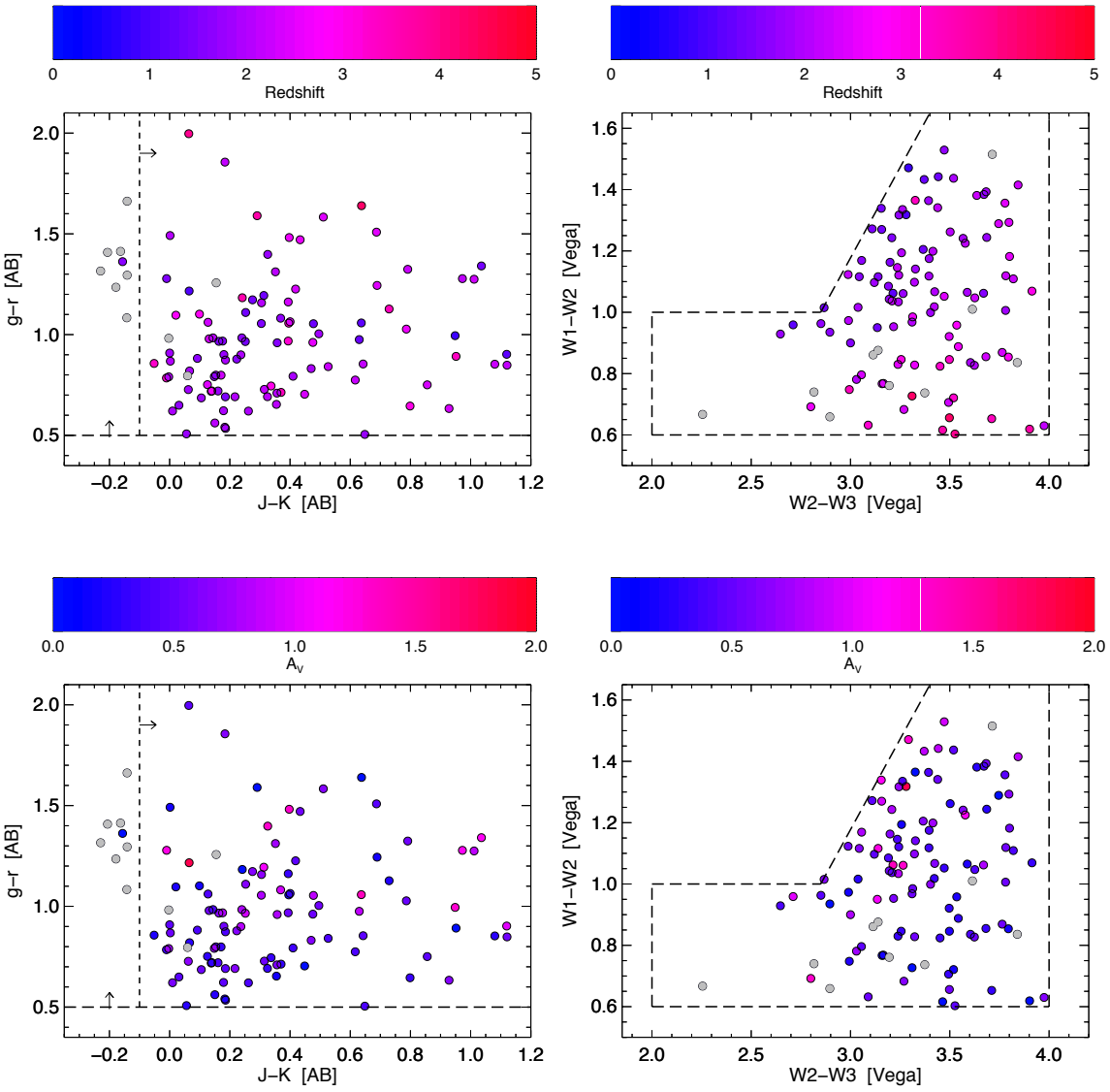

Figure 2.6: The full sample of eHAQs color coded as a function of redshift and A_V shown in four optical/infrared color-color diagrams. The grey dots represent the contaminating sources and the unclassified objects. The black dashed lines mark our selection criteria. The redshift and A_V tendencies toward red optical/infrared colors are clearly illustrated. In the region of blue $W1-W2$ and red $W2-W3$ colors, the objects appear to have a degeneracy between high redshifts and low amounts of reddening.

2.4 Discussion

After completion of the first observing run dedicated to obtain spectroscopic verification of the eHAQ candidates, severe stellar contamination in the original eHAQ optical and MIR color criteria described in Sec. 2.1.2 was observed. To effectively remove this type of contamination before the following observing runs we (as in Fynbo, Krogager and I) redefined the selection criteria by applying a $J-K > -0.1$ color cut, which was found to be successful. The original eHAQ color criteria was defined by assuming effective rejection of stellar and galaxy contamination using the *WISE* MIR color criteria, in addition to requiring red optical colors. Recent studies have examined the QSO population in MIR color-color space compared to that of stars

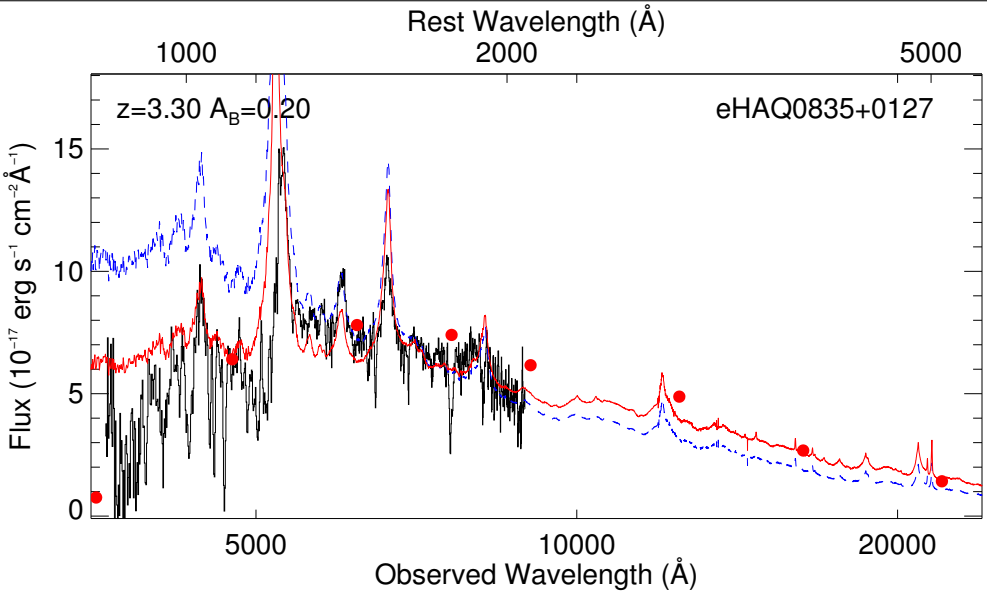

Figure 2.7: Spectrum (solid black line) and photometric data (red dots) for one of the eHAQs possibly reddened by an intervening absorption system. The background QSO is located at $z_{\rm QSO} = 3.30$ determined from the visible emission lines. The one-dimensional spectrum have a DLA feature around 4670Å revealing a foreground galaxy at $z_{\rm abs} = 2.84$ reddening the background QSO.

and galaxies and found that these should harbor a specific region in $W2 - W3$ vs. $W1 - W2$ color-color diagrams. For a comprehensive empirical study of this, see e.g., Nikutta et al. (2014), where I have adopted the left panel of Figure 2 and shown it in Fig. 2.8 (originally shown in Wright et al. (2010)). However, based on this study it appear that the region assumed to only being occupied by QSOs in the figure contain a lot of dwarf stars as well. In particular, in the original list of eHAQ candidates I found that $\sim 33\%$ of the objects had $J - K < -0.1$, clearly demonstrating how insufficient the use of MIR colors are to distinguish QSOs from stellar objects. This could indicate that other searches for QSOs using MIR color criteria might be highly contaminated as well and need to be revised. By investigating the MIR colors of the eHAQs from this study and the confirmed HAQs from Paper II, selected from optical and NIR photometry only, I will in this section discuss the contamination in and the completeness of MIR color selection of QSOs.

2.4.1 Contamination in mid-infrared color-selected QSO samples

To probe the extend of which MIR color selection of QSOs are contaminated by Galactic stellar sources I show the location of the full sample of eHAQs in $W2-W3$ vs $W1-W2$ color-color space in the left panel of Fig. 2.9. Overplotted is the eHAQ selection criteria along with two other *WISE* color selection criteria from Stern et al. (2012) and Mateos et al. (2012), respectively. The selection of QSOs (and in general AGN candidates) of Stern et al. (2012) are based on a simple $W1 - W2 > 0.8$ (Vega) color criterion. This was developed based on model colors of AGNs using the templates of Assef et al. (2010). By analyzing two cases, one with a pure AGN template with increasing amounts of dust extinction (between $0.0 < E(B - V) < 1.0$) and one with an unextincted AGN diluted by increasing amounts of host galaxy light (contributing to 0, 10, 25 and 50 per cent of the total light, respectively) they find that they are able to identify

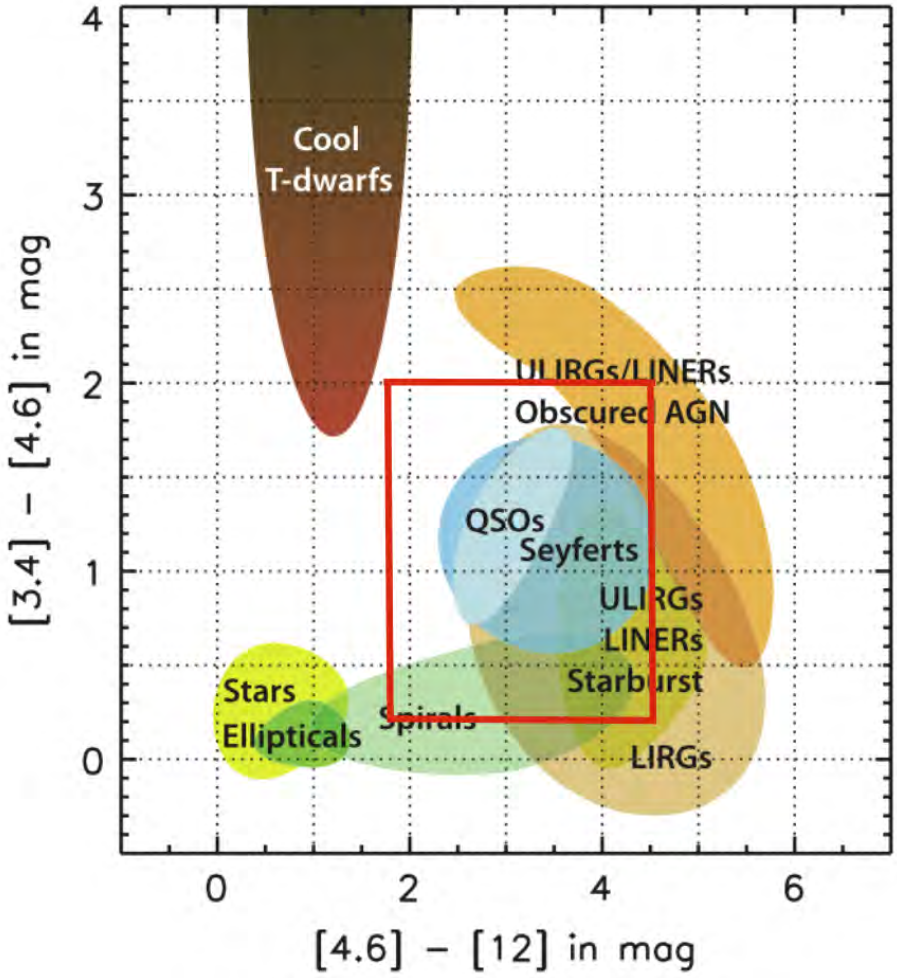

Figure 2.8: MIR color-color diagram showing the locations of various types of astronomical objects. QSOs and AGNs are easily separated from stars and galaxies since they tend to be red in both colors. The red box show the approximate region we focused on in the following two plots showing the eHAQ sample, see Fig. 2.9. Adapted from Wright et al. (2010).

pure AGNs out to $z \sim 3$ whereas for the increasingly reddened template this limit extends out to higher redshifts. The one-color criterion fails at identifying AGNs where the light from the host galaxy contributes significantly. By targeting objects in the COSMOS field (**?**) they find that the $W1 - W2 > 0.8$ selection criteria have high completeness (78%) of identifying AGNs and even higher reliability (95%) at selecting AGNs only. We observed about half of the contaminating sources above the $W1 - W2$ color cut indicating that the reliability of this specific selection technique could be overestimated.

Compared to Stern et al. (2012), the MIR color criteria of Mateos et al. (2012) are more complex. They define their selection criteria using the 3.4, 4.6 and 12 μm bands of *WISE* where they developed a MIR color wedge (black solid line in Fig. 2.9) based on the luminous AGNs from the wide-angle Bright Ultrahard XMM-Newton survey (BUXS). They argue that their selection suffer less contamination from star-forming galaxies than the simple $W1 - W2 > 0.8$ cut, but at the cost of reducing the completeness of the sample. Indeed, we can see from the left panel of Fig. 2.9 that some eHAQs would have entered the sample of Stern et al. (2012) but would not be present in the sample of Mateos et al. (2012). They argue, however, that theirs

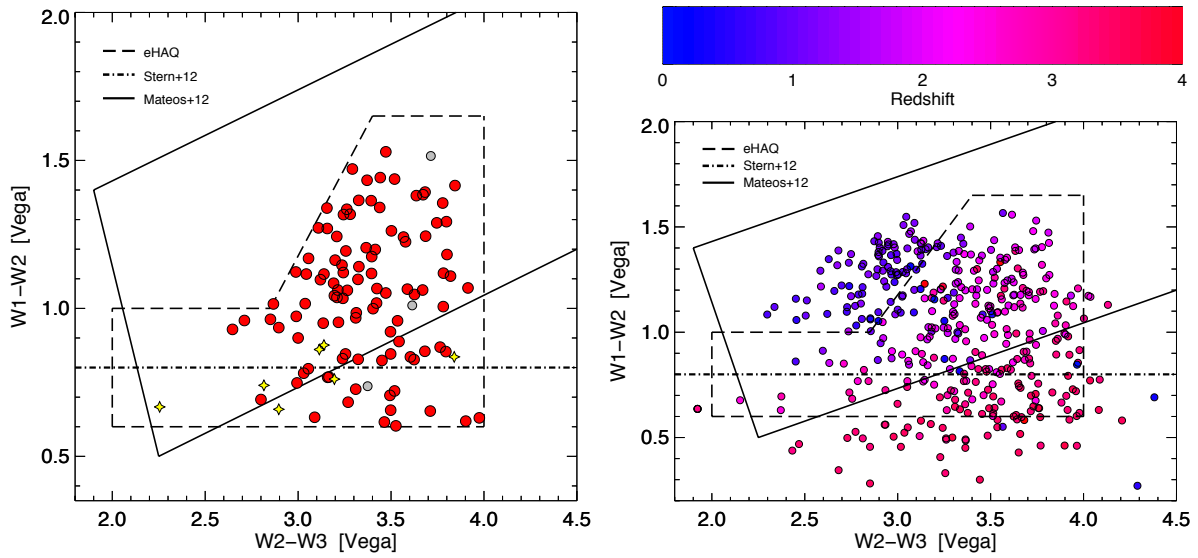

Figure 2.9: *Left panel:* The full eHAQ sample in $W2-W3$ vs. $W1-W2$ MIR color-color space. The confirmed QSOs are shown as red dots, the unclassified objects as grey dots and the observed stellar contamination as yellow star symbols. Overplotted is three different MIR selection criteria as defined by the legend. All approaches reveal stellar contamination and the exclusion of QSOs for each of the criteria is clearly demonstrated.
Right panel: The 408 already verified QSOs from the SDSS database having the same optical/NIR colors as the HAQ criteria shown in $W2-W3$ vs. $W1-W2$ MIR color-color space (similar to Fig. 2.1). The objects are color coded as a function of redshift as defined by the upper panel. There is a clear tendency in redshift, where the high-z QSOs move toward red $W2-W3$ and blue $W1-W2$ colors. All of the three MIR selection criteria reduces the completeness of their respective samples to obtain the highest possible reliability.

is the best compromise between completeness and reliability of selecting AGNs. About half of the observed contaminating stellar sources in the eHAQ sample would still be present using this MIR two-color selection so the reliability could also be overestimated in this case as well.

2.4.2 Completeness of mid-infrared color-selected QSO samples

It is now clear that all of three MIR selection criteria are incomplete in comparison to the full underlying population of QSOs. To understand the incompleteness of the eHAQ sample and the two other MIR color selections I examined the objects from the optical/NIR selected HAQ sample. The original HAQ criteria of Paper II was shown to robustly select reddened QSOs based on optical/NIR photometry only, so by analysing these in MIR color-color space it is possible to probe how many of the HAQs get rejected using the MIR selection criteria only. In the right panel of Fig. 2.9 I show the 408 objects with existing spectra from the SDSS database having the same optical/NIR colors as the objects selected for observations as part of the HAQ survey. This is similar to Fig. 2.1 but here I chose to examine the objects already observed by SDSS-III/BOSS DR12Q (Pâris et al., in prep.) due to larger sampling (408 objects) where the first figure only show the ~ 150 HAQs described in Paper II.

From the right panel of Fig. 2.9 it is clear that all three of the MIR color selection approaches are biased toward the high-z population of reddened QSOs. This bias is introduced when trying to remove the contamination of star-forming galaxies and local stellar sources, see e.g., Fig. 2.8.

Since the HAQ selection is independent of the MIR colors it is possible to probe the population of QSOs at red $W2 - W3$ and blue $W1 - W2$ colors.

Previously, when examining the completeness of various MIR selected sample, these gets compared to the optically selected QSOs from SDSS (see e.g., Secrest et al., 2015). However, the UVX selection of SDSS is found to be very insensitive to the reddened population of QSOs at $z \gtrsim 2.5$. These are located exactly in the region not selected by the MIR color criteria, i.e., both approaches of identifying QSOs are insensitive to the same types of objects. So, when comparing the completeness of one of these to the other, the true completeness will be highly overestimated. Specifically, the criterion of $W1 - W2 > 0.8$ from Stern et al. (2012) discard $\sim 25\%$ of the verified optically red, HAQ selected QSOs from SDSS, where the selection criteria of Mateos et al. (2012) discard closer to $\sim 30\%$ of the objects. The MIR color criteria of the eHAQ survey are less biased toward the $z > 2.5$ population of reddened QSOs but are by design less complete toward the population at lower redshifts. I suggest that a combination of near/mid-infrared selection criteria is required to more robustly reject contaminating stellar sources (see Chapter 4).

Table 2.1: The full sample of eHAQs observed with the NOT.

Target	**R.A. (J 2000)**	**Decl. (J 2000)**	$\mathbf{r_{SDSS}}$ **(mag)**	**Telescope**	**Exp. time (sec)**
eHAQ 0001+0233	00 01 21.70	+02 33 05.00	17.86	NOT	2×300
eHAQ 0001+0431	00 01 42.90	+04 31 39.00	19.47	NOT	2×600
eHAQ 0007+1445	00 07 42.10	+14 45 28.60	19.31	NOT	2×900
eHAQ 0019+0657	00 19 57.30	+06 57 45.90	19.42	NOT	2×900
eHAQ 0026+0708	00 26 11.40	+07 08 41.30	19.24	NOT	2×600
eHAQ 0044+1321	00 44 56.40	+13 21 48.70	18.69	NOT	2×600
eHAQ 0102+1159	01 02 52.90	+11 59 48.40	20.25	NOT	1×900
eHAQ 0104+0756	01 04 17.10	+07 56 35.20	18.82	NOT	2×600
eHAQ 0104+0912	01 04 11.70	+09 12 38.50	19.29	NOT	2×600
eHAQ 0104+1506	01 04 07.00	+15 37 39.80	18.89	NOT	3×1000
eHAQ 0109+0435	01 09 11.20	+04 35 44.20	19.58	NOT	2×900
eHAQ 0111+0641	01 11 34.70	+06 41 19.20	18.82	NOT	2×900
eHAQ 0113+0804	01 13 55.40	+08 04 25.70	18.95	NOT	2×600
eHAQ 0121+1028	01 21 34.40	+10 28 34.20	20.69	NOT	2×1200
eHAQ 0129+0638	01 29 50.60	+06 38 46.00	19.64	NOT	2×1300
eHAQ 0129+1039	01 29 19.00	+10 39 43.20	20.34	NOT	2×1200
eHAQ 0138+0742	01 38 14.40	+07 42 35.50	19.29	NOT	2×600
eHAQ 0142+0257	01 42 06.90	+02 57 13.10	18.10	NOT	2×600
eHAQ 0147+0411	01 47 32.00	+04 11 13.40	18.34	NOT	2×700
eHAQ 0157+1321	01 57 01.50	+13 21 18.80	18.98	NOT	3×1200
eHAQ 0216+0426	02 16 43.30	+04 26 28.80	19.88	NOT	2×1200
eHAQ 0227+0521	02 27 57.90	+05 21 41.90	19.30	NOT	1×600
eHAQ 0300+0440	03 00 02.50	+04 40 04.90	19.49	NOT	2×600
eHAQ 0321+0523	03 21 52.20	+05 23 37.40	19.36	NOT	1×900
eHAQ 0347+0348	03 47 34.20	+03 48 36.90	19.33	NOT	2×600
eHAQ 0828+0313	08 28 13.98	+03 13 54.32	17.59	NOT	3×200
eHAQ 0835+0127	08 35 15.80	+01 27 31.40	19.03	NOT	3×600
eHAQ 0835+0830	08 35 42.18	+08 30 10.42	17.62	NOT	3×200
eHAQ 0839+0556	08 39 02.86	+05 56 27.63	18.73	NOT	3×500
eHAQ 0852+0204	08 52 03.80	+02 04 37.80	19.78	NOT	3×900
eHAQ 0856+0643	08 56 28.30	+06 43 54.20	19.43	NOT	3×900
eHAQ 0913+0910	09 13 04.40	+09 10 44.20	18.10	NOT	3×250
eHAQ 0915+0115	09 15 35.57	+01 15 15.42	18.45	NOT	3×400
eHAQ 0919+0843	09 19 07.11	+08 43 05.04	19.44	NOT	3×900
eHAQ 0921+0149	09 21 42.00	+01 49 59.70	19.42	NOT	3×900
eHAQ 0923+0520	09 23 45.80	+05 20 26.40	19.03	NOT	3×600
eHAQ 0927 - 0233	09 27 40.00	-02 33 47.50	19.65	NOT	3×900
eHAQ 0930+0148	09 30 45.10	+01 48 46.70	19.78	NOT	3×900
eHAQ 0940+0532	09 40 51.40	+05 32 13.30	18.60	NOT	3×500
eHAQ 0943+0954	09 43 49.70	+09 54 00.90	18.93	NOT	3×600
eHAQ 0943+1300	09 43 33.00	+13 00 55.70	19.42	NOT	3×600
eHAQ 0949+1207	09 49 47.00	+12 07 56.20	19.41	NOT	2×600
eHAQ 0950+0440	09 50 04.10	+04 40 40.40	19.41	NOT	3×600
eHAQ 0952+0835	09 52 03.00	+08 35 55.80	19.69	NOT	3×900

Table 2.1: *Continued*

Target	**R.A. (J 2000)**	**Decl. (J 2000)**	$\mathbf{r_{SDSS}}$ **(mag)**	**Telescope**	**Exp. time (sec)**
eHAQ 1002+0406	10 02 51.29	+04 06 53.98	18.42	NOT	3×400
eHAQ 1005+0602	10 05 01.80	+06 02 19.90	19.85	NOT	2×900
eHAQ 1010+1158	10 10 54.00	+11 58 05.70	18.95	NOT	3×600
eHAQ 1025+1324	10 25 18.62	+13 24 11.96	18.80	NOT	3×500
eHAQ 1026 - 0241	10 26 00.90	-02 41 17.10	19.69	NOT	2×900
eHAQ 1030+1040	10 30 32.60	+10 40 51.30	17.78	NOT	3×200
eHAQ 1101+1220	11 01 20.02	+12 20 31.82	18.81	NOT	3×500
eHAQ 1106+0844	11 06 35.80	+08 44 02.30	19.35	NOT	3×900
eHAQ 1109+0135	11 09 02.30	+01 35 38.86	18.42	NOT	3×400
eHAQ 1109+1058	11 09 24.80	+10 58 25.40	19.83	NOT	2×900
eHAQ 1111+0151	11 11 37.68	+01 51 47.31	18.33	NOT	3×360
eHAQ 1119+1430	11 19 39.70	+14 30 00.80	19.37	NOT	3×600
eHAQ 1120+0812	11 20 03.60	+08 12 12.10	16.91	NOT	3×100
eHAQ 1132+1243	11 32 07.20	+12 43 42.10	18.87	NOT	3×600
eHAQ 1136+0027	11 36 44.10	+00 27 00.30	19.96	NOT	3×900
eHAQ 1144+0902	11 44 45.40	+09 02 26.60	18.88	NOT	3×600
eHAQ 1202+0423	12 02 04.90	+04 23 41.00	19.04	NOT	2×600
eHAQ 1203+0652	12 03 36.90	+06 52 34.50	19.85	NOT	3×900
eHAQ 1203+1118	12 03 34.00	+11 18 26.00	19.45	NOT	3×900
eHAQ 1210+1429	12 10 21.00	+14 29 58.60	17.38	NOT	3×200
eHAQ 1222+0826	12 22 15.00	+08 26 10.20	19.64	NOT	2×900
eHAQ 1226 - 0236	12 26 55.30	-02 36 57.90	19.64	NOT	3×900
eHAQ 1237+1233	12 37 26.50	+12 33 50.02	19.85	NOT	2×900
eHAQ 1244+0841	12 44 18.80	+08 41 36.00	19.13	NOT	3×800
eHAQ 1252+0842	12 52 57.70	+08 42 06.10	18.79	NOT	3×600
eHAQ 1312+1431	13 12 14.20	+14 31 11.30	19.54	NOT	2×900
eHAQ 1326+1317	13 26 24.80	+13 17 27.50	18.11	NOT	6×300
eHAQ 1331+1304	13 31 29.89	+13 04 20.87	19.02	NOT	3×600
eHAQ 1340+1458	13 40 53.90	+14 58 53.80	19.67	NOT	2×900
eHAQ 1346+0114	13 46 32.40	+01 14 08.40	19.37	NOT	3×900
eHAQ 1357 - 0051	13 57 30.60	-00 51 41.10	18.40	NOT	3×300
eHAQ 1400+0720	14 00 39.20	+07 20 12.00	19.72	NOT	2×900
eHAQ 1443+0415	14 43 58.20	+04 15 42.47	19.00	NOT	3×600
eHAQ 1447+0521	14 47 21.60	+05 21 41.70	19.92	NOT	3×900
eHAQ 1450+1002	14 50 43.70	+10 02 38.80	19.56	NOT	2×900
eHAQ 1455+0705	14 55 10.52	+07 05 25.51	17.59	NOT	3×200
eHAQ 1504+0523	15 04 24.59	+05 23 07.11	18.50	NOT	3×400
eHAQ 1514 - 0002	15 14 01.90	-00 02 59.70	19.27	NOT	3×600
eHAQ 1525+0155	15 25 55.00	+01 55 13.50	19.88	NOT	3×900
eHAQ 1528+0546	15 28 53.60	+05 46 57.30	19.18	NOT	6×360
eHAQ 1539+0351	15 39 35.30	+03 51 25.60	17.95	NOT	3×360
eHAQ 1543+0447	15 43 27.30	+04 47 17.80	19.78	NOT	2×900
eHAQ 1550+0501	15 50 00.00	+05 01 28.00	19.85	NOT	3×900

Table 2.1: *Continued*

Target	**R.A. (J 2000)**	**Decl. (J 2000)**	**r_{SDSS} (mag)**	**Telescope**	**Exp. time (sec)**
eHAQ 2209+0304	22 09 20.40	+03 04 36.00	19.91	NOT	2×900
eHAQ 2235+0635	22 35 12.40	+06 35 45.50	19.29	NOT	2×400
eHAQ 2236+0731	22 36 09.40	+07 31 08.20	19.96	NOT	2×900
eHAQ 2247+0922	22 47 09.10	+09 22 33.50	19.82	NOT	2×900
eHAQ 2254+0638	22 54 32.30	+06 38 26.10	18.40	NOT	2×600
eHAQ 2255+1213	22 55 58.70	+12 13 10.90	19.14	NOT	2×600
eHAQ 2256+0531	22 56 43.90	+05 31 15.10	20.57	NOT	2×1500
eHAQ 2258+0251	22 58 43.00	+02 51 07.20	20.73	NOT	2×1500
eHAQ 2259+0208	22 59 55.80	+02 08 25.40	19.07	NOT	2×400
eHAQ 2259+0256	22 59 20.40	+02 56 43.80	19.37	NOT	2×600
eHAQ 2259+0736	22 59 17.80	+07 36 33.50	19.66	NOT	2×1000
eHAQ 2301+0752	23 01 59.40	+07 52 39.00	19.77	NOT	2×900
eHAQ 2303+0747	23 03 00.30	+07 47 36.80	19.12	NOT	5×1080
eHAQ 2309+1159	23 09 14.80	+11 59 56.00	19.69	NOT	2×900
eHAQ 2310+0447	23 10 44.00	+04 47 46.80	19.78	NOT	2×900
eHAQ 2313+1259	23 13 24.40	+12 59 39.00	19.71	NOT	2×900
eHAQ 2314+0552	23 14 53.40	+05 52 33.10	19.92	NOT	2×1000
eHAQ 2316+0651	23 16 07.10	+06 51 45.10	19.93	NOT	2×1000
eHAQ 2321+1107	23 21 51.30	+11 07 20.70	18.38	NOT	2×300
eHAQ 2321+1121	23 21 52.30	+11 21 28.50	19.92	NOT	2×1000
eHAQ 2334+1519	23 34 21.50	+15 19 47.60	20.74	NOT	2×1200
eHAQ 2340+0121	23 40 54.30	+01 21 41.30	18.82	NOT	2×500
eHAQ 2344+1416	23 44 51.90	+14 16 40.40	18.90	NOT	2×500
eHAQ 2358+1030a	23 58 40.50	+10 30 39.90	20.82	NOT	2×1200
eHAQ 2358+1030b	23 58 40.53	+10 30 35.53	20.37	NOT	2×1200

Table 2.2: The results of the spectroscopic follow-up.

Target	**Type**	$\mathbf{z}_{\mathrm{QSO}}$	A_V	**Notes**
eHAQ 0001+0233	QSO	1.88	0.23	
eHAQ 0001+0431	QSO	1.96	0.60	
eHAQ 0007+1445	QSO	1.37	0.91	
eHAQ 0019+0657	QSO	3.40	0.28	
eHAQ 0026+0708	QSO	1.78	0.64	
eHAQ 0044+1321	QSO	1.70	0.38	
eHAQ 0102+1159	QSO	4.25	0.53	
eHAQ 0104+0756	QSO	2.21	0.23	
eHAQ 0104+0912	QSO	2.03	0.24	
eHAQ 0104+1506	QSO	1.80	0.45	
eHAQ 0109+0435	QSO	3.85	0.45	
eHAQ 0111+0641	QSO	3.23	0.32	
eHAQ 0113+0804	QSO	2.01	0.64	
eHAQ 0121+1028	QSO	2.10	0.53	
eHAQ 0129+0638	QSO	2.40	0.60	
eHAQ 0129+1039	QSO	1.10	0.98	
eHAQ 0138+0742	QSO	2.38	0.26	
eHAQ 0142+0257	QSO	2.30	0.45	
eHAQ 0147+0411	QSO	1.77	0.38	
eHAQ 0157+1321	QSO	1.73	0.38	
eHAQ 0216+0426	QSO	1.58	0.76	
eHAQ 0227+0521	QSO	2.68	0.18	
eHAQ 0300+0440	QSO	1.88	0.33	
eHAQ 0321+0523	QSO	2.95	0.30	
eHAQ 0347+0348	QSO	1.87	0.20	
eHAQ 0828+0313	QSO	2.00	0.70	
eHAQ 0835+0127	QSO	3.30	0.20	
eHAQ 0835+0830	G/M-dwarf	0.00	0.00	$J-K=-0.14$
eHAQ 0839+0556	QSO	1.49	0.60	
eHAQ 0852+0204	QSO	2.20	0.53	
eHAQ 0856+0643	QSO	2.49	0.50	
eHAQ 0913+0910	QSO	1.95	0.50	
eHAQ 0915+0115	G/M-dwarf	0.00	0.00	$J-K=-0.23$
eHAQ 0919+0843	QSO	2.43	0.30	
eHAQ 0921+0149	QSO	0.99	1.80	
eHAQ 0923+0520	QSO	3.40	0.20	
eHAQ 0927 - 0233	QSO	1.24	0.83	
eHAQ 0930+0148	QSO	2.95	0.30	
eHAQ 0940+0532	QSO	2.22	0.30	
eHAQ 0943+0954	QSO	4.25	0.00	
eHAQ 0943+1300	QSO	2.10	0.60	
eHAQ 0949+1207	QSO	3.36	0.00	
eHAQ 0950+0440	QSO	2.30	0.53	
eHAQ 0952+0835	QSO	1.86	0.60	

Table 2.2: *Continued*

Target	**Type**	$\mathbf{z}_{\mathrm{QSO}}$	A_V	**Notes**
eHAQ 1002+0406	G/M-dwarf	0.00	0.00	$J-K=-0.14$
eHAQ 1005+0602	QSO	2.56	0.49	
eHAQ 1010+1158	QSO	2.24	0.40	
eHAQ 1025+1324	QSO	2.57	1.30	
eHAQ 1026 - 0241	QSO	3.23	0.15	
eHAQ 1030+1040	Unknown	0.00	0.00	
eHAQ 1101+1220	QSO	3.20	0.50	
eHAQ 1106+0844	QSO	1.86	0.45	
eHAQ 1109+0135	G/M-dwarf	0.00	0.00	$J-K=-0.16$
eHAQ 1109+1058	QSO	1.90	0.38	
eHAQ 1111+0151	G/M-dwarf	0.00	0.00	$J-K=-0.14$
eHAQ 1119+1430	QSO	1.88	0.38	
eHAQ 1120+0812	G/M-dwarf	0.00	0.00	$J-K=0.06$
eHAQ 1132+1243	Unknown	0.00	0.00	
eHAQ 1136+0027	QSO	1.12	1.36	
eHAQ 1144+0902	QSO	1.78	0.50	
eHAQ 1202+0423	QSO	2.32	0.00	
eHAQ 1203+0652	QSO	2.40	0.30	
eHAQ 1203+1118	QSO	3.62	0.00	
eHAQ 1210+1429	QSO	1.48	1.20	
eHAQ 1222+0826	QSO	2.85	0.15	
eHAQ 1226 - 0236	QSO	1.25	0.83	
eHAQ 1237+1233	QSO	2.28	0.30	
eHAQ 1244+0841	QSO	1.87	0.55	
eHAQ 1252+0842	QSO	3.56	0.00	
eHAQ 1312+1431	QSO	1.64	0.38	
eHAQ 1326+1317	QSO	2.00	0.50	
eHAQ 1331+1304	G/M-dwarf	0.00	0.00	$J-K=-0.20$
eHAQ 1340+1458	QSO	1.73	0.53	
eHAQ 1346+0114	QSO	1.73	1.30	
eHAQ 1357 - 0051	QSO	1.80	0.53	
eHAQ 1400+0720	QSO	2.40	0.15	
eHAQ 1443+0415	QSO	1.54	0.00	
eHAQ 1447+0521	QSO	2.33	0.45	
eHAQ 1450+1002	QSO	1.58	0.38	
eHAQ 1455+0705	QSO	1.90	0.80	
eHAQ 1504+0523	G/M-dwarf	0.00	0.00	$J-K=-0.18$
eHAQ 1514 - 0002	QSO	2.00	0.15	
eHAQ 1525+0155	QSO	1.62	0.91	
eHAQ 1528+0546	QSO	2.12	0.50	
eHAQ 1539+0351	QSO	1.63	0.43	
eHAQ 1543+0447	QSO	2.05	0.72	
eHAQ 1550+0501	QSO	1.48	0.76	

Table 2.2: *Continued*

Target	**Type**	$\mathbf{z}_{\mathrm{QSO}}$	A_V	**Notes**
eHAQ 2209+0304	QSO	2.33	0.60	
eHAQ 2235+0635	QSO	1.33	1.06	
eHAQ 2236+0731	QSO	1.72	0.23	
eHAQ 2247+0922	QSO	1.65	0.68	
eHAQ 2254+0638	QSO	1.50	0.76	
eHAQ 2255+1213	QSO	2.05	0.15	
eHAQ 2256+0531	QSO	1.35	1.13	
eHAQ 2258+0251	QSO	2.43	0.42	
eHAQ 2259+0208	QSO	2.05	0.38	
eHAQ 2259+0256	QSO	1.50	0.76	
eHAQ 2259+0736	QSO	0.78	1.29	
eHAQ 2301+0752	QSO	2.62	0.26	
eHAQ 2303+0747	QSO	1.31	0.60	
eHAQ 2309+1159	QSO	2.00	0.57	
eHAQ 2310+0447	QSO	1.42	0.45	
eHAQ 2313+1259	QSO	2.11	0.45	
eHAQ 2314+0552	QSO	2.03	0.30	
eHAQ 2316+0651	QSO	1.37	0.60	
eHAQ 2321+1107	QSO	1.56	0.60	
eHAQ 2321+1121	QSO	2.18	0.38	
eHAQ 2334+1519	QSO	2.25	0.83	
eHAQ 2340+0121	QSO	2.17	0.38	
eHAQ 2344+1416	QSO	2.52	0.53	
eHAQ 2358+1030a	QSO	2.06	1.13	
eHAQ 2358+1030b	QSO	1.68	0.00	Non-eHAQ

Chapter 3

Conclusions

In the first part of my thesis I chronologically outlined the different approaches with which QSOs have been discovered. Here I also discussed how the population of dust-reddened QSOs contribute to the total QSO population.

In the second part of my thesis I presented a tailored search for dust-reddened QSOs, which was the third and latest phase of the High A_V Quasar (HAQ) survey. The aim for this extended HAQ (eHAQ) survey, and the initial HAQ survey as well, was to detect and study metal-rich and dusty foreground galaxies, e.g., damped Lyman-α absorbers (DLAs). DLAs have previously been selected towards background QSOs, which in the majority of cases are selected based on their blue optical colors, in for instance the SDSS legacy survey. If the absorbing gas is rich in metals and cold gas, however, the dust column density might also be high causing the background QSO to appear redder. This way, the QSOs will not be selected in present optical samples and the chemically enriched DLAs will escape our analyses as well.

To overcome this bias I (together with my supervisor and collaborators, see the last co-author statement in the Appendix) specifically searched for dust-reddened QSOs, with a selection based on well-defined optical and near/mid-infrared color criteria, with the aim of detecting these elusive DLAs. By combining the optical and near/mid-infrared photometric data from the SDSS, UKIDSS and *WISE* surveys, respectively, it is possible to break the degeneracy of QSOs with optical stellar-like colors. In particular, the near-infrared K-band excess of QSOs compared to that of stars was used in a combination with the mid-infrared *WISE* colors, to effectively remove stellar contamination. Moreover, the mid-infrared colors allow for a robust rejection of QSOs at low redshift, reddened by intrinsic clouds of dust, irrelevant to the search for DLAs. To remove any possible contamination of compact galaxies, a conservative lower limit in the $W1 - W2$ color of the targets was set, which I found unfortunately also removed several QSOs at $z > 3$, compared to the previous HAQ survey. Even though the survey was successful in removing most intrinsically reddened QSOs at $z < 1$, about 50% of the eHAQ sample consisted of broad absorption line (BAL) QSOs. Although interesting on their own, these were not the primary goal of the eHAQ survey so the selection needs to be even more fine-tuned. In the next chapter I will outline the future work on this subject and discuss a more optimized set of optical to near/mid-infrared selection criteria, which hopefully will reveal several more QSOs with intervening, dusty galaxies.

As an added value to the search for dusty DLAs, we discovered a large number of intrinsically dust-reddened and high-z QSOs in our samples, which are missing in present optically selected QSO samples, e.g., SDSS. That is, we detect a population of QSOs which have been underrepresented in present large area QSO surveys.

Chapter 4

Outlook and Future Work

This last chapter is dedicated to summarize the recently initiated projects of which I am currently involved in. The quest for dust-reddened QSOs is currently being continued, where the aim is to target even fainter and redder QSOs than previous. In particular, after the completion of the three phases described in Paper I, II (Fynbo et al., 2013; Krogager et al., 2015) and Chapter 2 I am convinced that an even more optimized selection algorithm is necessary in the search for dusty absorption systems.

4.1 Mining the KiDS and VIKING surveys for red QSOs

After completion of the first three phases (described in Paper I and II: Fynbo et al., 2013; Krogager et al., 2015, and Chapter 2) aimed to detect and study metal-rich and dusty foreground galaxies, our sample now exceeds 300 previously unknown dust-reddened QSOs. In Paper I, $\sim$ 20% of the observed sample was found to be contaminating stellar or extragalactic sources and of the confirmed QSOs only objects with intrinsic reddening were observed. From Paper I to II the selection criteria were refined to exclude most of the contaminants and to target more dust-reddened QSOs to reach the goal of detecting sources reddened by dusty foreground galaxies. Here the authors obtained an almost pure sample ($\sim$ 97% confirmed QSOs) and found a handful of systems with intervening foreground galaxies. Such galaxies, too faint to be detected in emission, are of crucial importance to the star formation inventory in the universe as they are expected to be numerous.

The goal is now to extend these surveys to locate fainter and more reddened sources. By identifying redder QSOs the aim is to detect the sources that are even more reddened by metal-rich and dusty foreground galaxies than what has been observed in the HAQ and eHAQ surveys. From the initial surveys it is easy to realize that dusty absorbers do exist towards red QSOs (in roughly 2 per cent of the cases) and that the dust reddening causes the QSOs to escape optical identification. However, we (the collaborators on this project and I) have only begun to probe the tip of the iceberg. In order to detect more dusty systems we need to target even redder and fainter candidates, as the larger dust content absorbs more of the light from the background QSO. This limits our ability to use the SDSS and UKIDSS photometry which formed the basis for the previous HAQ and eHAQ surveys. Instead we use a deeper catalog from a combination of data release 2 (DR2) of the public Kilo-Degree Survey (KiDS; de Jong et al., 2015) and the VISTA Kilo-Degree Infrared Galaxy (VIKING; Arnaboldi et al., 2007) survey. These new public surveys together with mid-infrared photometry from the *WISE* all-sky survey form the basis for the target selection in the latest, recently commenced survey. In particular, we wish to target red QSOs at $z > 2.5$, which are the most interesting for our primary goal to explore the issue of dusty DLAs.

This new approach is similar to the one utilized in the eHAQ survey (Chapter 2) where the *WISE* colors are used to effectively remove the low-z population of intrinsically reddened QSOs and the optical/NIR colors are used to target red sources and to remove stellar contamination. However, as described in Chapter 2, the *WISE* colors only are not capable of removing contaminating dwarf stars from the samples. To also remove possible contaminating galaxies from the sample a conservative lower cut in $W1 - W2$ was invoked in the eHAQ survey which unfortunately also removed most of the reddened QSOs at $z > 3$. Based on the knowledge obtained from the spectroscopic follow-up campaign of the eHAQ survey we are now able to further optimize our selection of QSOs with intervening foreground galaxies.

The refined color criteria were defined by combining information from the optical (KiDS) and infrared (VIKING and *WISE*) missions. Our criteria are as follows (see also Fig. 4.1):

Optical/near-infrared point sources based on KiDS and VIKING imaging,

$$0.5 < g - r < 2.5 \quad , \quad 0.0 < r - i < 1.0 \quad , \quad J < 20 \ ,$$

$$J - K > 0.3 \ \& \ g - r > 1.5 \quad \text{OR} \quad J - K > -0.2 \ \& \ g - r < (2 \times [J - K] + 0.90) \ ,$$

$$W1 - W2 > 0.2 \ , \ 2.0 < W2 - W3 < 4.2 \ , \ W1 - W2 < 0.8 \ \& \ W2 - W3 < 2.75 \ ,$$

$$\text{OR} \quad W2 - W3 > 2.75 \ \& \ W1 - W2 < (0.62 \times [W2 - W3] - 0.91) \ .$$

(note: W1, W2 and W3 refer to the 3.4 μm, 4.6 μm and 12 μm bands respectively. The *WISE*

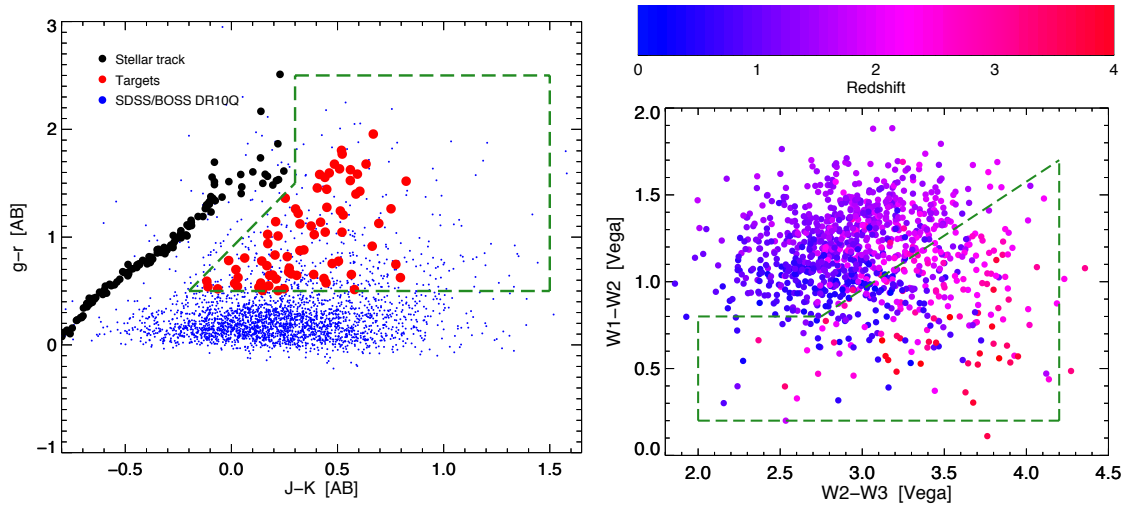

Figure 4.1: *Left panel:* A $g-r$ vs. $J-K$ color-color diagram illustrating our optical/near-infrared selection criteria. The selection region is marked with a green dashed box and the individual targets marked with red dots. Also shown is the stellar track (black points) and the SDSS/BOSS DR10 QSO sample (blue dots). *Right panel:* A $W1-W2$ vs. $W2-W3$ color-color diagram illustrating our MIR selection criteria. The selection region is again marked with a green dashed box shown together with a subsample of the SDSS/BOSS DR10 QSO sample matched to *WISE*, color coded as a function of redshift. These criteria allow us to optimize our selection to identify QSOs at $z > 2.5$.

magnitudes are on the Vega system and the g, r, J and K magnitudes are on the AB system).

First, we required that all candidates are point sources in both optical and NIR imaging to remove objects in which the host galaxy of the AGN contributes significantly to the observed light. The first optical color criteria ensures the red nature of the targets (where most QSOs have $g-r < 0.5$, see Fig. 4.1) and that the objects are bright enough for spectroscopic follow-up with e.g., the NOT. The optical/NIR selection criteria effectively remove stellar contamination (again, see Fig. 4.1) and the *WISE* colors are defined in such a way that most of the population of reddened QSOs at $z \lesssim 2.5$ is removed prior to observation. The *WISE* colors are only slightly modified compared to the selection criteria of the eHAQ survey, but we expect that this new approach will effectively remove most of the population of broad absorption line (BAL) QSOs at $z \sim 2$ which contributed significantly ($\sim 50\%$) to the eHAQ survey. Although still an interesting sub-class on their own, about a hundred BAL QSOs have already been observed as part of the HAQ and eHAQ surveys, whereas only about a dousin damped Lyman-α absorbers (DLAs) have been detected. We also revoked the too conservative $W1-W2$ color cut of the eHAQ survey to remove the bias against $z > 3$ QSOs.

Appendices

Appendix A

Serendipitous Discovery of a Projected Pair of QSOs Separated by 4.5 arcsec on the Sky, The Astronomical Journal, Vol. 152, 13 (2016). Authors: Heintz, K. E., Fynbo, J. P. U., Krogager, J.-K., Vestergaard, M., Møller, P., Arabsalmani, M., Geier, S., Noterdaeme, P. Ledoux, C., Saturni, F. G., Venemans, B.

Co-author statement:
In this work, which is based on a serendipitous discovery, I was the PI for the fast-track proposal submitted to the NOT to obtain follow-up spectroscopy of the two targets, I did the whole analysis for the two objects and wrote the initial version of the text. The co-authors have contributed at the level of commenting on the text and figures and making suggestions for changes of these. The referee suggested an alternative calculation of the likelihood of observing two, this proximate, quasars.

The Astronomical Journal, 152:13 (4pp), 2016 July doi:10.3847/0004-6256/152/1/13

SERENDIPITOUS DISCOVERY OF A PROJECTED PAIR OF QSOs SEPARATED BY 4.5 arcsec ON THE SKY*

K. E. Heintz[1,10], J. P. U. Fynbo[1], J.-K. Krogager[1,6], M. Vestergaard[1,2], P. Møller[3], M. Arabsalmani[3], S. Geier[4,5], P. Noterdaeme[6], C. Ledoux[7], F. G. Saturni[8], and B. Venemans[9]

[1] Dark Cosmology Centre, Niels Bohr Institute, University of Copenhagen, Juliane Maries Vej 30, DK-2100 Copenhagen O, Denmark; heintz@dark-cosmology.dk
[2] Steward Observatory, University of Arizona, 933 N. Cherry Avenue, Tucson AZ 85721, USA
[3] European Southern Observatory, Karl-Schwarzschildstrasse 2, D-85748 Garching, Germany
[4] Gran Telescopio Canarias (GRANTECAN), Cuesta de San José s/n, E-38712, Breña Baja, La Palma, Spain
[5] Instituto de Astrofísica de Canarias, Vía Láctea s/n, E-38200, La Laguna, Tenerife, Spain
[6] Institut d'Astrophysique de Paris, CNRS-UPMC, UMR7095, 98bis bd Arago, F-75014 Paris, France
[7] European Southern Observatory, Alonso de Crdova 3107, Vitacura, Casilla 19001, Santiago 19, Chile
[8] University of Rome "La Sapienza", p.le A. Moro 5, I-00185 Rome, Italy
[9] Max-Planck Institute for Astronomy, Königstuhl 17, D-69117 Heidelberg, Germany
Received 2016 February 16; accepted 2016 April 15; published 2016 June 21

ABSTRACT

We present the serendipitous discovery of a projected pair of quasi-stellar objects (QSOs) with an angular separation of $\Delta\theta = 4.50$ arcsec. The redshifts of the two QSOs are widely different: one, our program target, is a QSO with a spectrum consistent with being a narrow line Seyfert 1 active galactic nucleus at $z = 2.05$. For this target we detect Lyα, C IV, and C III]. The other QSO, which by chance was included on the spectroscopic slit, is a Type 1 QSO at a redshift of $z = 1.68$, for which we detect C IV, C III], and Mg II. We compare this system to previously detected projected QSO pairs and find that only about a dozen previously known pairs have smaller angular separation.

Key words: quasars: general

1. INTRODUCTION

We report the discovery of a closely projected pair of quasi-stellar objects (QSOs) with an angular separation of only $\Delta\theta = 4.50$ arcsec. The observing run from which the spectra of these two objects were obtained was unrelated to the search for close projected QSO pairs. Originally, the run was designed to spectroscopically verify candidate dust-reddened QSOs, as part of the High A_V Quasar (HAQ) survey (Fynbo et al. 2013; Krogager et al. 2015). The dust-reddened candidate QSO originally intended to be verified spectroscopically, HAQ2358 +1030A, J2000 coordinates $\alpha_A = 23^{\rm h}\,58^{\rm m}\,40\overset{\rm s}{.}47$, $\delta_A = +10^{\rm o}\,30^{\rm m}\,40\overset{\rm s}{.}07$, will henceforth just be denoted as object A. The companion "HAQ"2358+1030B with J2000 coordinates ($\alpha_B = 23^{\rm h}\,58^{\rm m}\,40\overset{\rm s}{.}53$, $\delta_B = +10^{\rm o}\,30^{\rm m}\,35\overset{\rm s}{.}53$, will be denoted as object B. The companion QSO was discovered serendipitously, coincidentally placed on the slit during the target acquisition of object A. The slit was aligned at the parallactic angle.

The small angular separation of this projected pair of QSOs is quite unusual and will be discussed briefly in Section 4. Previously, Hennawi et al. (2006b) carried out an extensive search for binary QSO systems, using the Sloan Digital Sky Survey (SDSS; York et al. 2000) and the 2dF QSO Redshift Survey (2QZ; Croom et al. 2004) QSO catalogs. They primarily focused on selecting binary QSO pairs, the controversial population discovered in the search for small-scale $2 \leqslant \Delta\theta \leqslant 10$ arcsec gravitationally lensed QSOs (e.g., Mortlock et al. 1999), to study the small-scale QSO clustering and correlation function. However, the majority of the detected QSO pair systems were projected systems, having relative radial separations of $\Delta z \approx 0.3$–1.0. The discovery of these close angularly separated projected QSO pairs initiated the search and study of "quasars probing quasars" (see e.g., Hennawi et al. 2006a, and later papers). Close binary QSOs and projected QSO pairs are important for studies of small-scale QSO clustering, the tomography of the inter-galactic medium along close lines of sight, the effects of QSO transverse ionization (Møller & Kjaergaard 1992), and gravitationally lensed QSOs.

Throughout this paper we assume the standard ΛCDM cosmology with $H_0 = 70\,{\rm km\,s^{-1}\,Mpc^{-1}}$, $\Omega_M = 0.28$, and $\Omega_\Lambda = 0.72$ (Komatsu et al. 2011).

2. OBSERVATIONS

In Figure 1 we present a 1×1 arcmin^2 field around the two sources (marked A and B) as imaged in the *i*-band by SDSS in Data Release 12 (DR12) (Alam 2015).

The observation was carried out during an observing run with the Nordic Optical Telescope (NOT) on La Palma in 2015 September. The spectra were obtained using the Andalucia Faint Object Spectrograph and Camera (ALFOSC), grism #4 covering the wavelengths 3200–9100 Å (with a spectral resolution of 21 Å) and a slit width of 1.3 arcsec. Blocking filter #94 was used in order to prevent second-order contamination from wavelengths shorter than 3560 Å. Two exposures of 1200 s were taken. The object south of our program target is the one captured serendipitously.

One additional spectrum was taken on 2016 January 9 in a redder grism (grism #20). This spectrum was taken again with a position angle covering both QSOs. A total exposure time of 3200 s was secured. The purpose of this spectrum was to confirm that an unidentified emission line in the spectrum of object A was due to second-order contamination (see below).

* Based on observations made with the Nordic Optical Telescope, on the island of La Palma jointly operated by Denmark, Finland, Iceland, Norway, and Sweden, in the Spanish Observatorio del Roque de los Muchachos of the Instituto de Astrofisica de Canarias.
[10] Author to whom correspondence should be addressed.

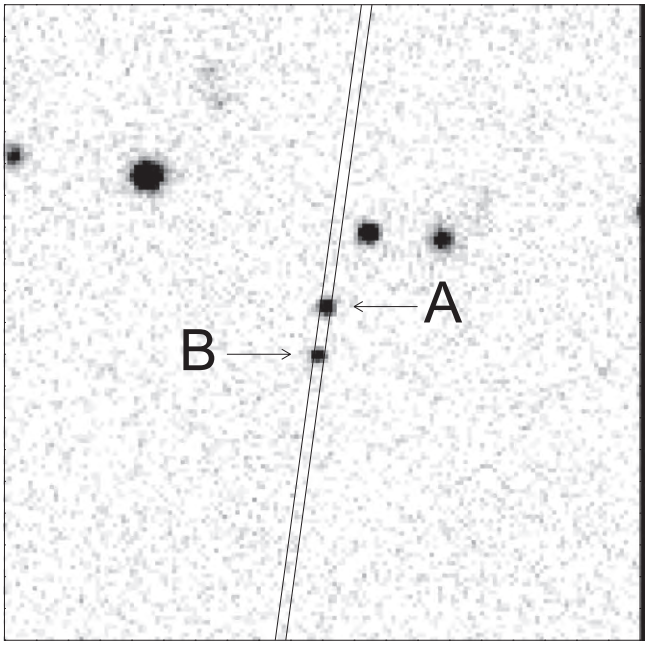

Figure 1. A 1×1 arcmin^2 field around the two sources (marked A and B) as imaged in the *i*-band by SDSS DR12. North is up and east is to the left. A schematic view of the actual slit, used during the observation, which was centered on source A and aligned with the parallactic angle ($-7.^\circ7$ east of north (EoN) at the time) is shown. The position angle between the two objects is $-10.^\circ1$ EoN.

The spectra were processed using a combination of IRAF[11] and MIDAS[12] tasks for low resolution spectroscopy. To reject cosmic rays we used La_cosmic (van Dokkum 2001). We corrected the spectra for Galactic extinction using the extinction maps of Schlegel et al. (1998). To improve the absolute flux calibration we scaled the spectra to be consistent with the *r*-band photometry from SDSS.

3. THE PROJECTED QSO PAIR HAQ2358+1030A AND B

The projected angular separation between the two objects is ~4.6 arcsec as measured on the SDSS images.[13] Based on the acquisition picture obtained we find a projected angular separation of only 23.5 pixels = 4.50 arcsec (0.19 arcsec/pixel for ALFOSC). This corresponds to a physical angular separation of 39.2 kpc at $z = 1.5$. Since our measurement is taken directly from the acquisition picture, we consider this a more precise estimate of the angular separation of the two objects due to the better spatial resolution in these data.

Figure 2 shows the two one-dimensional spectra after flat-field correction, bias and sky subtraction, and flux calibration along with the photometry from SDSS and the UKIRT Infrared Deep Sky Survey (UKIDSS; Lawrence et al. 2007) which are all on the AB magnitude system. We determine the redshift by visual inspection of the emission lines visible in the spectra.

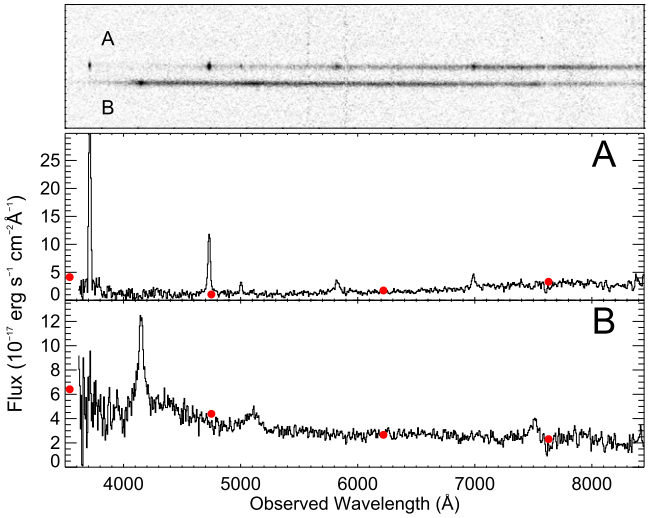

Figure 2. Top panel: the 2D spectrum showing the traces of the two sources marked with A and B. Middle and bottom panels: the 1D spectra of the two sources. The observed spectra are plotted as the solid black lines and the photometric data points from SDSS are shown as the red dots (left to right: *u*, *g*, *r*, *i*). The spectra have been scaled to match the *r*-band photometric data point from SDSS. Object A is a QSO equivalent of a narrow line Seyfert 1 galaxy at $z = 2.05$ whereas B is a Type 1 QSO at $z = 1.68$.

Table 1 lists the optical and near-infrared AB magnitudes for each of the two objects from the SDSS DR12 and the UKIDSS DR10plus catalogs.

In Table 2 we list the wavelengths, line widths (full width at half maximum, FWHM), and derived redshifts for the detected emission lines for the two objects. Object A is identified as a dust-reddened QSO equivalent of a narrow line Seyfert 1 galaxy classified by its narrow C IV λ1549 emission line with a FWHM of 920 km s^{-1}. The redshift is determined to be $z = 2.053$ based on the visible Lyα and the C IV, C III] λ1909 emission lines. There is an additional emission line in this spectrum at rest wavelength 2289 Å. This line is not prominent in the the empirical ultraviolet template for iron emission in active galactic nucleus derived from I Zwicky 1 (Vestergaard & Wilkes 2001) and we have not been able to find it in other spectra for QSOs in the literature. The new spectrum obtained in 2016 January at the NOT with grism #20 confirms that this line is due to second-order contamination (Stanishev 2007) and is hence not real.

The reddening of this object was determined to be $A_V = 1.1$ from the photometric data points and the shape of the continuum following the procedure of Fynbo et al. (2013) and Krogager et al. (2015). Object B is identified to be a regular, unreddened Type 1 QSO with a FWHM of 4200 km s^{-1} of the C IV emission line. The redshift was determined to be $z = 1.68$ based on the broad C IV and C III] emission lines. The unobscured nature of this object was again determined from the photometric data points and the shape of the continuum.

The redshift measurements suggest a relative radial distance of $\Delta z = 0.38$ between the two QSOs. Only about a dozen other systems of projected QSO pairs with $\Delta\theta < 4.50$ arcsec have been reported in the systematic search by Hennawi et al. (2006a, see Tables 8 and 9), Inada et al. (2012), and More et al. (2016), all with relative radial distances $\Delta z \sim 0.3$–1.1. It is also worth noting that neither of these two QSOs are included in the DR12 QSO survey. We selected object A as a candidate dust-

[11] IRAF is the Image Reduction and Analysis Facility, a general purpose software system for the reduction and analysis of astronomical data. IRAF is written and supported by the National Optical Astronomy Observatories (NOAO) in Tucson, Arizona. NOAO is operated by the Association of Universities for Research in Astronomy (AURA), Inc. under cooperative agreement with the National Science Foundation

[12] ESO-MIDAS is a copyright protected software product of the European Southern Observatory. The software is available under the GNU General Public License.

[13] http://skyserver.sdss.org/dr12/en/tools/explore/Summary.aspx?

Table 1
The Optical and Near-infrared Magnitudes of Objects A and B all on the AB Magnitude System from the SDSS and UKIDSS Catalogs

Object	u (mag)	g (mag)	r (mag)	i (mag)	z (mag)	Y (mag)	J (mag)	H (mag)	K_s (mag)
A	21.37	22.10	20.82	19.62	18.92	18.62	18.21	17.71	17.24
B	20.90	20.54	20.37	20.01	20.01	20.06	20.07	19.74	19.71

Table 2
Wavelength, Line Widths (Measured and Corrected for the Spectral Resolution), and Derived Redshifts for all Detected Emission Lines

Line	λ_{obs} (Å)	FWHM (Å)	FWHM_{corr} (Å)	z
Object A				
Lyα λ1216	3711.8 ± 0.5	20.0 ± 1.2	12.3 ± 1.2	2.0533 ± 0.0004
C IV λ1549	4731.0 ± 0.4	24.8 ± 0.9	14.5 ± 0.9	2.0533 ± 0.0004
He II λ1640	5003.7 ± 1.3	20.0 ± 0.9	...	2.0503 ± 0.0008
C III] λ1909	5825.1 ± 1.8	43.1 ± 4.5	35.3 ± 4.5	2.0530 ± 0.0008
Lyα 2nd order λ2289	6989.7 ± 1.4	36.2 ± 3.4	20.7 ± 3.4	2.053
Object B				
C IV λ1549	4149.7 ± 1.7	61.0 ± 4.1	58.4 ± 4.1	1.6781 ± 0.0011
C III] λ1909	5100.8 ± 5.8	124.4 ± 14.4	122.5 ± 14.4	1.673 ± 0.003
Mg II λ2800	7506.4 ± 3.8	63.1 ± 10.1	54.5 ± 10.1	1.6817 ± 0.0014

reddened QSO in the HAQ survey (see e.g., Fynbo et al. 2013; Krogager et al. 2015). Object B evaded selection due to its specific photometry falling outside the selection criteria of BOSS, which is optimized for $z > 2$.

We looked for associated absorption in the two spectra, more specifically absorption in the spectrum of object A due to, e.g., Mg II λ2800 or C IV due to gas associated with the foreground QSO object B. The continuum level in the spectrum of A is too weak at the position of C IV at the redshift of object B to allow detection of absorption. For Mg II we show the relevant spectral regions in Figure 3. There is a hint of Mg II absorption at 7490.2 Å with an observed equivalent width of 8 ± 3 Å found by integrating the error spectrum across the absorption line extent. This wavelength corresponds to $z_{abs} = 1.676$, roughly consistent, but slightly blueshifted, relative to the expected position at the redshift of object B.

4. THE SIGNIFICANCE OF CLOSELY SEPARATED QSO PAIRS

The projected pair of close angularly separated QSOs is a rare finding. Richards et al. (2005) find an integrated space density of QSOs brighter than $g = 20.5$ (brightness of object B) of ~31 deg^{-2} based on the 2dF-SDSS LRG and QSO (2SLAQ) survey. This intrinsic number density is based on robust optical five-band (u, g, r, i, z) color–color cuts similar to those utilized in the first SDSS QSO selection algorithm (Richards et al. 2002) although with slight modifications for the faintest objects. Based on the integrated space density, we estimated the likelihood of observing one additional QSO in the slit placed on object A. Considering only QSO pairs where (as in our case) the redshift difference corresponds to a distance much larger than the two-point correlation length, then the likelihood can be calculated as

$$\sim(31/3600/3600) \times 1.3 \times 10 \approx 3.1 \times 10^{-5}, \quad (1)$$

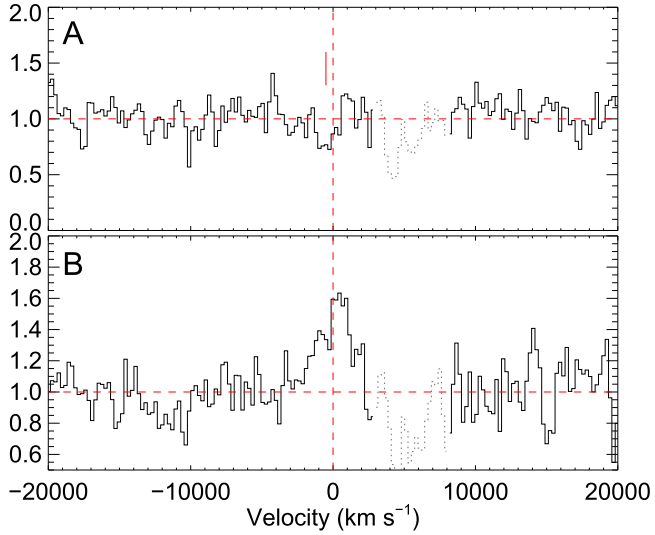

Figure 3. This figure shows the normalized spectra of object A and B in the regions around Mg II at the redshift of object B. In the top panel there is a hint of Mg II absorption with a formal significance of about 3σ. The part of the spectra shown in dotted gray represents telluric absorption.

where the last two numbers are the width of the slit and the length within which object B was detected (~2 × 5 arcsec) from object A, respectively. Had the observation been carried out just an hour later, the parallactic angle of the slit would not have captured this nearby companion, and we would not have discovered this system. When extrapolating the conservative total number of QSOs in the sky of ~31 × 41.253 deg^2 ≈ 1.3 × 10^6 and using the estimate of the likelihood per square degree we compute how many such cases on the entire sky is expected. We found a total of only ~140 cases of such closely separated QSO systems within the magnitude limit of object B. This detection was indeed serendipitous.

We wish to thank the anonymous referee for the helpful comments that improved the quality of this work. The research leading to these results has received funding from the European Research Council under the European Union's Seventh Framework Program (FP7/2007-2013)/ERC Grant agreement No. EGGS-278202. The data presented here were obtained with ALFOSC, which is provided by the Instituto de Astrofisica de Andalucia (IAA) under a joint agreement with the University of Copenhagen and NOTSA. B.V. acknowledges funding through the ERC grant Cosmic Dawn. M.V. gratefully acknowledges support from the Danish Council for Independent Research via grant No. DFF 4002-00275. Funding for the Sloan Digital Sky Survey III has been provided by the Alfred P. Sloan Foundation, the U.S. Department of Energy Office of Science, and the Participating Institutions. SDSS-IV acknowledges support and resources from the Center for High-Performance Computing at the University of Utah. The SDSS website is www.sdss.org.

REFERENCES

Alam, S., Albareti, F. D., Allende Prieto, C., et al. 2015, ApJS, 219, 12
Croom, S. M., Smith, R. J., Boyle, B. J., et al. 2004, MNRAS, 349, 1397
Fynbo, J. P. U., Krogager, J.-K., Venemans, B., et al. 2013, ApJS, 204, 6
Hennawi, J. F., Prochaska, J. X., Burles, S., et al. 2006a, ApJ, 651, 61
Hennawi, J. F., Strauss, M. A., Oguri, M., et al. 2006b, AJ, 131, 1
Inada, N., Oguri, M., Shin, M.-S., et al. 2012, AJ, 143, 119
Komatsu, E., Smith, K. M., Dunkley, J., et al. 2011, ApJS, 192, 18
Krogager, J.-K., Geier, S., Fynbo, J. P. U., et al. 2015, ApJS, 217, 5
Lawrence, A., Warren, S. J., Almaini, O., et al. 2007, MNRAS, 379, 1599
Møller, P., & Kjaergaard, P. 1992, A&A, 258, 234
More, A., Oguri, M., Kayo, I., et al. 2016, MNRAS, 456, 1595
Mortlock, D. J., Webster, R. L., & Francis, P. J. 1999, MNRAS, 309, 836
Richards, G. T., Croom, S. M., Anderson, S. F., et al. 2005, MNRAS, 360, 839
Richards, G. T., Fan, X., Newberg, H. J., et al. 2002, AJ, 123, 2945
Schlegel, D. J., Finkbeiner, D. P., & Davis, M. 1998, ApJ, 500, 525
Stanishev, V. 2007, AN, 328, 948
van Dokkum, P. G. 2001, PASP, 113, 1420
Vestergaard, M., & Wilkes, B. J. 2001, ApJS, 134, 1
York, D. G., Adelman, J., Anderson, J. E., Jr., et al. 2000, AJ, 120, 1579

Appendix B

Determining the fraction of reddened quasars in COSMOS with multiple selection techniques from X-ray to radio wavelengths, accepted for publication in the journal Astronomy and Astrophysics. Authors: Heintz, K. E., Fynbo, J. P. U., Møller, P., Milvang-Jensen, B., Zabl, J., Maddox, N., Krogager, J.-K., Geier, S., Vestergaard, M., Noterdaeme, P. Ledoux, C.

The idea of this project came from Johan Fynbo. In the work I was the PI for the observing run on which we obtained spectroscopy of the four candidate quasars (but the actual observations was done by C. Grillo, D. Malesani and B. Milvang-Jensen). J. Zabl helped running one object through his SED fitting code, and N. Maddox ran the KX candidate through her custom-designed algorithm. I had great help from B. Milvang-Jensen with obtaining the data used in this work, but did the merging of catalogs and selection myself. P. Møller helped restructure the first draft of the paper to a form that is closer to the one presented in the paper. The other co-authors have contributed at the level of commenting on the text and figures and making suggestions for changes of these.

Astronomy & Astrophysics manuscript no. 28836_ap
August 25, 2016

Determining the fraction of reddened quasars in COSMOS with multiple selection techniques from X-ray to radio wavelengths⋆

K. E. Heintz[1], J. P. U. Fynbo[1], P. Møller[2], B. Milvang-Jensen[1], J. Zabl[1], N. Maddox[3], J.-K. Krogager[1,4], S. Geier[5,6], M. Vestergaard[1,7], P. Noterdaeme[4], C. Ledoux[8]

[1] Dark Cosmology Centre, Niels Bohr Institute, Copenhagen University, Juliane Maries Vej 30, 2100 Copenhagen Ø, Denmark
e-mail: heintz@dark-cosmology.dk
[2] European Southern Observatory, Karl-Schwarzschildstrasse 2, D-85748 Garching, Germany
[3] ASTRON, the Netherlands Institute for Radio Astronomy, Postbus 2, 7990 AA, Dwingeloo, The Netherlands
[4] Institut d'Astrophysique de Paris, CNRS-UPMC, UMR7095, 98bis bd Arago, 75014 Paris, France
[5] Gran Telescopio Canarias (GRANTECAN), Cuesta de San José s/n, E-38712 , Breña Baja, La Palma, Spain
[6] Instituto de Astrofísica de Canarias, Vía Láctea s/n, E38200, La Laguna, Tenerife, Spain
[7] Steward Observatory, University of Arizona, 933 N. Cherry Avenue, Tucson AZ 85721, USA
[8] European Southern Observatory, Alonso de Córdova 3107, Vitacura, Casilla 19001, Santiago 19, Chile

accepted for publication in *Astronomy & Astrophysics*, August 19, 2016

ABSTRACT

The sub-population of quasars reddened by intrinsic or intervening clouds of dust are known to be underrepresented in optical quasar surveys. By defining a complete parent sample of the brightest and spatially unresolved quasars in the COSMOS field, we quantify to which extent this sub-population is fundamental to our understanding of the true population of quasars. By using the available multiwavelength data of various surveys in the COSMOS field, we built a parent sample of 33 quasars brighter than $J = 20$ mag, identified by reliable X-ray to radio wavelength selection techniques. Spectroscopic follow-up with the NOT/ALFOSC was carried out for four candidate quasars that had not been targeted previously to obtain a 100% redshift completeness of the sample. The population of high A_V quasars (HAQs), a specific sub-population of quasars selected from optical/near-infrared photometry, some of which were shown to be missed in large optical surveys such as SDSS, is found to contribute $21\%^{+9}_{-5}$ of the parent sample. The full population of bright spatially unresolved quasars represented by our parent sample consists of $39\%^{+9}_{-8}$ reddened quasars defined by having $A_V > 0.1$, and $21\%^{+9}_{-5}$ of the sample having $E(B-V) > 0.1$ assuming the extinction curve of the Small Magellanic Cloud. We show that the HAQ selection works well for selecting reddened quasars, but some are missed because their optical spectra are too blue to pass the $g-r$ color cut in the HAQ selection. This is either due to a low degree of dust reddening or anomalous spectra. We find that the fraction of quasars with contributing light from the host galaxy, causing observed extended spatial morphology, is most dominant at $z \lesssim 1$. At higher redshifts the population of spatially unresolved quasars selected by our parent sample is found to be representative of the full population of bright active galactic nuclei at $J < 20$ mag. This work quantifies the bias against reddened quasars in studies that are based solely on optical surveys.

Key words. quasars: general – galaxies: active – surveys – dust, extinction

1. Introduction

The nature of quasars and their cosmological applications are of central importance in contemporary astrophysics. To properly understand the origin and physical nature of quasars in a general context, great caution has to be applied when defining the techniques with which these objects are selected and samples are built. For many applications the assembly of large samples of quasars has to be representative of the general population since selection bias will give a distorted picture of the full underlying population. Most large-area quasar surveys have relied on optical photometric selection, for instance, the Sloan Digital Sky Survey (SDSS; York et al. 2000; Richards et al. 2002) and the 2dF quasar redshift survey (2QZ; Croom et al. 2004). However, they have been found to be systematically biased against intrinsically dust-reddened quasars (e.g., Richards et al. 2003; Krawczyk et al. 2015) and intervening dust-rich absorbers reddening the background quasar (Noterdaeme et al. 2009, 2010, 2012; Kaplan et al. 2010; Fynbo et al. 2011; Wang et al. 2012; Krogager et al. 2016). Moreover, optical surveys contain other biases, for example, against quasars above redshifts of $z > 2.5$, at which point the Lyman-α (Lyα) forest (LyαF) enters the optical u-band, effectively removing the observed UV excess (UVX) of quasars compared to that of stars (Fan 1999).

It it therefore important to understand to what extent various quasar samples suffer from biases against dust-reddened systems and quasars at high redshifts so that we can build more complete and representative samples. A large number of studies targeting reddened quasars have been executed in the past two decades (see, e.g., Webster et al. 1995; Warren et al. 2000; Gregg et al. 2002; Richards et al. 2003; Hopkins et al. 2004; Glikman et al. 2007, 2012, 2013; Maddox et al. 2008, 2012; Urrutia et al. 2009; Banerji et al. 2012; Fynbo et al. 2013; Krogager et al. 2015), all trying to probe this underrepresented subset of quasars using a

⋆ Partly based on observations made with the Nordic Optical Telescope, operated by the Nordic Optical Telescope Scientific Association at the Observatorio del Roque de los Muchachos, La Palma, Spain, of the Instituto de Astrofisica de Canarias.

range of selection techniques that are less sensitive to dust obscuration. With the advent of large-area near- and mid-infrared surveys such as UKIDSS, *WISE,* and *Spitzer* (Wright et al. 2010; Cutri & et al. 2013; Lawrence et al. 2007; Warren et al. 2007; Werner et al. 2004; Fazio et al. 2004), the selection of quasars based on infrared (IR) photometry alone has been made possible as well (Donley et al. 2008, 2012; Peth et al. 2011; Stern et al. 2012; Mateos et al. 2012; Secrest et al. 2015). Quasars identified by their mid-infrared colors can be selected without requiring X-ray or radio detections and blue optical colors. In addition, other types of selection techniques have recently been proposed that are unbiased in terms of colors (Schmidt et al. 2010; Graham et al. 2014; Heintz et al. 2015), to independently probe the full underlying population of quasars.

How large the missing population of dust-reddened quasars is compared to the full population is still debated. Recent studies estimate fractions from below 10% to above 40% (Richards et al. 2003, 2006; Glikman et al. 2004, 2012; Gibson et al. 2009; Urrutia et al. 2009; Allen et al. 2011; Maddox et al. 2008, 2012). The majority of objects in these samples consist of broad absorption line (BAL) quasars. The search for quasars reddened by intervening absorbers, dubbed the high A_V quasar (HAQ; Fynbo et al. 2013; Krogager et al. 2015) survey, reveals that a large portion of intrinsically reddened quasars are missing in optical samples as well.

In this paper we examine the fraction of the HAQs and in general the dust-reddened population of quasars (which we define as having $A_V > 0.1$) compared to the total. The aim is to determine whether this missing sub-population constitutes a significant fraction of the true population of quasars and if the reddest of the most bright and spatially unresolved quasars are indeed identified by the tailored optical and near-infrared (NIR) color criteria used in the HAQ survey. We have decided to focus on spatially unresolved sources because the selection of point sources is a central part of the HAQ survey. In the same vein, we focused on relatively bright quasars, $J < 20$ mag because we are interested in the population of intrinsically bright quasars that are typically used for quasar absorption lines studies, for example. To securely determine the fraction, an effective selection of the complete population of quasars within the appropriate limit in brightness has to be obtained. We assume that this can be done using multiple selection techniques covering the different observed features of quasars.

The paper is structured as follows. In Sect. 2 we briefly describe the different data sets obtained from the COSMOS surveys and how these were combined to apply all the multiwavelength information to each object within our defined region of the COSMOS field. In Sect. 3 we define the quasar selection techniques used to build our parent sample, representing the full population of the brightest spatially unresolved quasars. In Sect. 4 we describe our follow-up observations, and in Sect. 5 we present the results. In Sect. 6 we discuss our analysis, and in Sect. 7 we conclude on the implication of our work in a general context. We assume a standard flat ΛCDM cosmology with $H_0 = 70$ km s^{-1} Mpc^{-1}, $\Omega_M = 0.3$ and $\Omega_\Lambda = 0.7$. Unless otherwise stated, the AB magnitude system (Oke 1974) is used throughout this paper.

2. Data description

By using the extensive multiwavelength data sets available from the combined COSMOS (Scoville et al. 2007b) surveys, all covering the *Chandra* COSMOS (C-COSMOS; Elvis et al. 2009; Civano et al. 2012) field, the different methods for quasar selection (see Sect. 3.2-3.7) can be applied. This sub-field of COSMOS covers the central 0.9 deg^2 of the approximately two square degrees of the COSMOS field (see, e.g., Fig. 1 in Elvis et al. (2009) and Fig. 1 in McCracken et al. (2012) for the specific outline of the field). This region is one of the most observed fields on the sky, making it excellent for detailed studies of general quasar properties and populations, and it is therefore ideal for our study. By building a parent sample consisting of the quasars selected with a range of different methods, the fraction of the HAQs compared to the full underlying population, that is, the extent to which the HAQs contribute to the defined parent sample of quasars, can be determined. Although extensive spectroscopic analysis is available in this field, a minority of the candidate quasars from the parent sample were without existing spectra, so that follow-up spectroscopy was required to confirm their nature for the purpose of this study.

2.1. COSMOS field: from X-ray to radio wavelengths

The COSMOS field was originally defined by Scoville et al. (2007b) as a two deg^2 region with multiwavelength coverage, including HST/ACS F814W imaging over 1.8 deg^2 (Scoville et al. 2007a). It was observed using the Advanced Camera for Surveys (ACS) Wide Field Channel (WFC) and imaged in the F814W filter which is broad I-band filter centered on an effective wavelength of 7940Åwith a resolution of $\sim 0\farcs1$. For a description, see for example Koekemoer et al. (2007) for how the HST-ACS mosaic was produced and Leauthaud et al. (2007) for how the mosaic was used to assemble a source catalog. This catalog consists of approximately 1.2×10^6 objects down to a limiting magnitude of $F814W = 26.6$ mag.

In our study we used the X-ray information from the initial *Chandra* COSMOS (C-COSMOS; Elvis et al. 2009; Civano et al. 2012) and the XMM-COSMOS surveys (Hasinger et al. 2007; Cappelluti et al. 2009; Brusa et al. 2010). C-COSMOS, an extensive 1.8 Ms *Chandra* program, has imaged the central 0.9 deg^2 of the COSMOS field down to the limiting fluxes of 1.9×10^{-16} erg cm^{-2} s^{-1} in the soft (0.5 - 2 keV) band, 7.3×10^{-16} erg cm^{-2} s^{-1} in the hard (2 - 10 keV) band and 5.7×10^{-16} erg cm^{-2} s^{-1} in the full (0.5 - 10 keV) band (Elvis et al. 2009). Complementary to *Chandra* are the X-ray data from the XMM-COSMOS mission, which is a contiguous 2 deg^2 *XMM-Newton* survey of the COSMOS field. The limiting fluxes are 5×10^{-16}, 3×10^{-15} and 7×10^{-17} erg cm^{-2} s^{-1} in the $0.5-2$, $2-10$ and $5-10$ keV bands, respectively (Hasinger et al. 2007). The flux limits of the two surveys are not reached over the complete area but vary across the field because of irregular exposure times. The sensitivity of C-COSMOS due to its sub-arcsecond imaging is three times below the corresponding flux limits for the XMM-COSMOS survey.

The initial C-COSMOS survey used in this paper consists of 1761 X-ray detected point sources, where the XMM-COSMOS survey have observed 1797 X-ray point sources. Elvis et al. (2009) reported that 70 sources from the XMM-COSMOS catalog were absent from the C-COSMOS sample, while 24 XMM-COSMOS sources have been resolved into two distinct sources in the C-COSMOS catalog. The optical/near-infrared COSMOS counterparts were found for each of the X-ray point source detections with *Chandra* and *XMM-Newton* (see Civano et al. 2012; Brusa et al. 2010, respectively). Based on these counterparts, the photometric redshifts of each of the sources have been determined by Salvato et al. (2009, 2011).

In addition to the two X-ray surveys, we used the photometric data from the multiband catalog described in Ilbert et al.

(2013). This catalog consists of multiband photometry covering the near-ultraviolet (NUV) to the mid-infrared (MIR) effective wavelengths. The NUV-optical data sets are from previous releases, described in Capak et al. (2007); Ilbert et al. (2009). The catalog by Capak et al. (2007) also contains optical photometry in the u, g, r, i, z bands from the SDSS data release 2 (DR2; Abazajian et al. 2004), produced by facilitating photometric measurements from a mosaic of the SDSS placed on the same grid as the other COSMOS data. We used the star/galaxy classifier from the Capak et al. (2007) catalog, which allowed us to only target optical point sources (spatially unresolved quasars). At wavelengths redward of the UltraVISTA ($\sim 1-2\,\mu$m) coverage, we used the MIR data from the *Wide-field Infrared Survey Explorer* (*WISE*; Wright et al. 2010) most recent data release (AllWISE; Cutri & et al. 2013). This all-sky mission has imaged the sky in four different MIR filters with effective wavelengths ranging from 3.4 μm to 22 μm. Finally, we included the radio ($\sim$ 21 cm) data from the deep and joint VLA-COSMOS catalog (Schinnerer et al. 2007, 2010). Detailed imaging from the various COSMOS surveys is publicly available at the NASA/IPAC Infrared Science Archive (IRSA) web page[1].

2.2. Matching procedure

We required that each of the sources from the various COSMOS data sets are within 2 arcsec from the objects listed in the photometric catalog by Ilbert et al. (2013, hereafter I13). Since multiple objects can be within this region, we selected only the nearest match. For the *Chandra/XMM-Newton* detected X-ray point sources, we matched the optical/NIR counterparts found by Civano et al. (2012); Brusa et al. (2010), respectively, to the photometric catalog by I13. In the first COSMOS optical/NIR catalog by Capak et al. (2007), the morphology information from the CFHT+Subaru *i*-band images was included. Therefore only this catalog had to be matched to the photometric catalog by I13, again within 2 arcsec. This was done primarily to attach the morphological data to the UltraVISTA DR1 sources, but also to obtain the SDSS five-band magnitudes for each of the objects. Following the same procedure, we paired the objects detected in the AllWISE and VLA-COSMOS data sets to the optical/NIR counterparts in the photometric catalog (I13) as well.

3. Selection techniques

Since the publicly available C-COSMOS survey is limited to the central 0.9 deg^2 of the COSMOS field, see for instance Fig. 1 of Elvis et al. (2009), we isolated this region from the rest of the data sets. In Fig. 1 the confirmed and the candidate quasars (specifics of the subsample symbols are defined below) within this specific region is shown, where the gray dashed lines represent the coverage of the C-COSMOS survey, indicating our targeted region of the COSMOS field. Applying these boundaries furthermore ensures that the whole sub-field examined is covered by all the multiwavelength surveys.

3.1. Morphology and brightness

In the original HAQ criteria (and most other optical/NIR color selection approaches) the targeted objects were defined as optical and NIR point sources. In this study we follow the same procedure and select spatially unresolved sources at observed optical wavelengths only (using the star/galaxy classifier of Capak et al. (2007), based on ground-based photometry from the CFHT+Subaru *i*-band images), while discarding the sources with dominating light from the host galaxy. This means that we only considered the optically unresolved quasar population and not the overall/general active galactic nucleus (AGN) population. We discuss the implication of this specific morphology cut in detail in Sect. 6. Moreover, we also defined an upper magnitude limit of $J_{\rm AB} < 20$ mag to avoid being biased against the depth of each of the individual surveys. This magnitude limit furthermore ensures a fair comparison of each of the respective quasar populations within a certain brightness. This provides a more secure detection and low errors on the photometric data. In the following sections we describe how each of the specific quasar selection techniques were applied. We only considered the optically unresolved sources that were brighter than our magnitude limit before the distinctive selection techniques.

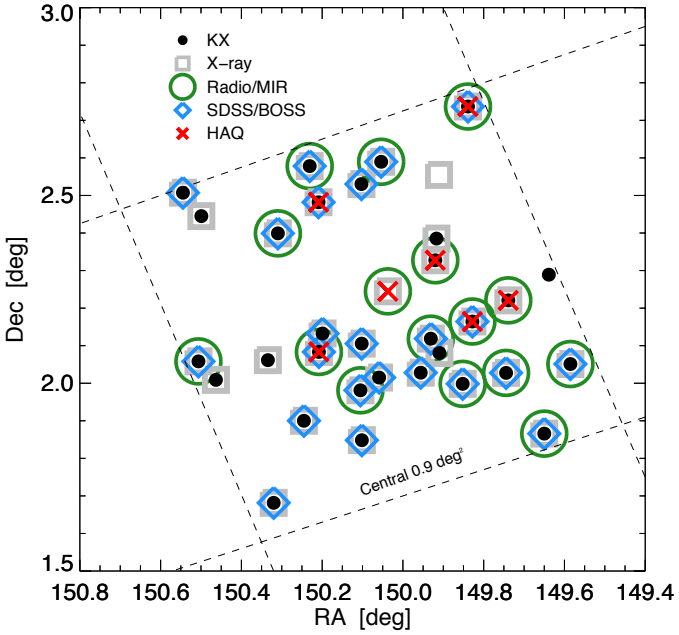

Fig. 1: Location of the 34 confirmed and candidate quasars from the parent sample. Overplotted are the cuts in right ascension (RA) and declination (Dec) used to isolate the C-COSMOS field. The symbols represent individual selection methods used to identify each candidate quasar (see Sect. 3.2-3.7).

3.2. HAQ selection

This tailored search for reddened quasars was originally designed to search for dust-rich damped Lyα absorbers (DLAs) along the line of sight toward the background source. Dust-rich DLAs are known to redden the background source to the extent where optical color selection fails to classify them as quasars (Noterdaeme et al. 2009, 2010, 2012; Fynbo et al. 2011; Kaplan et al. 2010; Krogager et al. 2016). To select HAQ candidates from the COSMOS photometric catalog by I13, we adopted the same criteria as in Krogager et al. (2015), all on the AB magnitude system:

$$J - K_s > 0, \quad H - K_s > 0, \quad J - H < 0.4,$$
$$0.5 < g - r < 1.0, \quad 0.1 < r - i < 0.7 \ . \qquad (1)$$

[1] http://irsa.ipac.caltech.edu/data/COSMOS/index_cutouts.html

These criteria were defined based on the pilot study executed before the HAQ survey, described in Fynbo et al. (2013). They were found to identify quasars (not necessarily all having high A_V, as the name suggests) with a purity of $P \sim 97\%$ (154/159) from the set of candidates selected from optical/NIR photometry, where the remaining objects were two dwarf stars and three so-far unidentified objects. While only a handful of DLAs were found, numerous intrinsically reddened quasars were detected with a pronounced amount of extinction from dust, quantified by the parameter A_V. Only ∼45% of the HAQ candidates from the original study were spectroscopically classified as quasars in DR7 before observation. A small fraction of the spectroscopically verified HAQs were later observed by the SDSS-III/BOSS (DR10Q; Pâris et al. 2014) program, which relies on more advanced selection algorithms than the original optical color criteria of SDSS-I/II (see, e.g., Ross et al. 2012; Dawson et al. 2013, and Sect. 3.7). To distinguish the HAQ selected quasars from the general population of reddened quasars, we use the term HAQs for the quasars that were selected by the same (and very limiting) optical/NIR criteria of Krogager et al. (2015). We found that seven objects satisfy the HAQ criteria. The HAQ selected candidate quasars are marked with an "H" in Col. 3 in Table 1 and with red crosses in Fig. 1. Owing to different redshifts, intrinsic slopes, and other absorption features, not all quasars selected in this way do in fact have high A_V, but we adopted the original name for consistency. The quasars with $A_V > 0.1$ are referred to as red quasars or the general reddened population of quasars. Defining this lower limit ensures that quasars with natural variability (typically ±0.05 mag, as inferred from Krogager et al. 2015) are not considered as part of the reddened population of quasars.

3.3. KX selection

Another approach to identify the missing reddened quasars, regardless of redshift and amount of dust reddening, is to exploit the general K-band excess (KX) shown by all quasars (Warren et al. 2000; Croom et al. 2001; Maddox et al. 2008, 2012) hereafter referred to as KX. This approach is comparable to the HAQ selection criteria with the NIR K-band excess of quasars being the primary quasar/star classifier, although not as tailored for targeting objects with red optical colors. This selection was therefore not as specialized in selecting quasars with intervening DLAs as the HAQ survey, but is unbiased toward those objects in the same way, and will therefore be more complete in detecting quasars. The KX selected candidate quasars were selected from the COSMOS photometric catalog by I13 as well, where we converted the original selection criteria from Vega to AB magnitudes. We refined the magnitude range used in their study of $14.0 < K_{Vega} < 16.6$ to $K_{s,AB} > 15.85$, $J_{AB} \leq 20$ mag. Here, the lower limit was converted from Vega into AB magnitudes (following the formulation of Blanton & Roweis 2007), and the upper limit is $\sim 0.5 - 1$ magnitude fainter than the original to match our overall magnitude limit. The refined criteria, that is, the selection lines, are then as follows, again all on the AB magnitude system:

$$g-J < \begin{cases} 4.4(J-K_s) - 2.08, & \text{for } J-K_s \leq -0.04,\ g-J \leq 2.01 \\ 20.83(J-K_s) - 2.83, & \text{for } J-K_s \geq -0.04,\ g-J \geq 2.01 \end{cases} \quad (2)$$

These can be directly compared to the selection criteria and the selection lines in Fig. 2 of Maddox et al. (2008, 2012). Following the original KX selection procedure, we proceeded to run the candidate quasars without existing spectra, detected by their K-band excess, through the custom-made photo-z algorithm described in Maddox et al. (2008, 2012). This algorithm is based on a standard model quasar template with seven reddened models created from the base model with increasing amounts of Small Magellanic Cloud (SMC)-type dust. To exclude compact galaxies, seven galaxy templates spanning E through Scd types were included. Star templates were also incorporated obtained from the Bruzual–Persson–Gunn–Stryker atlas[2]. By first applying the gJK color cut, about 95% of the objects were removed in the original sample. Then, by applying the photo-z code to the remaining objects, most of the contaminants were excluded, with colors inconsistent with standard quasars. After the photometric data of the candidates with no pre-existing spectra were processed by the photo-z code, the sample of KX selected candidate quasars consisted of 31 objects. The KX selected candidate quasars are marked with a K in Col. 3 in Table 1 and with black dots in Fig. 1.

3.4. X-ray detection

Selection at X-ray wavelengths has been found to effectively identify quasars, or AGNs in general (Brandt & Hasinger 2005), with an insignificant amount of contamination from star-forming galaxies, which are otherwise present in optical or infrared surveys (Donley et al. 2008, 2012). Stars with strong X-ray emission can also appear in X-ray samples, but because of their distinct stellar colors, they can easily be rejected as non-quasar candidates. Moreover, X-ray surveys are efficient in detecting low-luminosity and obscured quasars below the *Compton-thick* limit. To select quasars detected by *Chandra/XMM-Newton,* we required that the optical/NIR counterparts of the X-ray point sources were unresolved in the CFHT+Subaru i-band images. The flux limits of the two X-ray surveys and the matching to the optical/NIR counterpart to apply the morphological information are described in Sects. 2.1 and 2.2, respectively.

A significant amount of the selected objects were stars with strong X-ray emission. We discarded the X-ray point sources determined to be Galactic stellar sources by Salvato et al. (2009, 2011), based on either spectroscopically confirmed spectra or photometrically computed stellar fits by their χ^2 analysis. No requirements were imposed on the optical/IR photometry, except for the general defined magnitude limit. In Sect. 6 we discuss in more detail the morphological context of the objects that are point sources at X-ray wavelengths but not in the optical, or in other words, the general AGN X-ray population. We found 32 objects detected with *Chandra/XMM-Newton* all having a spatially unresolved optical/NIR counterpart in the photometric catalog by I13. The X-ray selected candidate quasars are marked with an X in Col. 3 in Table 1 and with gray squares in Fig. 1.

3.5. Radio detection

Apparent optical stellar sources with extreme radio emission represent the first detected subpopulation of radio-loud quasars (Schmidt 1963; Matthews & Sandage 1963). This selection is not affected by extinction at optical wavelengths and would therefore not be biased against dust-reddened quasars, see, for instance, Becker et al. (1997). By definition, only the radio-loud quasars will be targeted by this approach, so that the sample in itself is not complete (see, e.g., Urry & Padovani 1995; Sikora et al. 2007, for a description of the radio emission from quasars

[2] http://www.stsci.edu/hst/observatory/cdbs/bpgs.html

and the empirical observations of the two sub-populations, respectively). Two recent radio selections of optical spatially unresolved quasars (Ivezić et al. 2002; Baloković et al. 2012) used data from the Faint Images of the Radio Sky at Twenty centimeters (FIRST; Becker et al. 1995) mission together with the SDSS program. A similar approach was executed based on source detection with the FIRST matched to the NIR counterparts of the Two Micron All Sky Survey (2MASS; Skrutskie et al. 2006) by Glikman et al. (2007, 2012); Urrutia et al. (2009). Equivalent to these, we selected candidate quasars detected by VLA by only requiring that the optical/NIR counterpart of the radio-detected sources were unresolved in the CFHT+Subaru *i*-band images. No further constraints were set on the VLA data, and we found that nine sources were selected in this way. The radio-selected candidate quasars are marked with an R in Col. 3 in Table 1 and with green circles in Fig. 1.

3.6. Mid-infrared selection

Recently, with the launch of the complementary MIR *Spitzer* and *WISE* missions, multiple new approaches of selecting quasars using MIR colors alone have been developed. See, for example, the *Spitzer* two-color criteria of Donley et al. (2012), the *WISE* one-color criteria of Stern et al. (2012); Assef et al. (2013), and the *WISE* two-color criteria of Mateos et al. (2012). All these criteria were defined by the unique colors of quasars in MIR color space, primarily tracing the torus around the super-massive black hole (SMBH) of the AGN. A selection based on the MIR wavelength range is insensitive to dust extinction and will therefore not be biased toward reddened quasars (Mateos et al. 2013; LaMassa et al. 2016). We chose the *WISE* two-color criteria of Mateos et al. (2012) as used by Secrest et al. (2015) to represent the MIR selected quasars. They defined the AGN locus in Vega magnitudes by

$$W1 - W2 = 0.315 \times (W2 - W3), \quad (3)$$

where the top and bottom boundaries of this two-color wedge are obtained by adding y-axis intercepts of +0.796 and -0.222, respectively (see Eqs. 3 and 4 of Mateos et al. 2012). This selection, compared to the other MIR selection approaches, was found to show less contamination from brown dwarfs and to be more complete. Following the same procedure as for the X-ray and radio-detected candidate quasars, we discarded objects that were selected by the MIR two-color criteria but were spatially resolved in the CFHT+Subaru *i*-band images. Again, the implication for this specific selection is discussed in Sect. 6. By using these criteria, we found ten sources selected by their MIR colors and spatially unresolved counterpart in I13. The MIR-selected candidate quasars are marked with an M in Col. 3 in Table 1 and with green circles in Fig. 1.

3.7. SDSS-III/BOSS DR12Q sample

The DR12Q sample is a combination of the pre-BOSS SDSS-I/II quasar selection program (see, e.g., Richards et al. 2002; Schneider et al. 2010, for the selection criteria and the full pre-BOSS sample, respectively), which focused on quasars with high UVX and objects with outlying optical colors compared to that of stars. The SDSS-III/BOSS program depended on numerous other more advanced selection algorithms (see Ross et al. 2012; Dawson et al. 2013, for a description of the selection algorithms and the spectroscopic survey of the SDSS-III/BOSS programme), specifically designed to target quasars at $z > 2.2$. We included all the confirmed quasars from the pre-BOSS (SDSS-I/II) and SDSS-III/BOSS DR12Q samples (Pâris et al. 2016, in prep.) within the central region of the COSMOS field with the same requirements of morphology and brightness from the COSMOS photometric catalog by I13. In Sect. 6 we directly show which of the SDSS/BOSS-selected quasars we discarded due to these cuts. Some of the spectroscopically verified quasars have been observed by the SDSS/BOSS programs only because they were detected in the *ROSAT, FIRST, Chandra,* or *XMM* missions. These were not included as SDSS- or BOSS-selected quasars in our sample, but with the corresponding X-ray or radio detection instead. This was done to examine the photometric selection of these two selection functions alone, since X-ray and radio selection is a part of our study by design. Notes on how each of the SDSS/BOSS quasars were selected are given in the appendix, Fig. 10. We found that 23 sources were selected based on their photometry by the SDSS/BOSS programs, where 15 quasars are from the SDSS and 8 quasars are from the BOSS survey. The SDSS/BOSS photometrically selected candidate quasars are marked with either an S or B for SDSS or BOSS selection, respectively, in Col. 3 in Table 1 and with blue diamonds in Fig. 1.

3.8. Parent sample

Combining the confirmed and the candidate quasars obtained from all six selection approaches, we found a total number of 34 objects brighter than $J = 20$ magnitude, all located in the C-COSMOS field. The majority of the quasars (30/34) have existing spectra in the literature (see, e.g., the SDSS DR12 database[3]), whereas the remaining four objects had to be verified spectroscopically (see next section). This is necessary to verify the computed photometric redshift and to calculate the extinction of each of the quasars by analyzing the amount of reddening from the slope of the spectral energy distribution (SED) and the photometric data points. In Table 1 all candidate and confirmed quasars are listed by name together with the respective techniques by which they were selected. The letters denoting each of the selection techniques, as shown in the table, are used in the following sections. The names are listed either as Q+coordinates for known quasars or CQ+coordinates for the candidate quasars.

4. Spectroscopic observations and analysis

4.1. Observations and data reduction

The observations of the four candidate quasars were carried out during an observing run with the Nordic Optical Telescope (NOT) on La Palma on February 12–15, 2016. The spectra were obtained using the Andalucia Faint Object Spectrograph and Camera (ALFOSC). In Table 2 the setup for the spectroscopic follow-up of these four candidate quasars is summarized. Grism 4 covers the wavelengths 3200 − 9100 Å with a spectral resolution of ∼300, whereas grism 18 is limited to the blue part of the spectrum covering the wavelengths of 3530 − 5200 Å. This was only used for CQ095924.4+020842.6 since it appeared to have few to no emission features in the spectrum obtained with grism 4. Blocking filter 94 was used in combination with grism 4 to eliminate second-order contamination from wavelengths shorter than 3560 Å. The spectra were taken by aligning the slit at parallactic angle.

[3] http://skyserver.sdss.org/dr12/en/home.aspx

Table 1: Number, object name, selection technique(s), $z_{\rm spec}$, $z_{\rm phot}$, A_V, brightness in J-band, and additional notes for each of the confirmed quasars in the parent sample. Following the notation in Sect. 3.2 – 3.7 for the selection techniques; K = KX selection, X = X-ray detection, R = radio detection, M = MIR selection, S/B = SDSS/BOSS photometric selection, and H = HAQ selection.

#	Object	Selection	$z_{\rm spec}$	$z_{\rm phot}$	A_V (SMC)	A_V (Zafar+15)	J-band (mag)	Notes
(1)	(2)	(3)	(4)	(5)	(6)	(7)	(8)	(9)
1	Q 095820.5+020304.1	KXMS	1.356	1.462	0.00	0.00	19.70	*g-r, r-i*
2	CQ 095833.3+021720.4	K	1.910	1.750	0.23	0.23	19.99	*g-r*
3	Q 095836.0+015157.1	KXRB	2.935	2.919	0.00	0.00	19.32	*g-r*
4	Q 095857.4+021314.5	KXRH	1.024	1.043	0.38	0.30	19.41	
5	Q 095858.7+020139.1	KXMB	2.448	2.418	0.00	0.00	18.70	*g-r, r-i*
6	Q 095918.7+020951.7	KXRMSH	1.156	1.181	0.30	0.15	19.72	
7	Q 095921.3+024412.4	KXRBH	1.004	0.030	0.98	0.60	19.37	
8	CQ 095924.4+020842.6	K	—	1.150	—	—	19.43	*g-r*, blended SED, non-quasar
9	Q 095924.5+015954.3	KXMS	1.241	1.281	0.00	0.00	18.49	*g-r, r-i*
10	Q 095938.3+020450.1	KX	2.802	2.779	0.23	0.08	19.74	*H-K$_s$*
11	CQ 095938.6+023316.7	X	0.740	0.742	1.21	0.68	19.47	*g-r*
12	Q 095940.1+022306.7	KX	1.131	1.110	0.15	0.15	19.93	*g-r, r-i*
13	Q 095940.8+021938.7	KXRH	1.454	1.465	0.30	0.30	19.74	
14	Q 095943.4+020707.4	KXRB	2.194	2.306	0.00	0.00	19.45	*g-r, r-i*
15	Q 095949.4+020141.0	KXS	1.753	1.753	0.00	0.00	18.99	*g-r*
16	CQ 100008.9+021440.7	XRMH	2.680	2.663	0.15	0.15	18.96	
17	Q 100012.9+023522.8	KXMS	0.698	0.702	0.00	0.08	18.47	*g-r*
18	Q 100014.1+020054.5	KXS	2.498	2.469	0.00	0.00	19.45	*g-r, r-i*
19	Q 100024.4+015054.0	KXS	1.661	1.669	0.30	0.30	19.61	*g-r, H-K$_s$*
20	Q 100024.5+020619.8	KXB	2.288	2.287	0.00	0.00	19.51	*g-r, r-i*
21	Q 100024.6+023149.1	KXS	1.319	1.362	0.00	0.00	19.36	*g-r, r-i, H-K$_s$*
22	Q 100025.3+015852.1	KXMS	0.372	0.372	0.00	0.00	19.07	*g-r*
23	Q 100047.8+020756.8	KXB	2.159	2.177	0.00	0.00	19.67	*g-r, r-i*
24	Q 100049.9+020500.0	KXRMBH	1.236	1.272	0.30	0.30	19.04	
25	Q 100050.1+022854.8	KXBH	3.365	3.378	0.00	0.00	19.64	
26	Q 100055.4+023441.4	KXRS	1.402	1.414	0.08	0.08	19.74	*g-r, r-i*
27	Q 100058.8+015400.3	KXS	1.560	1.557	0.00	0.00	19.87	*g-r, r-i*
28	Q 100114.3+022356.7	KXMS	1.802	1.777	0.00	0.00	19.38	*g-r*
29	Q 100116.8+014053.6	KXS	2.055	2.050	0.00	0.00	19.76	*g-r*
30	Q 100120.3+020341.2	KX	0.903	0.906	0.00	0.00	19.77	*g-r, r-i*
31	Q 100151.1+020032.5	KX	0.967	1.000	0.23	0.11	19.79	*g-r, r-i*
32	Q 100159.8+022641.7	KX	2.030	2.011	0.00	0.00	19.27	*g-r*
33	Q 100201.5+020329.4	KXMS	2.016	1.880	0.23	0.23	18.30	*g-r*
34	Q 100210.7+023026.2	KXS	1.160	1.340	0.00	0.00	19.17	*g-r, r-i*, XMM-COSMOS source

The spectra were processed using a combination of IRAF[4] and MIDAS[5] tasks for low-resolution spectroscopy. To reject cosmic rays, we used the LA-Cosmic software[6] developed by van Dokkum (2001). The flux calibration was done using a spectrophotometric standard star observed on the same night as the science spectra. We corrected the spectra for Galactic extinction using the extinction maps of Schlegel et al. (1998). To improve the absolute flux calibration, we scaled the spectra to be consistent with the *r*-band photometry from SDSS.

[4] IRAF is the Image Reduction and Analysis Facility, a general purpose software system for the reduction and analysis of astronomical data. IRAF is written and supported by the National Optical Astronomy Observatories (NOAO) in Tucson, Arizona. NOAO is operated by the Association of Universities for Research in Astronomy (AURA), Inc. under cooperative agreement with the National Science Foundation

[5] ESO-MIDAS is a copyright protected software product of the European Southern Observatory. The software is available under the GNU General Public License.

[6] Cosmic-Ray Rejection by Laplacian Edge Detection

4.2. Spectroscopic analysis

In Fig. 2 we show the one-dimensional spectra of the four candidate quasars along with the photometry from SDSS and UltraVISTA and the contours of the belonging images in four different wavelength bands: The optical F814W (I-band) filter from the HST-ACS mosaic, the near-infrared K_s filter from the KPNO mosaic, the X-ray *Chandra* merged energy band image, and the radio contours as observed by the VLA. We show the K_s imaging from KPNO since this (and not the UltraVISTA imaging) is available at the NASA/IPAC-IRSA web page. Overplotted is a composite quasar template by Selsing et al. (2016) with and without reddening (solid red and dashed blue lines, respectively). The composite was constructed from luminous blue quasars at $1 < z < 2.1$ selected from SDSS and has a slightly steeper spectral slope than other existing templates ($\alpha_\lambda = 1.70 \pm 0.01$ assuming a power-law continuum). This is explained for instance by the broader spectral wavelength coverage because the slope can more easily be determined without strong contamination quasar emission lines or by intrinsic host galaxy emission (see Selsing et al. 2016, for further details). The template was matched to

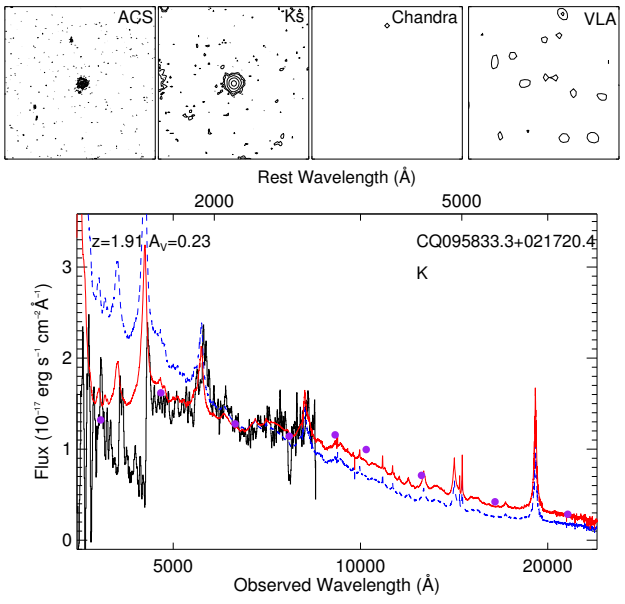

CQ: 2

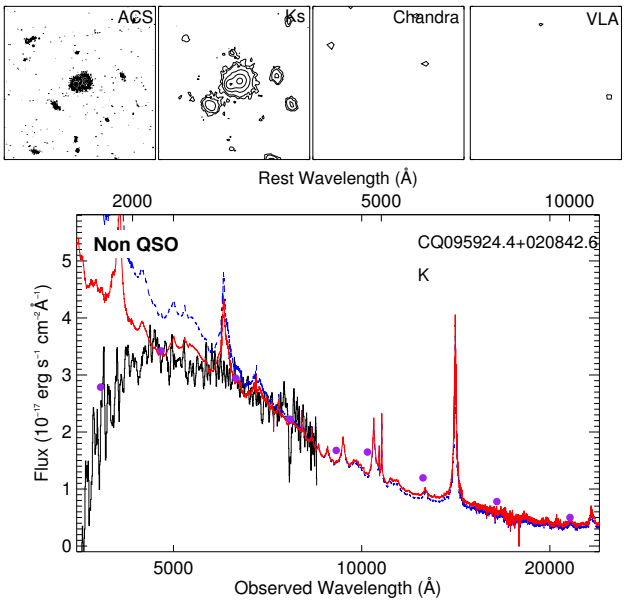

CQ: 8

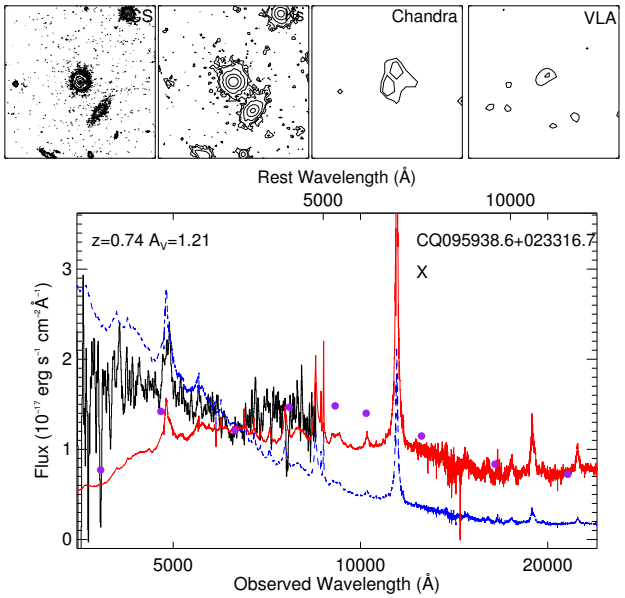

CQ: 11

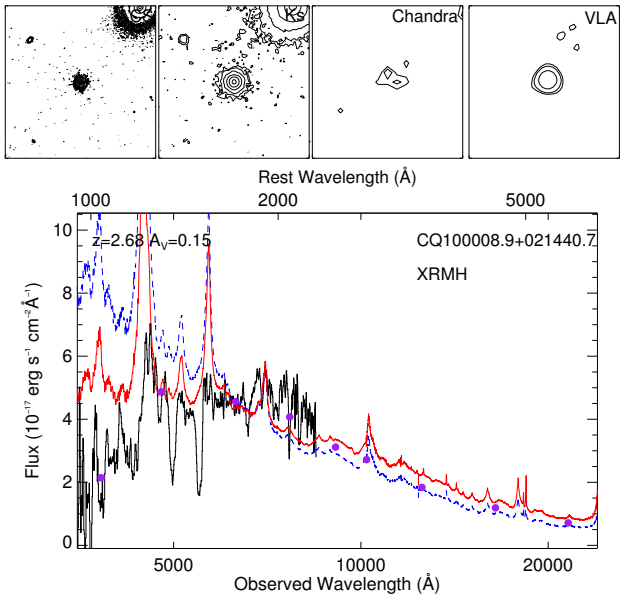

CQ: 16

Fig. 2: Extracted 1D spectra and images in four wavelength bands of the four candidate quasars observed for the purpose of this study. The three objects CQ095833.3+021720.4, CQ095938.6+023316.7, and CQ100008.9+021440.7 are confirmed to be quasars, whereas object CQ095924.4+020842.6 is not. The three confirmed quasars all show a pronounced amount of reddening and BAL features. *Upper panels:* Images of the objects shown in the optical F814W (I-band) filter from the HST-ACS mosaic, the near-infrared K_s filter from the KPNO mosaic, the X-ray *Chandra* merged energy band image, and the radio emission as seen by the VLA. Each of the images are 15×15 arcsec where north is up and east is to the left. *Bottom panels:* The solid black lines show the observed spectra from the NOT. Overplotted are the photometric data points shown by the purple dots from the merged optical/near-infrared photometric COSMOS catalog together with the composite quasar template spectrum from Selsing et al. (2016) with (red solid line) and without (blue dashed line) reddening, respectively. The redshift and amount of reddening, A_V, for each of the objects are shown in the upper left corner, while the name and selection method (from Col. 3 in Table 1) by which they were identified are shown in the upper right corner.

the visible emission lines to compute the spectroscopic redshifts. The template was constructed by combining spectra of luminous blue quasars at $1 < z < 2.1$ selected from the SDSS. The spectra combined to make the composite were observed with the X-shooter instrument at ESO/VLT, which allows for a simultaneous observation of the entire spectral range from the U to the K band. Hence, the observed effect of variability in quasars is not a problem in this composite. For the object CQ095924.4+020842.6 the

Table 2: Setup for the spectroscopic follow-up of the remaining four candidate quasars. Blocking filter 94 was used in combination with grism 4 for all observations.

Object	Grism	Slit width (arcsec)	Exp. time (sec)
CQ095833.3+021720.4	#4	1.3	3×1200
CQ095924.4+020842.6	#4 + #18	1.3/1.0	6×900
CQ095938.6+023316.7	#4	1.0	3×1200
CQ100008.9+021440.7	#4	1.3	3×600

composite is overplotted at the photometrically computed redshift ($z_{\rm phot} = 1.15$) since no emission line features are unambiguously present in the spectrum.

The amount of reddening for each of the objects was calculated assuming both an SMC-like extinction curve and a steeper extinction curve for intrinsically reddened quasars (Zafar et al. 2015). For the SMC we used the extinction curve as described by Gordon et al. (2003), but with a modification for wavelengths greater than 4400 Å (Fitzpatrick & Massa 2005), following the same procedure as in Urrutia et al. (2009); Fynbo et al. (2013). The extinction curve computed by Zafar et al. (2015) was determined from 16 reddened quasars from the original HAQ survey, where the SMC could not provide a good solution to the observed spectral SEDs. We found that for most of the dust-reddened quasars the Zafar+15 extinction curve template computes a lower value of A_V than when assuming SMC-like extinction (see Table 1). However, none of the two extinction curve templates were preferred over the other, meaning that both of the templates were in general good matches to the observed spectra. In the following we therefore consider only the A_V assuming SMC-like extinction.

The redshifts and the extinction was determined by visually matching the composite quasar template to the photometric data points and the observed spectra. For simplicity we assumed that the dust is located at the redshift of the quasar. The objects that do not show signs of reddening agree well with the unreddened composite quasar template. The reddened quasars can be identified by the discrepancy in the unreddened template to the observed spectra where the extinction parameter is simply a measurement of the amount of divergence. We disregarded photometric data blueward of the Lyα emission line, and in case of strong absorption at individual data points, these were excluded as well. The photometric data points are shown as the purple dots at the $u, g, r, i, z, Y, J, H, K_s$ effective wavelengths. The redshifts and amounts of reddening are shown for each of the objects, together with the object name, coordinates, and the respective selection technique by which the object was detected. In the Appendix, Fig. 10, the spectra of the remaining quasars are shown together with the corresponding images of each of the individual objects. Their extinction was determined following the same procedure as described above. Below each of the objects the SDSS/BOSS selection flags are stated.

We were able to obtain a secure confirmation of three objects: CQ095833.3+021720.4, CQ095938.6+023316.7, and CQ100008.9+021440.7. The visible emission lines in the three spectra allow for a clear redshift determination and agreed well with the computed photometric redshift. Two of the objects, CQ095833.3+021720.4 and CQ100008.9+021440.7, show clear broad absorption line (BAL) features. Quasar templates, both with and without reddening, show a poor fit to the spectrum of object CQ095924.4+020842.6. The photometry at MIR wavelengths disagrees with typical quasar MIR colors (Nikutta et al. 2014) as well. Because several stellar absorption lines at $z = 0.05$ are detected in the spectrum, we can identify a low-redshift quiescent galaxy as contribution to the SED. However, the full multiwavelength photometry cannot be fit well with BC03 stellar population synthesis models (Bruzual & Charlot 2003). The observed NIR and especially the MIR photometry shows excess compared to that expected from good model fits to the optical photometry. This most likely indicates that an additional source at higher redshift contributes to the observed SED, whose light would dominate at longer wavelengths. This scenario is supported by the HST imaging, which shows two close line-of-sight compact sources. For this object we do not list redshift or A_V in Fig. 2, but mark it as unclassified.

5. Results

We found 33 bright spatially unresolved quasars within the C-COSMOS sub-field brighter than $J = 20$ magnitude (corresponding to 37 quasars per square degree, see Sect. 3.8). We assume that our sample is a good representation of the full underlying population of quasars, although small (see below), since the bias should be negligible when using the multiple selection approaches, each of which target different aspects of quasar properties. In Fig. 3 a quantity diagram of the sub-populations of all the confirmed quasars is shown sorted according to the techniques through which they were selected and how they coincide. The numbering in the figure follows the same notation as in Table 1.

Out of the total number of quasars in the parent sample we found that seven optical point sources from the photometric catalog were selected by the specific optical/NIR HAQ criteria, see Eq. 1. This yields a fraction of $f_{\rm HAQ} = N_{\rm HAQ}/N_{\rm total} = 0.21^{+0.09}_{-0.05}$ ($21\%^{+9}_{-5}$) using the small number statistics formulated in Cameron (2011) with error bars corresponding to the 68% confidence interval, see Fig 4. The fraction of all reddened quasars in our sample, defined as having $A_V > 0.1$, was found to be, again with error bars corresponding to the 68% confidence interval, $f_{\rm Av>0.1} = N_{\rm Av>0.1}/N_{\rm total} = 0.39^{+0.09}_{-0.08}$ ($39\%^{+9}_{-8}$). Previously, Glikman et al. (2007, 2012); Urrutia et al. (2009) have defined red quasars as having $E(B-V) > 0.1$. We found that seven of the quasars in our parent sample satisfy this criterion, so that the fraction is again $f_{E(B-V)>0.1} = 21\%^{+9}_{-5}$, which is consistent with the findings of Glikman et al. (2007, 2012); Urrutia et al. (2009), see Sect. 7. The SDSS/BOSS photometric selection found 23 quasars, 5 of which have $A_V > 0.1$. This means that roughly 22% of the SDSS/BOSS photometrically selected quasars are classified as reddened, while 40% are expected. Hence an incompleteness of 45% in this particular optical quasar sample is observed.

In Table 1 we show the redshifts, both spectroscopic and photometric, along with the calculated reddening, A_V, both assuming SMC-like extinction and the extinction curve found by Zafar et al. (2015), and the corresponding reddening in terms of $E(B-V)$. The notes list the specific colors in which the individual objects do not meet the HAQ criteria.

The computed photometric redshifts generally agree well with the spectroscopically determined redshifts, both for the objects with public spectra and for the quasars we observed. We find a maximum difference of $|z_{\rm spec} - z_{\rm phot}| = 0.18$ (except for the extreme case of Q 095921.3+024412.4, see below), whereas for most objects the spectroscopic and photometric redshifts are determined well within $|z_{\rm spec} - z_{\rm phot}| < 0.1$. All but one of the seven HAQs show a pronounced amount of reddening ranging from $0.15 < A_V < 0.98$. Following the parameterization from

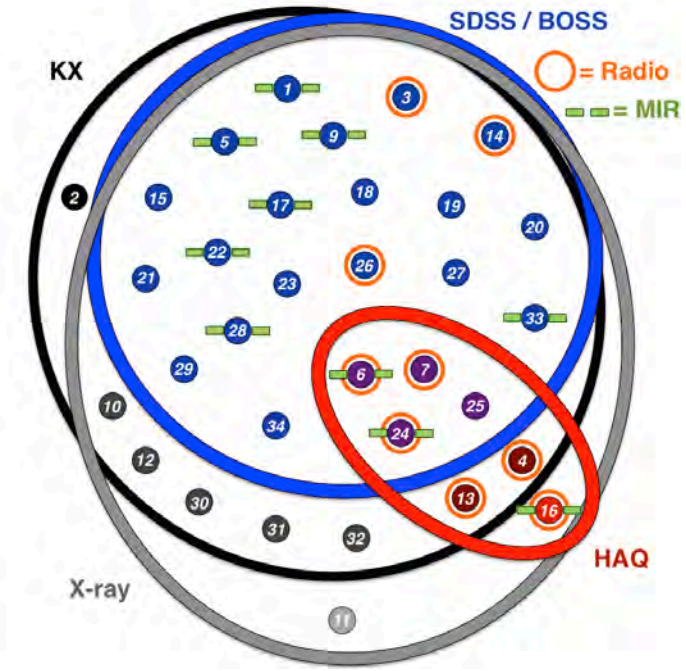

Fig. 3: Quantity diagram (a so-called Venn diagram) of the respective sub-populations of the 33 confirmed quasars. The numbers in each of the symbols represents the objects with the same numbering as in Table 1. The parent sample of quasars consists of $7/33 \sim 21\%$ HAQs. Only quasars 2 and 11 have been selected by one technique alone from KX selection or X-ray detection, respectively. Of the 13 quasars with $A_V > 0.1$, 6 were selected by the HAQ criteria, 11 were identified by the KX selection, 12 with X-ray detection, 6 had radio detections, 5 were from the photometric selection of SDSS/BOSS, and 4 of the reddened quasars were identified by the MIR selection.

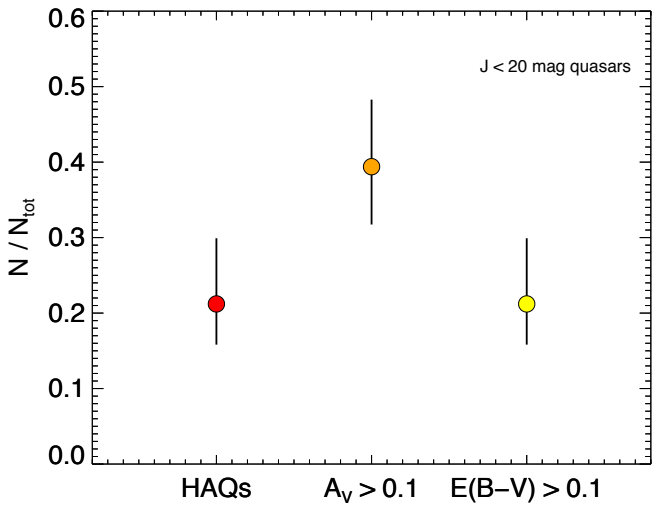

Fig. 4: Fractions of the HAQ-selected quasars, the quasars with $A_V > 0.1$, and the quasars with $E(B-V) > 0.1$ compared to the total. The error bars correspond to the 68% confidence interval.

Gordon et al. (2003), where (for SMC-like extinction)

$$R_V \equiv A_V/E(B-V),\ R_V = 2.74, \quad (4)$$

this corresponds to $0.05 < E(B-V) < 0.36$. The HAQs reddened by dust are at redshifts in the range $1.00 < z < 2.66$. The only HAQ with no sign of dust extinction is the object Q100050.1+022356.7 at $z = 3.37$. The distribution of redshifts and A_V of the HAQs from our parent sample agree well with the findings of Krogager et al. (2015), see Fig. 3 of their paper, for example. As mentioned, only four of the seven HAQs have been identified by the SDSS-III/BOSS program, which again is similar to the fraction found in the original HAQ survey, although from a much larger sample, where $409/901 \sim 45\%$ of the HAQ candidates had been observed as part of the SDSS (DR7) program before their study. In the spectrum of object Q095938.3+020450.1 (quasar 10) we found an indication of a damped Lyα absorption feature blueward of the strong Lyα emission line in the Lyα forest. The search for quasars reddened by intervening absorbers was the primary goal of the HAQ survey, but this object evaded selection by being slightly too blue ($H - K_s = -0.02$) for the HAQ criterion of $H - K_s > 0$. The optical colors are otherwise within the HAQ selection criteria, indicating the red nature ($A_V = 0.23$) of this object.

In Fig. 5, panels (a) and (b), we show the photometric colors of all the quasars from the parent sample in two optical/NIR color-color diagrams and in panel (c) the $g - r$ colors as a function of the reddening, A_V, assuming SMC-like extinction. Again, the respective symbols represent the individual selection methods used to identify each quasar as shown in panel (a), upper right corner. For comparison we show the photometry of main-sequence stars and M-dwarf stars in panel (a), illustrated by the yellow and red stars, respectively. In panel (b) the stellar track is outside the plotting region and is therefore absent. The stellar sources were obtained from the Hewett et al. (2006) catalog, where the yellow stellar track in general represents the densest region of the stellar locus. When we plot all the defined point sources from the full photometric COSMOS catalog used in our study, the main location in color-color space follows an equal track. In panel (a) the gray dashed line represents the selection line of the KX method formulated in Eq. 2. Panel (c) illustrates that the HAQs indeed are a part of the most reddened quasars in our sample. The quasars that were not selected by the HAQ criteria but still show a pronounced amount of reddening are either red in the gJK_s or the $J - K_s$ colors, suggesting that by refining the HAQ criteria, a larger and more complete sample of the reddest quasars can be obtained.

For one of the quasars, Q095921.3+024412.4 (quasar 7), we had to discard the spectroscopic redshift of $z = 3.623$ as determined by the BOSS program. This quasar is obscured and shows high reddening ($A_V = 0.98$) with only a few weak emission line signatures apparent. The available notes at the SDSS DR12 website report a poor χ^2 fit for the redshift determination of this quasar. For comparison, the photometric redshift from Salvato et al. (2011) was computed as $z_{\rm phot} = 0.030$. The redshift we suggest of $z = 1.004$, found when visually matching the spectrum to the composite quasar template, was also listed by Trump et al. (2009), who determined a value of $z = 1.0037 \pm 0.0054$.

6. Survey reliability

The success of a survey hinges critically upon obtaining the optimal balance between efficiency and completeness. In other words, being able to select a sample of candidates, which includes close to all of the objects of the targeted type, and close to nothing else. Below we review the individual surveys used to

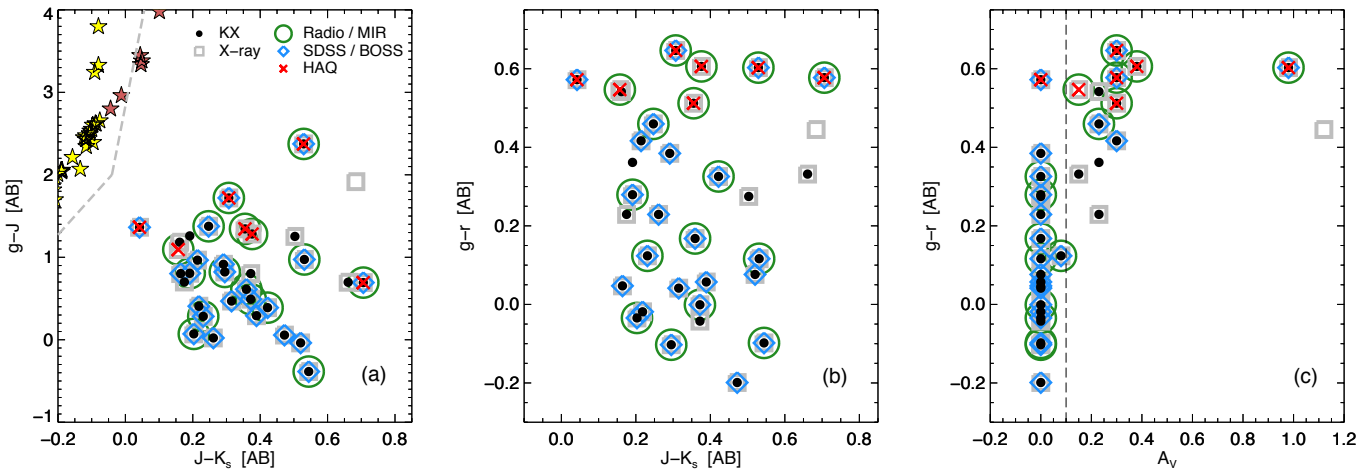

Fig. 5: *Panel (a) and (b):* Optical/NIR color-color diagrams of the 33 confirmed quasars. The respective symbols represent the individual selection method used to identify each quasar as defined by the legend. The yellow and red star symbols show the photometry of main-sequence and M-dwarf stars from the Hewett et al. (2006) catalog, respectively. *Panel (c):* The reddening, A_V, of the confirmed quasars as a function of their color in $g - r$. The HAQs contribute to about half of the population of reddened quasars defined as having $A_V > 0.1$ (black dashed line).

build our parent sample and discuss the completeness and reliability of each of the approaches.

6.1. Efficiency

Our parent sample was produced by only considering the brightest and spatially unresolved population of quasars obtained from six distinctive selection techniques. The conservative criteria we used of star-like morphology and $J \leq 20$ magnitude have introduced some significant bias (by design) when considering the general and complete AGN population. We required that the quasars were optically unresolved to remove objects with contributing host galaxy light and to be consistent with previous photometric selection approaches. The $J = 20$ magnitude cut ensured that our selection was complete down to the limiting depths in magnitude for each of the individual surveys. When comparing the different selection techniques, this cut allows the selection of quasars based on relatively shallow surveys to still be relevant.

To compare the SDSS/BOSS selected quasars from our parent sample to the full SDSS-III/BOSS sample, we extracted all the quasars from the DR12Q sample (Pâris et al. 2016, in prep.) within the C-COSMOS field, see Fig. 6. Here we show the full SDSS/BOSS DR12Q sample together with the confirmed quasars from our study to directly compare the two samples. In total, 42 quasars from the DR12Q sample have not been selected from our criteria but all had a counterpart in the photometric catalog. Of these, 25 quasars avoided selection by being too faint in the J band. However, most of the objects in the DR12Q sample have $J \leq 20.5$ mag, indicating that the cut in brightness is close to the limiting depth in magnitude up to which the SDSS/BOSS survey is complete. Furthermore, we found that 18 of 42 quasars in the DR12Q sample miss the selection because of extended spatial morphology in the photometric catalog, where most of these appear to be Seyfert galaxies in the SDSS database.

The survey that was suppressed the most by our requirement of optically unresolved morphology was the approach of X-ray selection. Without the point source criteria of the photometric

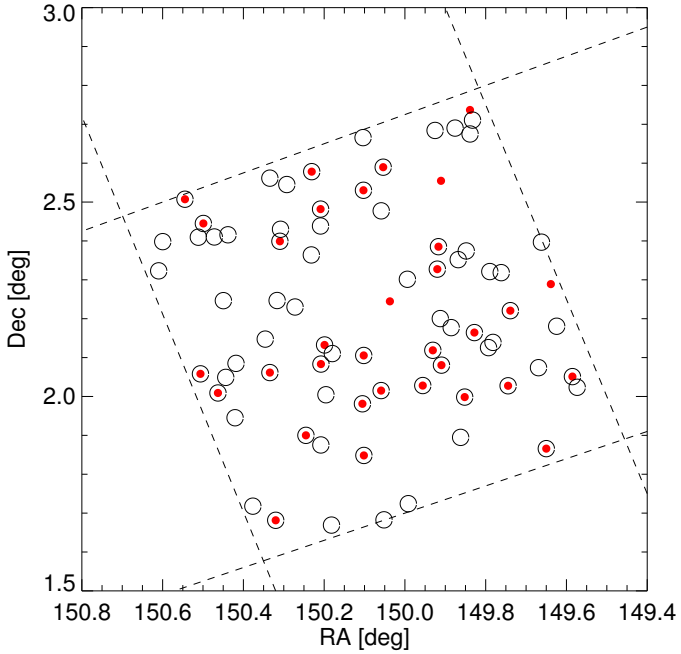

Fig. 6: Full SDSS-III/BOSS DR12Q sample (black circles) within the C-COSMOS field together with the confirmed quasars from our parent sample (red dots). About 60% of the DR12Q sample have not been selected by our criteria in morphology and/or brightness, where approximately 60% vs. 40% was due to $J > 20$ mag and optical resolved morphology, respectively.

catalog applied to the X-ray selected sample, we obtained 224 X-ray detected AGNs all brighter than $J = 20$ magnitude within the C-COSMOS field. That is, only $\sim 14\%$ of the X-ray selected sample is recovered using our morphology criteria, meaning that they have unresolved optical/NIR counterparts. Moreover, the MIR color-selected sample relying on *WISE* colors only detects 18 quasars in total, where only 10 (55%) of these have been con-

sidered in our study because of their unresolved morphology. This agrees with the findings of Gabor et al. (2009); Griffith & Stern (2010); Stern et al. (2012), who have examined the optical morphologies of AGNs in the COSMOS field where ∼ 50% of the brightest MIR color-selected population is extended or unresolved, respectively. The high density of the population of optically resolved X-ray selected AGNs is higher than has previously been reported. Griffith & Stern (2010) found that 72% of the X-ray selected sample is optically resolved, but only for the faintest population based on *XMM-Newton* observations (well beyond $J = 20$ mag). Some of the discrepancy for the brightest population could be explained by the more sensitive *Chandra* satellite, but the fraction of resolved X-ray AGNs is still incomparably higher than expected. Since we only considered the brightest and spatially unresolved population of quasars, the sub-population of reddened and extremely obscured quasars can be even higher when examining the entire population of optically unresolved and extended X-ray and/or MIR selected quasars, see, for example, Gavignaud et al. (2006); Fiore et al. (2008).

To show them in context to each other, we plotted the optically extended and point source X-ray detected quasars, respectively, as a function of redshift in Fig. 7. To be consistent, only the brightest population ($J \leq 20$ mag) of quasars, again within the C-COSMOS field, is shown. Below redshifts $z \lesssim 1$, the fraction of AGNs with dominating light from the host galaxy causing observed extended optical morphology (at the resolution of the CFHT+Subaru i band) is more dominant than the spatially unresolved population. At higher redshifts we found that the optically unresolved population of bright quasars is representative of the full underlying population with only a few optically extended quasars rejected for our parent sample. Most of these appear compact in the HST images, but still show signs of elliptical or spiral-like morphology.

For the SDSS/BOSS photometrically selected quasars the invoked limit in brightness for our parent sample was close to the completeness limit for this particular survey. For some of the deepest COSMOS surveys the limit down to which these are complete is several magnitudes deeper. For example, 172 of the X-ray selected quasars (when only considering the optically unresolved population) have magnitudes fainter than $J \geq 20$ mag, whereas only 33 of the radio selected and 11 of the mid-infrared selected quasars are fainter than this magnitude limit. By applying the cut at NIR wavelengths, the selection becomes less biased against quasars reddened by dust than in optical magnitude limited studies. We highlight that none of the defined selection techniques detect all the quasars from our parent sample. The X-ray selection technique found the most sources, where this particular approach of identifying quasars has been credited as being the most reliable (Brandt & Hasinger 2005), with the only exception being the quasar CQ095833.3+021720.4. A high absorption is observed in this object, which could explain the non-detection. The reason might also be that like Q100210.7+023026.2, this quasar is located in a region of short exposure.

6.2. Degree of contamination

Even though the X-ray selection technique detects most of the bright AGNs (regardless of optical morphology), great caution has to be applied when building large X-ray selected quasar samples. When considering all the optical/NIR point source counterparts (brighter than $J = 20$ mag) of the *Chandra* X-ray sample, we found an additional 31 sources that were either photometrically or spectroscopically classified as stars. That is, when the brightest population of optically unresolved X-ray selected

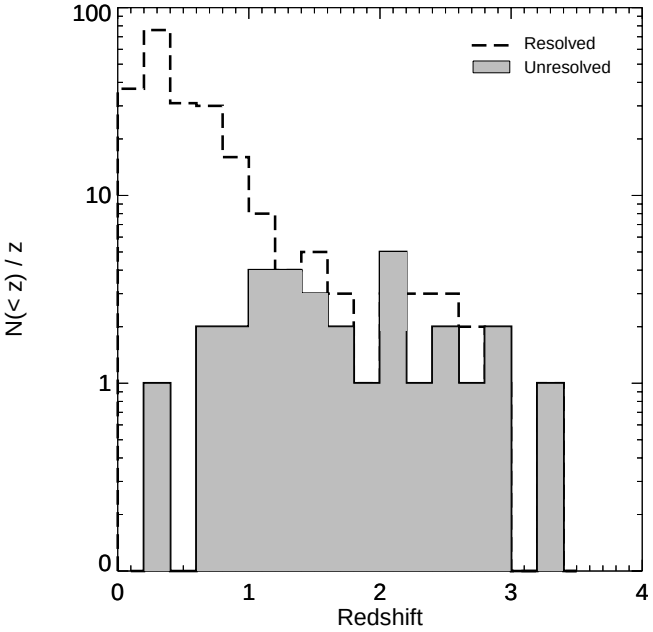

Fig. 7: Histogram of the redshift distribution of the brightest ($J < 20$ mag) optically resolved and unresolved *Chandra* X-ray detected quasars in the COSMOS field, respectively. At redshifts below $z \lesssim 1$ the incompleteness of our parent sample due to morphology is most severe, while at $z > 1$ the unresolved population of quasars is representative of the full population.

quasars is observed blindly, ∼ 50% will show stellar contamination. According to the photometric study of the X-ray selected COSMOS sample by Salvato et al. (2009, 2011), these could be discarded before selection either by having existing spectra classifying them as stars or by having seemingly stellar-like colors in optical/NIR color-color space. In addition, two radio-loud sources with an optically unresolved optical/NIR counterpart brighter than $J = 20$ mag were also initially present in our sample, but were removed in the same way. We chose to eliminate all objects located in the stellar locus to obtain a conservative estimate of the population of reddened quasars. However, since selection of quasars with apparent optical/NIR colors similar to that of stars is only possible at short (e.g., X-ray) or long (e.g., radio) wavelengths, these would not be detected by any standard optical/NIR color selection techniques, and rejection of them has to be considered carefully.

When we applied the KX selection line in gJK_s color-color space, that is, when we separated objects with and without K_s-band excess, ten additional contaminating sources were obtained. The contaminants with existing spectra consist of one L dwarf, one white dwarf, one $A0$ star, and one carbon star. The remaining KX candidates were eliminated after being processed by the photo-z algorithm. The majority of these were classified as stars by the code, while only two were classified as blue galaxies. The reduced χ^2_q from the best fit obtained with the AGN templates in the photometric COSMOS catalog all show relative poor fits as well. This was not the primary motivation for eliminating these sources, however, since the AGN templates are in no way fully inclusive and therefore not reliable (Ilbert et al. 2013). The two objects CQ095938.6+203316.7 and CQ100008.9+021440.7 were discarded by this process. For CQ095938.6+203316.7, we simply disregarded it before run-

ning the candidates through the algorithm because of its extended morphology in the SDSS imaging. The other quasar, CQ100008.9+021440.7, although selected by the general KX color criteria, was classified as being a star by the photo-z code. This object was spectroscopically confirmed as being a quasar, but indeed with high absorption and very red (and star-like) optical colors, especially in $u-g$. We chose to follow it up spectroscopically since it was identified by many other selection techniques, see, for example, Table 1. Although higher contamination is observed without applying this algorithm to the KX-selected objects, the code makes the specific output sample less complete.

Even though the HAQ survey is in no way complete, the purity of the sample without further considerations of template fitting, for instance, is unparalleled by any of the other surveys. All of the seven HAQ candidates selected from optical/NIR photometry alone were confirmed as being quasars. In the other samples, for example, the X-ray detected, the KX-selected, and the radio-detected quasars, additional photometric χ^2 fitting was executed to effectively remove stellar contamination. Selecting quasars in the COSMOS field also benefits from the previous extensive observations from numerous surveys, which had spectroscopically classified the majority of the stellar contamination.

7. Discussion and conclusions

We used the available multiwavelength data of various COSMOS surveys to define a complete parent sample of bright and spatially unresolved quasars that are representative of the full underlying population. Specifically, the sample was produced by using six distinctive techniques to identify quasars ranging from X-ray to radio wavelengths. From this parent sample of quasars, we determined the fraction of high A_V quasars (HAQs), a sub-population of quasars shown to be underrepresented in optical surveys (Fynbo et al. 2013; Krogager et al. 2015). We found that the total population of quasars in our sample consists of $f_{\rm HAQ} = 21\%^{+9}_{-5}$ HAQs. The general population of reddened quasars with $A_V > 0.1$ constitutes $f_{\rm A_V>0.1} = 39\%^{+9}_{-8}$ of the parent sample. The calculated fractions agree well with other similar studies reported in the literature. We chose the HAQ criteria to define the optical/NIR photometrically selected sample as one representation and quasars with $A_V > 0.1$ as another. We found a value slightly above estimates from optically selected samples, see, for instance, the study by Richards et al. (2003). Here they determined that only ∼6% of a subsample of quasars selected from the SDSS is reddened following a SMC-like extinction curve, but also that ∼ 15% of reddened quasars will be missing in the SDSS. In our sample, the SDSS/BOSS photometric selection functions detect 23 quasars, out of which 5 have $A_V > 0.1$, meaning that about 22% of the quasars in SDSS are reddened, while 40% are expected, which translates into an incompleteness of 46%. For the photometric sample of SDSS/BOSS, the completeness fraction is then $5/(23 \times 0.4) = 54\%$.

Selections of reddened quasars detected in radio with FIRST and matched to the NIR survey 2MASS have been executed as well, developed as another approach of alleviating the known bias against dust-reddened quasars in optically selected samples. Glikman et al. (2004) estimated the missing population of reddened quasars in optical surveys to be in the range ∼ 3 – 20%. Subsequently, Glikman et al. (2007); Urrutia et al. (2009) estimated a higher fraction of >∼ 20% based on the spectroscopic follow-up of their FIRST-2MASS-selected reddened quasars. Glikman et al. (2012) found that reddened quasars make up ≲ 15% – 20% of the radio-emitting bright quasar population

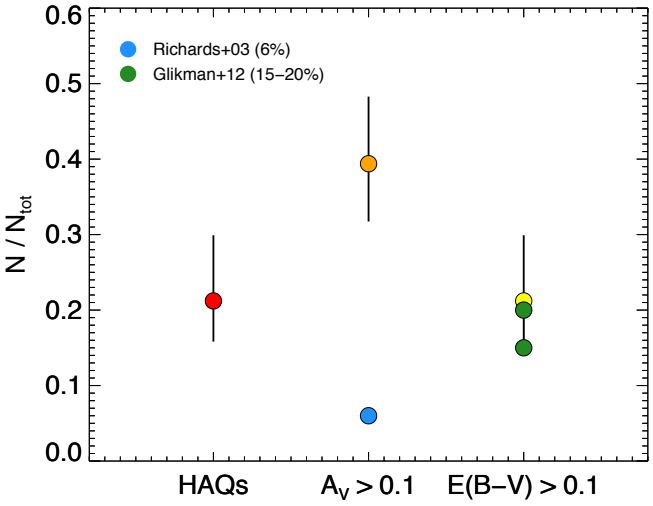

Fig. 8: Same as Fig. 4, but with comparisons to the fractions of reddened quasars found by Richards et al. (2003) and Glikman et al. (2012). Richards et al. (2003) considered sources with $E(B-V) > 0.04 \sim A_V > 0.1$ as reddened, while Glikman et al. (2012) used the definition of $E(B-V) > 0.1$ to identify reddened quasars.

from their sample, defined as quasars with $E(B-V) > 0.1$. For comparison, we found that $21\%^{+9}_{-5}$ of the quasars from our parent sample had $E(B-V) > 0.1$, assuming the extinction curve of the SMC (see, e.g., Fig 8 for a graphical comparison). This is of course still dependent on how the parent population is defined and how deep the limiting brightness is (since fainter samples will allow for a selection of even more reddened, i.e., optically faint quasars). Richards et al. (2006) estimated an upper limit of < 30% for the fraction of reddened quasars that are missed in optical samples such as the SDSS, based on the $u-g$ and $g-r$ colors of a MIR color-selected sample of quasars. They based this on the conclusion that ∼ 70% of the MIR color-selected sample had blue optical colors consistent with what has previously been reported in optical UVX surveys (having $u-g < 0.6$ and $g-r < 0.6$, respectively). This contradicts our findings in Sect. 5, however. In Fig. 5 we showed that only about half of the reddest population of quasars, with $A_V > 0.1$, have red optical colors of $g-r > 0.5$ (and only three of these quasars have $g-r > 0.6$), indicating that the 30% upper limit in the density of reddened quasars is not reliable.

Based on our results, we conclude that the HAQ selection is reliable in detecting reddened quasars. Seven out of the 13 reddened quasars are not selected, but these are all except for one quasars with too little reddening to pass the $g-r$ color cut, see Fig. 9. One apparently reddened quasar, CQ095938.6+023316.7, looks blue in the optical spectrum, but the NIR photometry has substantial excess over that expected from an unreddened quasar template. This could be explained by a significant contribution of light from the host galaxy to the NIR photometry. This is consistent with the morphology of the object in the HST image, which has significant extended fuzz around the point spread function of the quasar. The KX, X-ray, and MIR selections are more complete, but not as tailored to select exclusively reddened quasars.

At redshifts below $z \lesssim 1$, spatially resolved quasars are dominant, meaning that our parent sample of quasars in this redshift

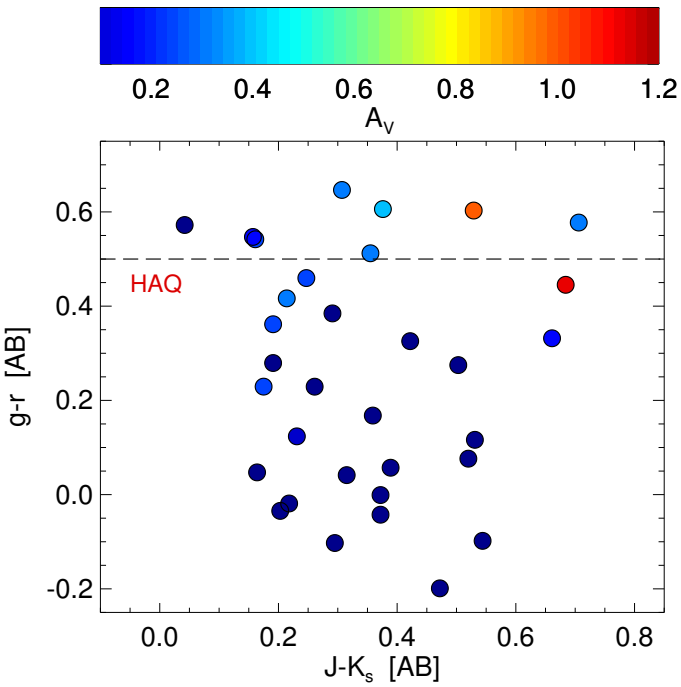

Fig. 9: Optical/NIR color-color diagram of the 33 quasars from the parent sample, color-coded as a function of their reddening, A_V (see the top legend). The HAQ $g - r$ color cut is shown by the dashed line. This conservative cut yields a reliable sample of reddened quasars only, while more relaxed color criteria are needed to obtain a more complete sample of reddened quasars, see also Fig. 5 (middle and right panel).

range is not representative of the total population of AGNs. At higher redshifts, however, we found that the population of spatially unresolved sources is representative of the full underlying population of quasars. The HAQ and in general the reddened sub-population of quasars thus make up a considerable fraction of the brightest optically unresolved sources. Studies of the nature and evolution of quasars (and in general SMBHs) through cosmic time must include this in their considerations to remove the otherwise distorted perspective originating from optical quasar surveys.

Acknowledgements. We would like to thank the anonymous referee for a constructive and insightful report that gave valuable suggestions to present the results of this paper in the best possible way. Furthermore, we would like to thank D. Malesani and C. Grillo for carrying out the observations of the candidate quasars at the NOT. Otherwise we would not have succeeded in obtaining a 100% redshift completeness of our parent sample. We also wish to thank I. Pâris for her help with the SDSS-III/BOSS DR12Q sample and the general SDSS/BOSS selection functions. The research leading to these results has received funding from the European Research Council under the European Union's Seventh Framework Program (FP7/2007-2013)/ERC Grant agreement no. EGGS-278202. JKK acknowledges support from the European Union's Seventh Framework Programme for research and innovation under the Marie-Curie grant agreement no. 600207 with reference DFF-MOBILEX–5051-00115. MV gratefully acknowledges support from the Danish Council for Independent Research via grant no. DFF 4002-00275. The data presented here were obtained with ALFOSC, which is provided by the Instituto de Astrofisica de Andalucia (IAA) under a joint agreement with the University of Copenhagen and NOTSA. Based on data products from observations made with ESO Telescopes at the La Silla Paranal Observatory under ESO programme ID 179.A-2005 and on data products produced by TERAPIX and the Cambridge Astronomy Survey Unit on behalf of the UltraVISTA consortium. Funding for SDSS-III has been provided by the Alfred P. Sloan Foundation, the Participating Institutions, the National Science Foundation, and the U.S. Department of Energy Office of Science. The SDSS-III web site is http://www.sdss3.org/. SDSS-III is managed by the Astrophysical Research Consortium for the Participating Institutions of the SDSS-III Collaboration including the University of Arizona, the Brazilian Participation Group, Brookhaven National Laboratory, Carnegie Mellon University, University of Florida, the French Participation Group, the German Participation Group, Harvard University, the Instituto de Astrofisica de Canarias, the Michigan State/Notre Dame/JINA Participation Group, Johns Hopkins University, Lawrence Berkeley National Laboratory, Max Planck Institute for Astrophysics, Max Planck Institute for Extraterrestrial Physics, New Mexico State University, New York University, Ohio State University, Pennsylvania State University, University of Portsmouth, Princeton University, the Spanish Participation Group, University of Tokyo, University of Utah, Vanderbilt University, University of Virginia, University of Washington, and Yale University.

References

Abazajian, K., Adelman-McCarthy, J. K., Agüeros, M. A., et al. 2004, AJ, 128, 502
Allen, J. T., Hewett, P. C., Maddox, N., Richards, G. T., & Belokurov, V. 2011, MNRAS, 410, 860
Assef, R. J., Stern, D., Kochanek, C. S., et al. 2013, ApJ, 772, 26
Baloković, M., Smolčić, V., Ivezić, Ž., et al. 2012, ApJ, 759, 30
Banerji, M., McMahon, R. G., Hewett, P. C., et al. 2012, MNRAS, 427, 2275
Becker, R. H., Gregg, M. D., Hook, I. M., et al. 1997, ApJ, 479, L93
Becker, R. H., White, R. L., & Helfand, D. J. 1995, ApJ, 450, 559
Blanton, M. R. & Roweis, S. 2007, AJ, 133, 734
Brandt, W. N. & Hasinger, G. 2005, ARA&A, 43, 827
Brusa, M., Civano, F., Comastri, A., et al. 2010, ApJ, 716, 348
Bruzual, G. & Charlot, S. 2003, MNRAS, 344, 1000
Cameron, E. 2011, PASA, 28, 128
Capak, P., Aussel, H., Ajiki, M., et al. 2007, ApJS, 172, 99
Cappelluti, N., Brusa, M., Hasinger, G., et al. 2009, A&A, 497, 635
Civano, F., Elvis, M., Brusa, M., et al. 2012, ApJS, 201, 30
Croom, S. M., Smith, R. J., Boyle, B. J., et al. 2004, MNRAS, 349, 1397
Croom, S. M., Warren, S. J., & Glazebrook, K. 2001, MNRAS, 328, 150
Cutri, R. M. & et al. 2013, VizieR Online Data Catalog, 2328
Dawson, K. S., Schlegel, D. J., Ahn, C. P., et al. 2013, AJ, 145, 10
Donley, J. L., Koekemoer, A. M., Brusa, M., et al. 2012, ApJ, 748, 142
Donley, J. L., Rieke, G. H., Pérez-González, P. G., & Barro, G. 2008, ApJ, 687, 111
Elvis, M., Civano, F., Vignali, C., et al. 2009, ApJS, 184, 158
Fan, X. 1999, AJ, 117, 2528
Fazio, G. G., Hora, J. L., Allen, L. E., et al. 2004, ApJS, 154, 10
Fiore, F., Grazian, A., Santini, P., et al. 2008, ApJ, 672, 94
Fitzpatrick, E. L. & Massa, D. 2005, AJ, 130, 1127
Fynbo, J. P. U., Krogager, J.-K., Venemans, B., et al. 2013, ApJS, 204, 6
Fynbo, J. P. U., Ledoux, C., Noterdaeme, P., et al. 2011, MNRAS, 413, 2481
Gabor, J. M., Impey, C. D., Jahnke, K., et al. 2009, ApJ, 691, 705
Gavignaud, I., Bongiorno, A., Paltani, S., et al. 2006, A&A, 457, 79
Gibson, R. R., Jiang, L., Brandt, W. N., et al. 2009, ApJ, 692, 758
Glikman, E., Gregg, M. D., Lacy, M., et al. 2004, ApJ, 607, 60
Glikman, E., Helfand, D. J., White, R. L., et al. 2007, ApJ, 667, 673
Glikman, E., Urrutia, T., Lacy, M., et al. 2012, ApJ, 757, 51
Glikman, E., Urrutia, T., Lacy, M., et al. 2013, ApJ, 778, 127
Gordon, K. D., Clayton, G. C., Misselt, K. A., Landolt, A. U., & Wolff, M. J. 2003, ApJ, 594, 279
Graham, M. J., Djorgovski, S. G., Drake, A. J., et al. 2014, MNRAS, 439, 703
Gregg, M. D., Lacy, M., White, R. L., et al. 2002, ApJ, 564, 133
Griffith, R. L. & Stern, D. 2010, AJ, 140, 533
Hasinger, G., Cappelluti, N., Brunner, H., et al. 2007, ApJS, 172, 29
Heintz, K. E., Fynbo, J. P. U., & Høg, E. 2015, A&A, 578, A91
Hewett, P. C., Warren, S. J., Leggett, S. K., & Hodgkin, S. T. 2006, MNRAS, 367, 454
Hopkins, P. F., Strauss, M. A., Hall, P. B., et al. 2004, AJ, 128, 1112
Ilbert, O., Capak, P., Salvato, M., et al. 2009, ApJ, 690, 1236
Ilbert, O., McCracken, H. J., Le Fèvre, O., et al. 2013, A&A, 556, A55
Ivezić, Ž., Menou, K., Knapp, G. R., et al. 2002, AJ, 124, 2364
Kaplan, K. F., Prochaska, J. X., Herbert-Fort, S., Ellison, S. L., & Dessauges-Zavadsky, M. 2010, PASP, 122, 619
Koekemoer, A. M., Aussel, H., Calzetti, D., et al. 2007, ApJS, 172, 196
Krawczyk, C. M., Richards, G. T., Gallagher, S. C., et al. 2015, AJ, 149, 203
Krogager, J.-K., Fynbo, J. P. U., Noterdaeme, P., et al. 2016, MNRAS, 455, 2698
Krogager, J.-K., Geier, S., Fynbo, J. P. U., et al. 2015, ApJS, 217, 5
LaMassa, S. M., Civano, F., Brusa, M., et al. 2016, ApJ, 818, 88
Lawrence, A., Warren, S. J., Almaini, O., et al. 2007, MNRAS, 379, 1599
Leauthaud, A., Massey, R., Kneib, J.-P., et al. 2007, ApJS, 172, 219
Maddox, N., Hewett, P. C., Péroux, C., Nestor, D. B., & Wisotzki, L. 2012, MNRAS, 424, 2876

Maddox, N., Hewett, P. C., Warren, S. J., & Croom, S. M. 2008, MNRAS, 386, 1605
Mateos, S., Alonso-Herrero, A., Carrera, F. J., et al. 2013, MNRAS, 434, 941
Mateos, S., Alonso-Herrero, A., Carrera, F. J., et al. 2012, MNRAS, 426, 3271
Matthews, T. A. & Sandage, A. R. 1963, ApJ, 138, 30
McCracken, H. J., Milvang-Jensen, B., Dunlop, J., et al. 2012, A&A, 544, A156
Nikutta, R., Hunt-Walker, N., Nenkova, M., Ivezić, Ž., & Elitzur, M. 2014, MNRAS, 442, 3361
Noterdaeme, P., Petitjean, P., Carithers, W. C., et al. 2012, A&A, 547, L1
Noterdaeme, P., Petitjean, P., Ledoux, C., et al. 2010, A&A, 523, A80
Noterdaeme, P., Petitjean, P., Ledoux, C., & Srianand, R. 2009, A&A, 505, 1087
Oke, J. B. 1974, ApJS, 27, 21
Pâris, I., Petitjean, P., Aubourg, É., et al. 2014, A&A, 563, A54
Peth, M. A., Ross, N. P., & Schneider, D. P. 2011, AJ, 141, 105
Richards, G. T., Fan, X., Newberg, H. J., et al. 2002, AJ, 123, 2945
Richards, G. T., Hall, P. B., Vanden Berk, D. E., et al. 2003, AJ, 126, 1131
Richards, G. T., Lacy, M., Storrie-Lombardi, L. J., et al. 2006, ApJS, 166, 470
Ross, N. P., Myers, A. D., Sheldon, E. S., et al. 2012, ApJS, 199, 3
Salvato, M., Hasinger, G., Ilbert, O., et al. 2009, ApJ, 690, 1250
Salvato, M., Ilbert, O., Hasinger, G., et al. 2011, ApJ, 742, 61
Schinnerer, E., Sargent, M. T., Bondi, M., et al. 2010, ApJS, 188, 384
Schinnerer, E., Smolčić, V., Carilli, C. L., et al. 2007, ApJS, 172, 46
Schlegel, D. J., Finkbeiner, D. P., & Davis, M. 1998, ApJ, 500, 525
Schmidt, K. B., Marshall, P. J., Rix, H.-W., et al. 2010, ApJ, 714, 1194
Schmidt, M. 1963, Nature, 197, 1040
Schneider, D. P., Richards, G. T., Hall, P. B., et al. 2010, AJ, 139, 2360
Scoville, N., Abraham, R. G., Aussel, H., et al. 2007a, ApJS, 172, 38
Scoville, N., Aussel, H., Brusa, M., et al. 2007b, ApJS, 172, 1
Secrest, N. J., Dudik, R. P., Dorland, B. N., et al. 2015, ApJS, 221, 12
Selsing, J., Fynbo, J. P. U., Christensen, L., & Krogager, J.-K. 2016, A&A, 585, A87
Sikora, M., Stawarz, Ł., & Lasota, J.-P. 2007, ApJ, 658, 815
Skrutskie, M. F., Cutri, R. M., Stiening, R., et al. 2006, AJ, 131, 1163
Stern, D., Assef, R. J., Benford, D. J., et al. 2012, ApJ, 753, 30
Trump, J. R., Impey, C. D., Elvis, M., et al. 2009, ApJ, 696, 1195
Urrutia, T., Becker, R. H., White, R. L., et al. 2009, ApJ, 698, 1095
Urry, C. M. & Padovani, P. 1995, PASP, 107, 803
van Dokkum, P. G. 2001, PASP, 113, 1420
Wang, J.-G., Zhou, H.-Y., Ge, J., et al. 2012, ApJ, 760, 42
Warren, S. J., Hambly, N. C., Dye, S., et al. 2007, MNRAS, 375, 213
Warren, S. J., Hewett, P. C., & Foltz, C. B. 2000, MNRAS, 312, 827
Webster, R. L., Francis, P. J., Petersont, B. A., Drinkwater, M. J., & Masci, F. J. 1995, Nature, 375, 469
Werner, M. W., Roellig, T. L., Low, F. J., et al. 2004, ApJS, 154, 1
Wright, E. L., Eisenhardt, P. R. M., Mainzer, A. K., et al. 2010, AJ, 140, 1868
York, D. G., Adelman, J., Anderson, Jr., J. E., et al. 2000, AJ, 120, 1579
Zafar, T., Møller, P., Watson, D., et al. 2015, A&A, 584, A100

8. Appendix

See next page.

Fig. 10: Here we present all of the images (at the top), spectra (black solid line), and the photometric data points (purple dots in the $u, g, r, i, z, Y, J, H, K_s$ filters) for each of the confirmed quasars. Overplotted is the composite quasar template with and without reddening (red and blue lines, respectively). The redshift and amount of reddening are shown in the upper left corner, while the object name and technique used to select this particular object are listed in the upper right corner. Below each object we show the SDSS/BOSS selection flags.

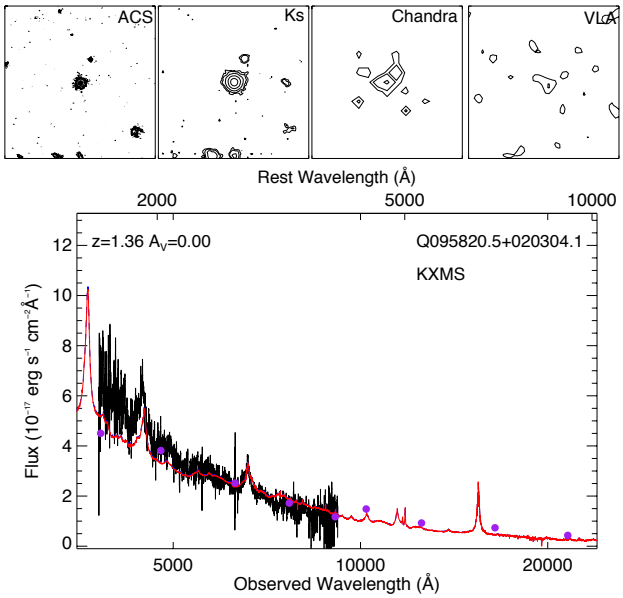

1: QSO_FAINT, SERENDIP_BLUE

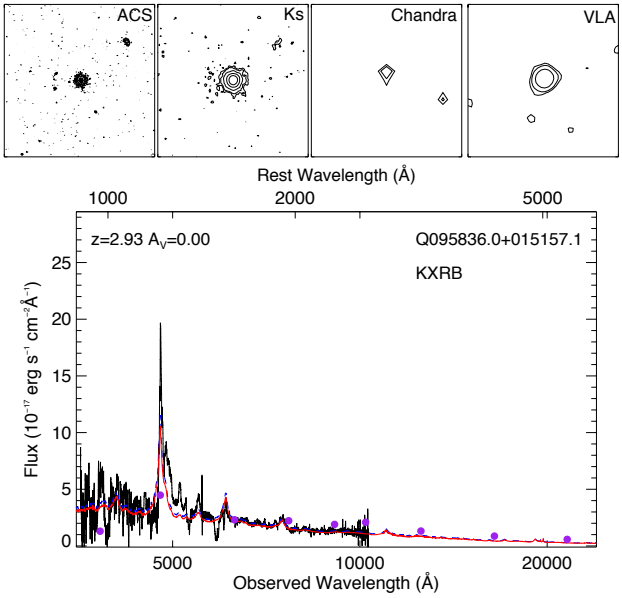

3: QSO_KNOWN_MIDZ, QSO_NN, QSO_KDE, QSO_CORE_MAIN

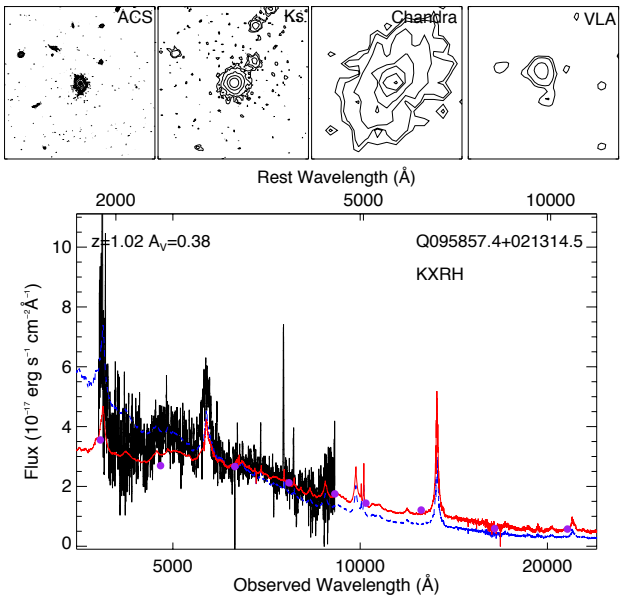

4: QSO_FAINT, ROSAT_D, ROSAT_C, ROSAT_B

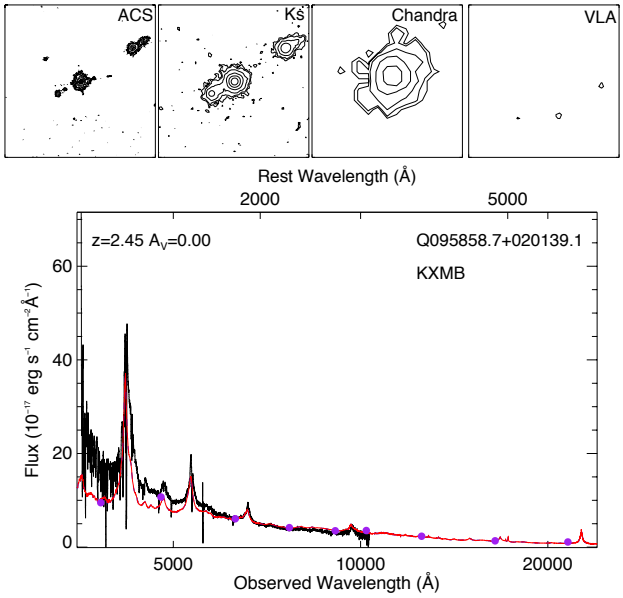

5: QSO_KNOWN_MIDZ, QSO_NN, QSO_KDE, QSO_CORE_MAIN

Fig. 9: *Continued*

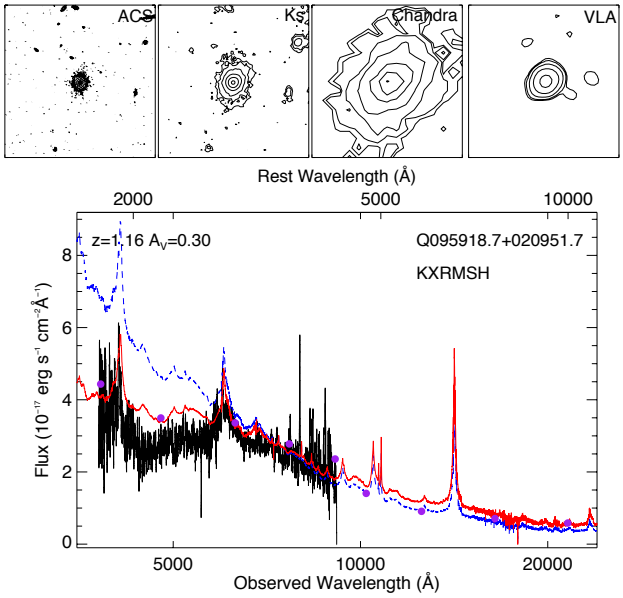

6: QSO_FAINT, SERENDIP_FIRST, SERENDIP_BLUE

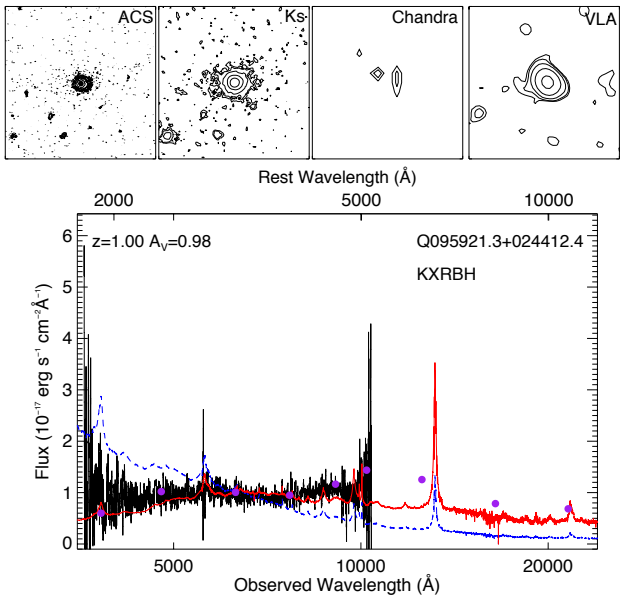

7:
QSO_FIRST_BOSS, QSO_KDE, QSO_BONUS_MAIN

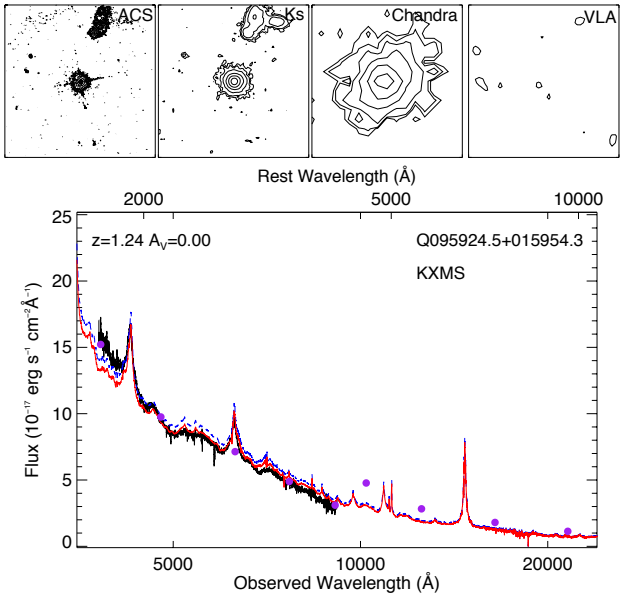

9: SEGUE2_CHECKED

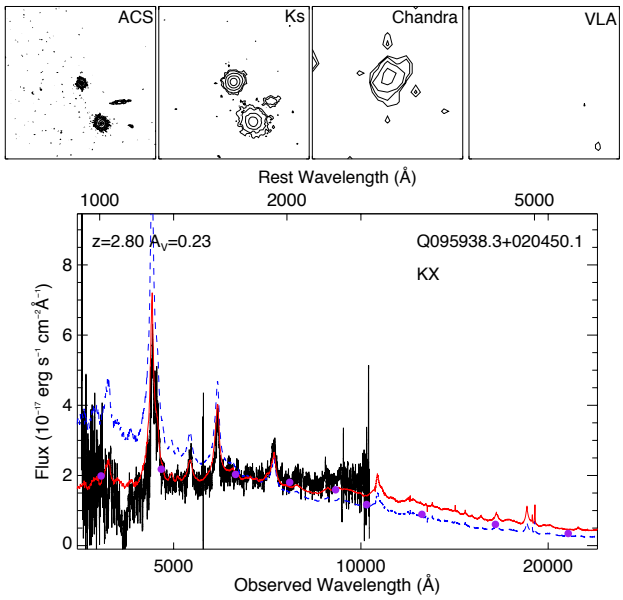

10: CHANDRAv1

Fig. 8: *Continued*

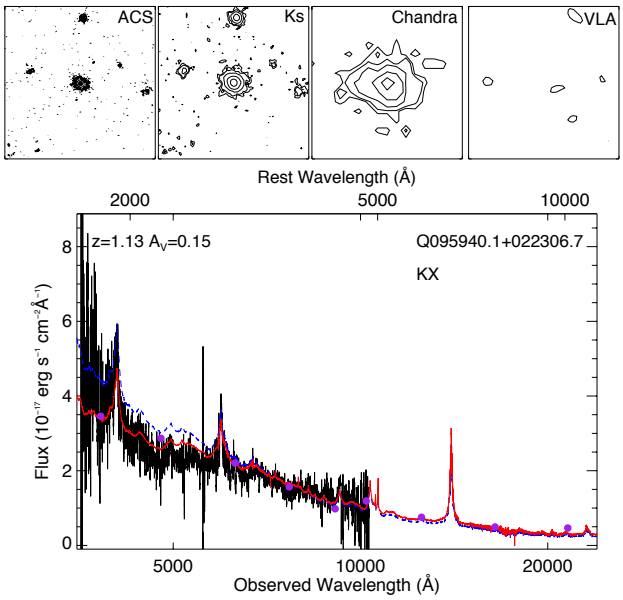

12: CHANDRAv1

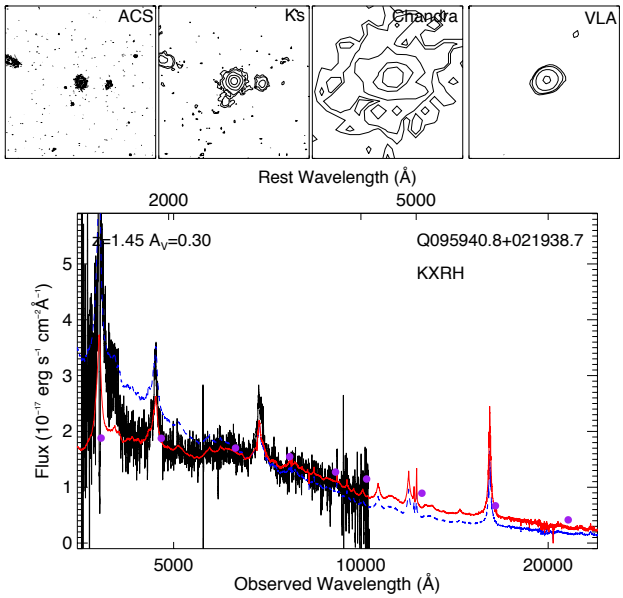

13: CHANDRAv1

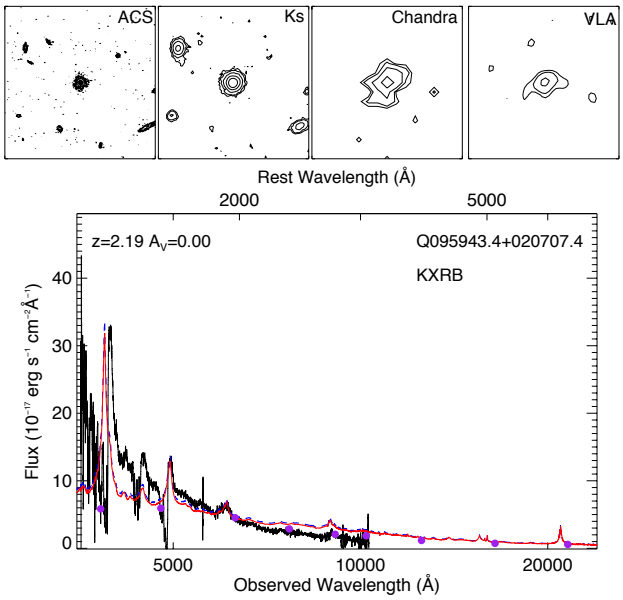

14: QSO_KDE, QSO_BONUS_MAIN, CHANDRAv1

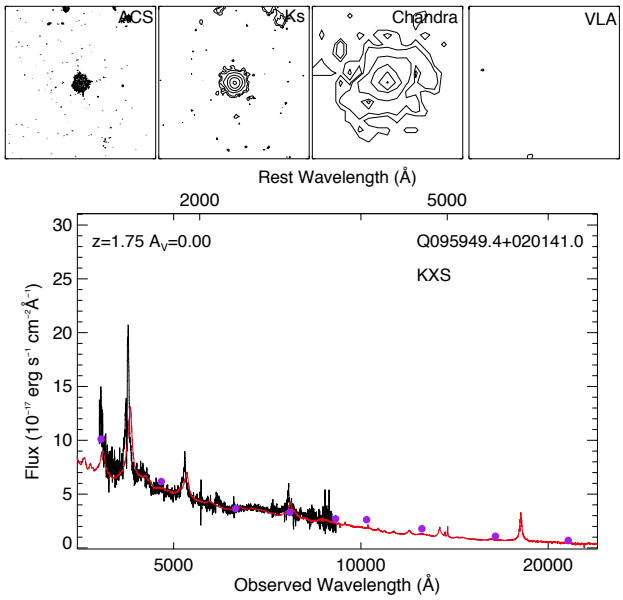

15: SERENDIP_BLUE, QSO_SKIRT

Fig. 7: *Continued*

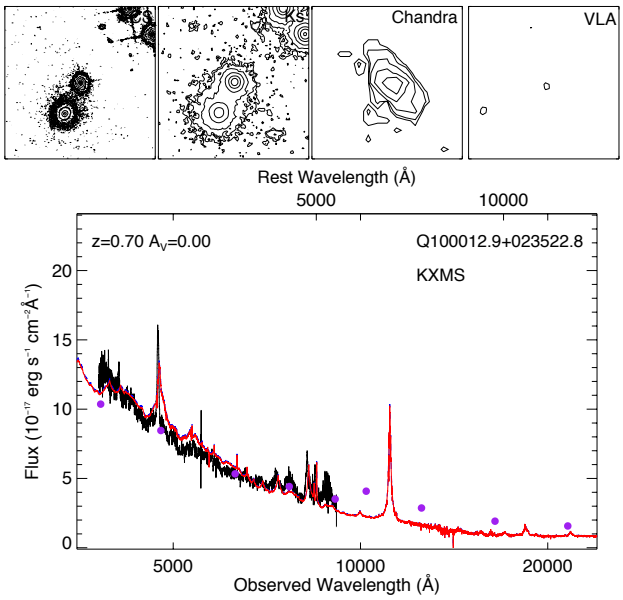

17: QSO_SKIRT

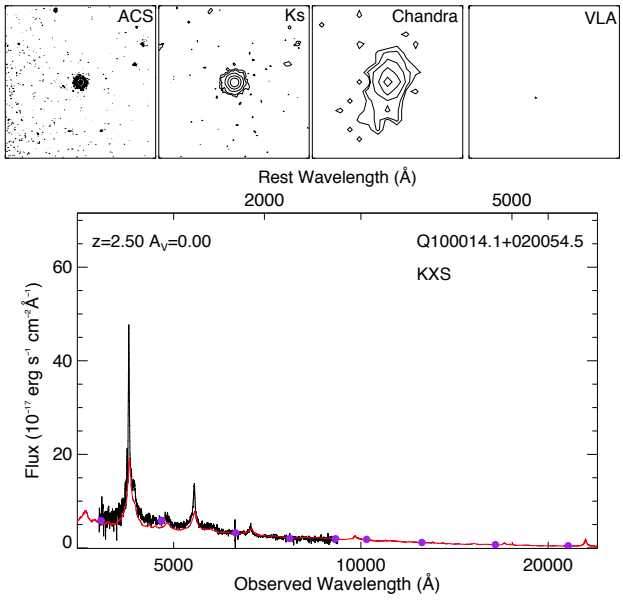

18: QSO_FAINT, SERENDIP_BLUE

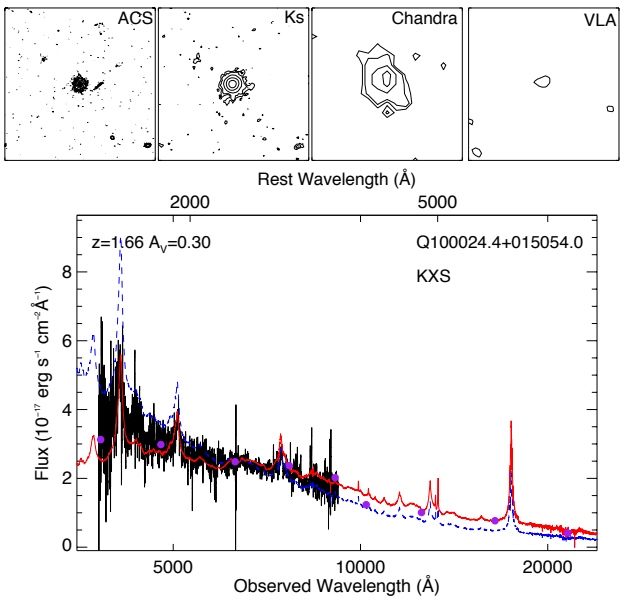

19: QSO_FAINT, SERENDIP_BLUE

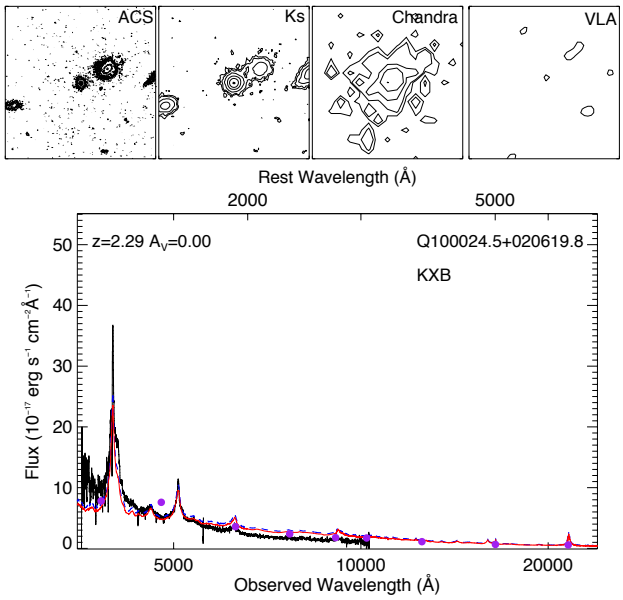

20: QSO_NN, QSO_KDE, QSO_CORE_MAIN, QSO_BONUS_MAIN, CHANDRAv1

Fig. 6: *Continued*

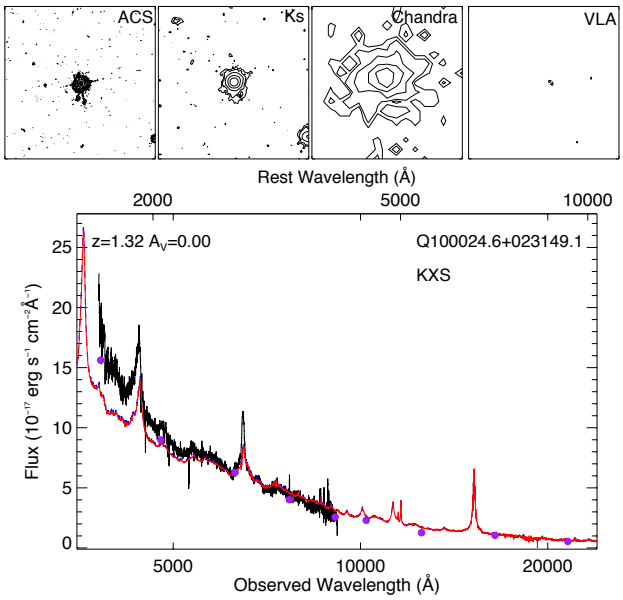

21: SERENDIP_BLUE, QSO_SKIRT

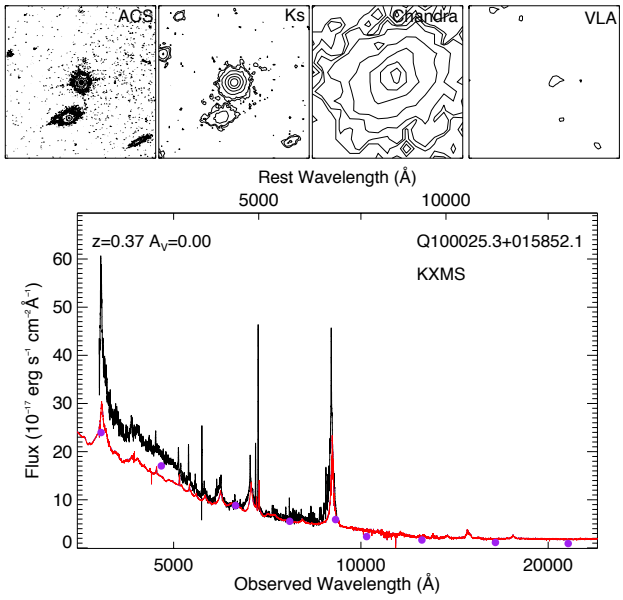

22: QSO_SKIRT, QSO_HIZ

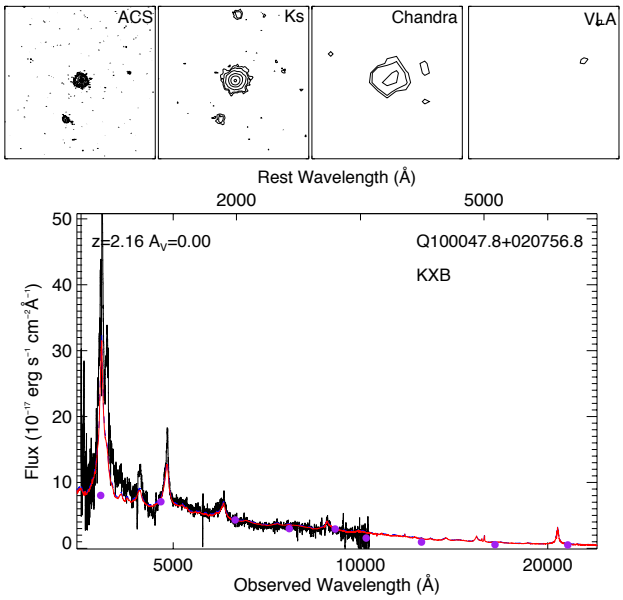

23: QSO_NN, QSO_KDE, QSO_BONUS_MAIN, CHANDRAv1

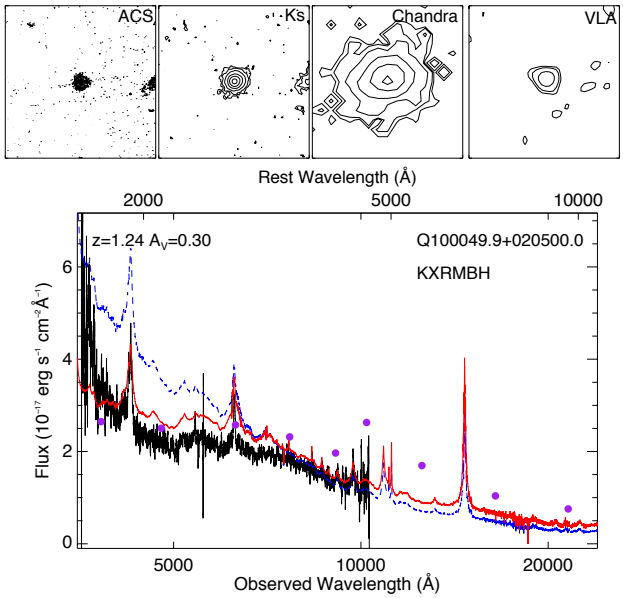

24: QSO_BONUS_MAIN, CHANDRAv1

Fig. 5: *Continued*

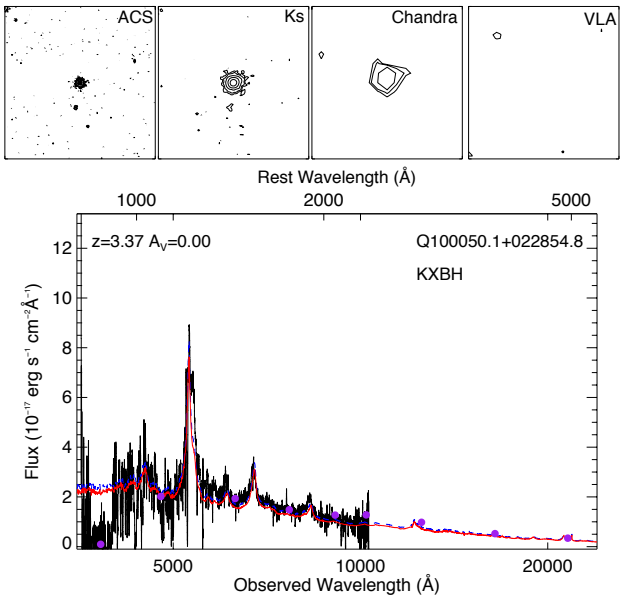

25: QSO_NN, QSO_KDE, QSO_CORE_MAIN, QSO_BONUS_MAIN, CHANDRAv1

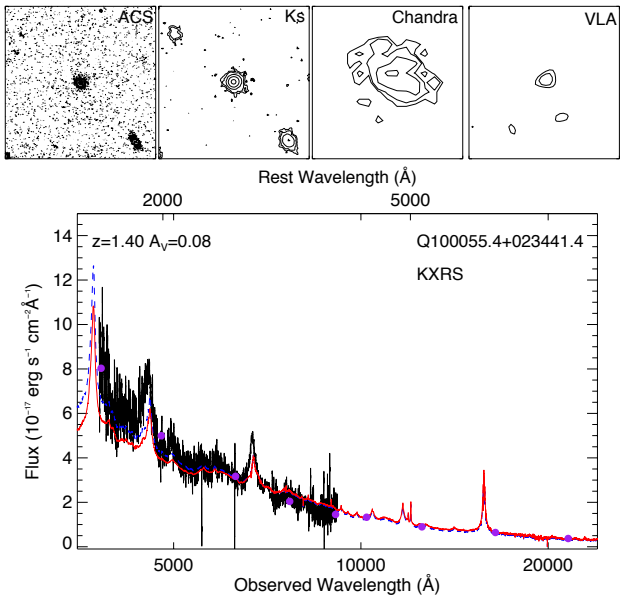

26: QSO_FAINT, SERENDIP_BLUE

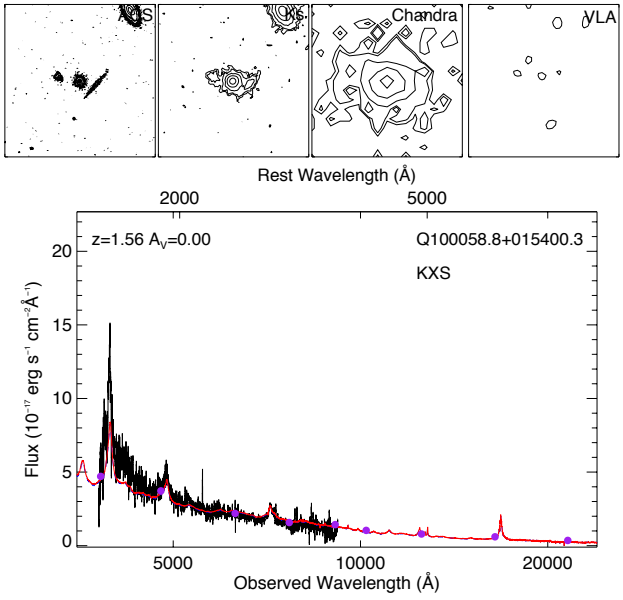

27: QSO_FAINT, SERENDIP_BLUE

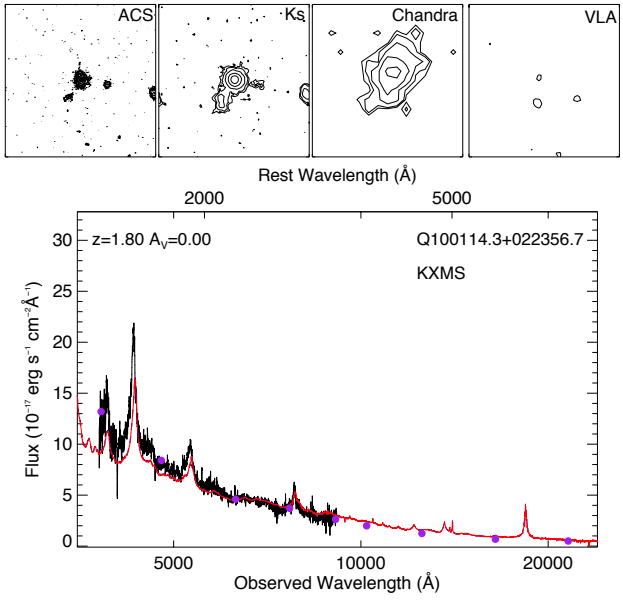

28: SERENDIP_BLUE, QSO_SKIRT

Fig. 4: *Continued*

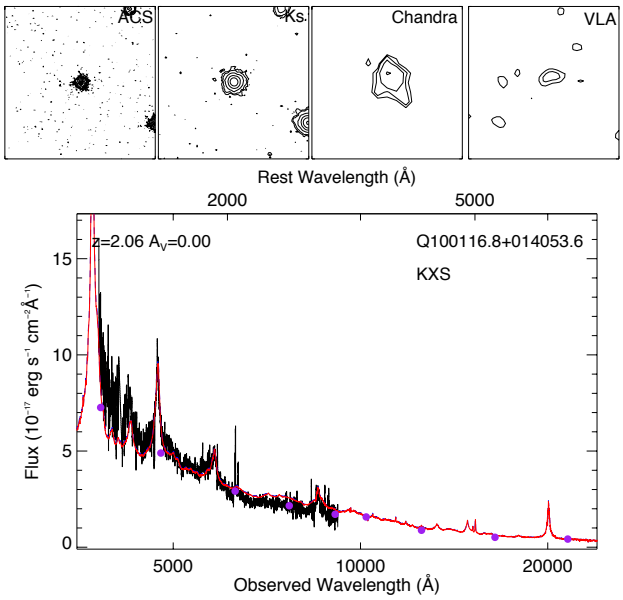

29: QSO_FAINT, SERENDIP_BLUE

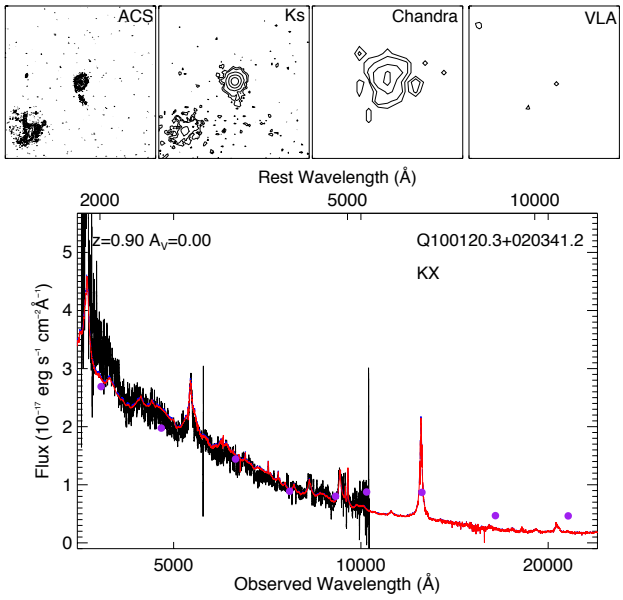

30: CHANDRAv1

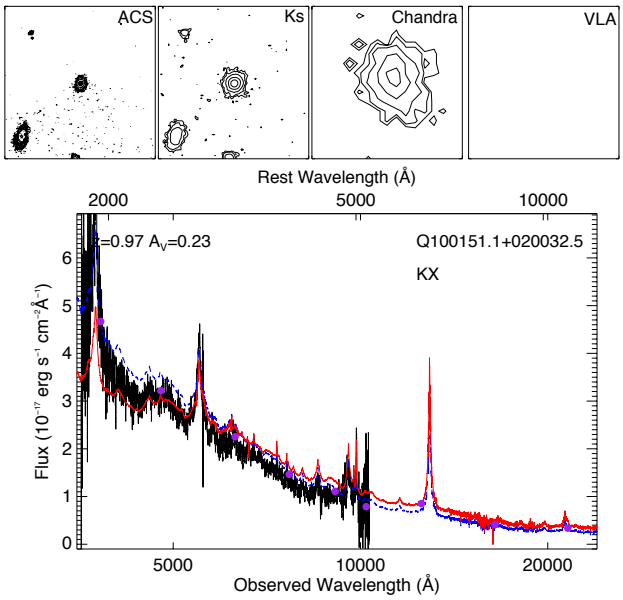

#31: CHANDRAv1

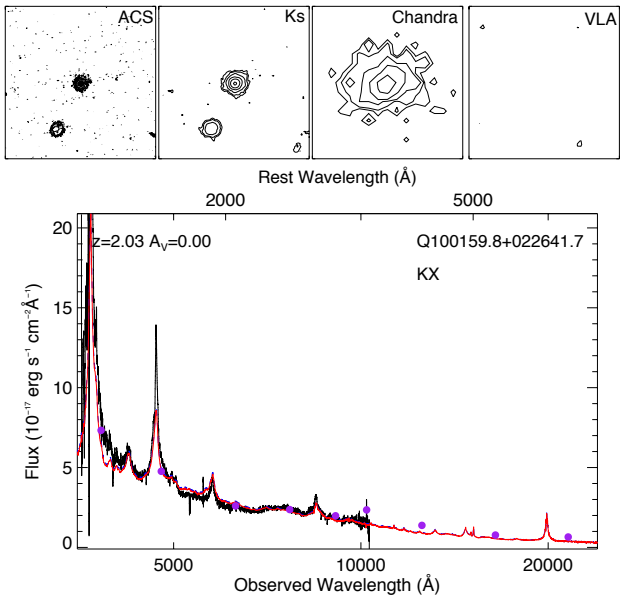

32: XMMBRIGHT

Fig. 3: *Continued*

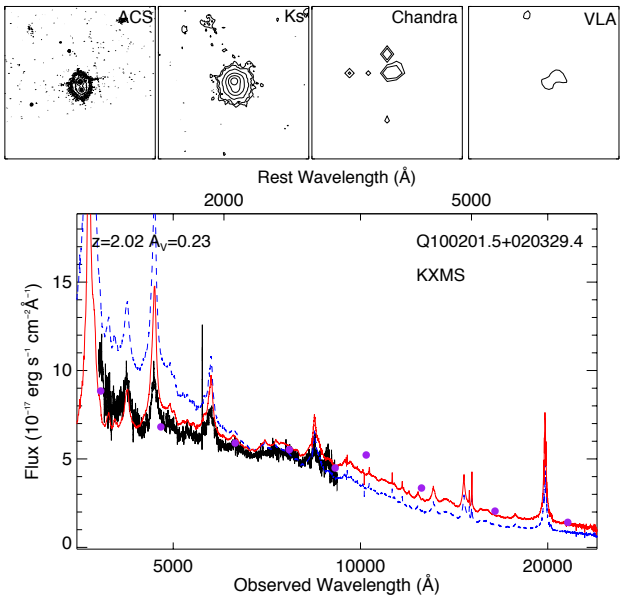

33: SERENDIP_BLUE, QSO_SKIRT

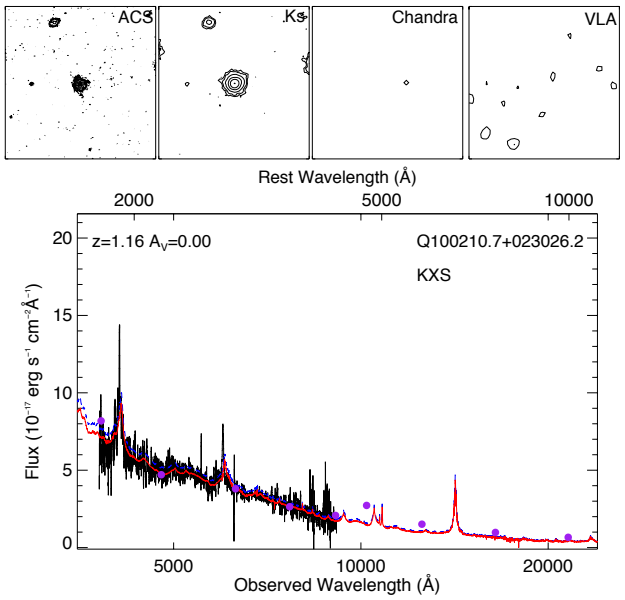

34: QSO_FAINT, SERENDIP_BLUE.

Appendix C

A study of purely astrometric selection of extragalactic point sources with Gaia, Astronomy & Astrophysics, Vol. 578, A91 (2015). Authors: Heintz, K. E., Fynbo, J. P U. & Høg, E.

Co-author statement:
E. Høg and J. Fynbo came up with the idea of examining the feasibility of selecting quasars, using the future measurements of the *Gaia* satellite. I did all the work myself with great guidance from J. Fynbo (in particular with the IDL part) and E. Høg on the mathematical formulations and where to obtain the necessary data. I have written the whole text and produced all the figures. The co-authors and the referee have contributed at the level of commenting on the text and figures and making suggestions for changes of these.

A&A 578, A91 (2015)
DOI: 10.1051/0004-6361/201526038

Astronomy & Astrophysics

A study of purely astrometric selection of extragalactic point sources with *Gaia*

K. E. Heintz[1], J. P. U. Fynbo[1], and E. Høg[2]

[1] Dark Cosmology Centre, Niels Bohr Institute, Copenhagen University, Juliane Maries Vej 30, 2100 Copenhagen O, Denmark
e-mail: heintz@dark-cosmology.dk
[2] Niels Bohr Institute, Copenhagen University, Juliane Maries Vej 30, 2100 Copenhagen O, Denmark

Received 6 March 2015 / Accepted 11 May 2015

ABSTRACT

Context. Selection of extragalactic point sources, e.g., quasi-stellar objects (QSOs), is often hampered by significant selection effects causing existing samples to have rather complex selection functions.
Aims. We explore whether a purely astrometric selection of extragalactic point sources, e.g., QSOs, is feasible with the ongoing *Gaia* mission. The idea has been discussed in the context of *Gaia*, but it is the first time quantified numbers have been given. This kind of selection would also be interesting as it would be unbiased in terms of colors of the targets and hence would allow selection also with colors in the stellar sequence.
Methods. We have analyzed a total of 18 representative regions of the sky using GUMS, the simulator prepared for ESAs *Gaia* mission, both in the range of $12 \leq G \leq 20$ mag and $12 \leq G \leq 18$ mag. For each region we determine the density of apparently stationary stellar sources, i.e., sources for which *Gaia* cannot measure a significant proper motion. The density is contrasted with the density of extragalactic point sources, e.g., QSOs, to establish in which celestial directions a pure astrometric selection is feasible.
Results. When targeting regions at galactic latitude $|b| \geq 30^{\rm o}$ the ratio of QSOs to apparently stationary stars is above 50% and when observing toward the poles, the fraction of QSOs goes up to about ~80%. We show that the proper motions from the proposed *Gaia* successor mission in about 20 years would dramatically improve these results at all latitudes. Detection of QSOs solely from zero proper motion, unbiased by any assumptions on spectra, might lead to the discovery of new types of QSOs or new classes of extragalactic point sources.

Key words. quasars: general – astrometry – proper motions

1. Introduction

Since their discovery in the early 1960s (Schmidt 1963) numerous surveys for quasi-stellar objects (QSOs) have been carried out and the number of known QSOs now count hundreds of thousands. To have a complete understanding of supermassive black hole formation and evolution, it is desirable to select QSO samples in several different ways to be less constrained by selection effects.

The incompleteness of QSO samples based on selection by optical photometry has been studied intensively for many years (see, e.g., Richards et al. 2004, for a color selection of QSOs from the SDSS survey), and it is now well established that these samples miss a substantial number of, in particular, dust-reddened QSOs (see, e.g., Krawczyk et al. 2015, for a recent study).

To examine the feasibility of this approach, we first need to determine the contamination by the stars in our galaxy. To accomplish this we analyze how many stars will be selected by the zero proper motion criterion and toward which galactic coordinates the problem of stellar contamination will be most severe.

To describe this, we have structured the paper as follows. We start with a brief description of the *Gaia* mission and show the expected errors on proper motion from this mission and the usefulness of the soon to be obtained highly accurate astrometric measurements in Sect. 2. To get a hint about these future data, we have used extracts from a catalog of 1.6 billion stars generated for the *Gaia* mission, the so-called *Gaia* Universe Model Snapshot (GUMS), which is also briefly described in Sect. 2. In Sect. 3 and 4 we discuss the results of this analysis and thereby conclude on the feasibility of this new approach.

In the analysis we not only consider what we can accomplish with the *Gaia* mission alone, but also with proper motions having ten times smaller errors that from *Gaia*. This accuracy can be obtained by a combination of positions from *Gaia* and from another all-sky astrometric space mission in 20 years with similar errors on positions as *Gaia*; in fact, this would be the only feasible way to obtain this kind of accuracy. In the following, we refer to such a second mission as a "*Gaia* successor".

2. Simulated *Gaia* data

The *Gaia* mission, launched by ESA in December 2013, is a very powerful astrometric mission that is scheduled to make a three-dimensional map of our galaxy, and provide an unprecedented measurement of positions, proper motions, and parallaxes to more than one billion stellar systems to a limit in the G-band of 20 mag during its five-six years mission lifetime (de Bruijne 2012).

2.1. GUMS

Gaia is expected to transmit close to 150 terabytes of raw data, therefore, preparation for acquiring this amount of data is essential (Luri et al. 2014). Hence, the *Gaia* Data Processing and

Analysis Consortium (DPAC) has produced a set of simulators, including the *Gaia* Object Generator (GOG), which provides simulations of number counts and lists of observable objects and is designed to simulate catalog data (see, e.g., Robin et al. 2012).

A basic component of the *Gaia* simulator is its Universe Model (UM) from Robin et al. (2003, 2004). This model is capable of simulating almost every object down to *Gaia*'s limiting magnitude of $G = 20$ mag, both for galactic and extra-galactic objects (Luri et al. 2014). The *Gaia* simulator combined with the Universe model is then supposed to show a snapshot of the potentially observable objects by *Gaia*, thereby called the *Gaia* Universe Model Snapshot (GUMS). See especially Sect. 3 in Robin et al. (2012) for a full description of the stellar content.

We have used the extracts from this catalog of 1.6 billion stars, which have been generated by GUMS and can be obtained via the vizier website[1]. This has enabled us to derive precise numbers for the expected stellar contamination and the probability of separating QSOs and other extragalactic point sources from galactic sources.

2.2. Expected Gaia errors

We assumed the standard errors for a five year mission as expected before the launch of *Gaia*. These errors and the signal-to-noise ratio, S/N, are calculated as a function of the apparent magnitude G, which is approximately equal to the visual magnitude V. The following formulae are taken from de Bruijne (2012)[2]:

$$
\begin{aligned}
&z = 10^{(0.4\cdot(G-15))}, \text{ for } G > 12 \text{ mag}\\
&\sigma_\pi\ [\mu\text{as}] = \left(9.3 + 658.1\cdot z + 4.568\cdot z^2\right)^{1/2}\\
&\qquad\qquad \times\ [0.986 + (1-0.986)\cdot(V - I_C)]\,,\\
&\sigma_\mu\ [\mu\text{as yr}^{-1}] = 0.526\cdot\sigma_\pi, \quad S/N = \frac{\mu}{\sigma_\mu},
\end{aligned}
\tag{1}
$$

where G is the G-band magnitude, σ_π denotes the error on the parallax measurement, σ_μ is the error on the proper motion, and for an unreddened G2V star, we can set $(V - I_C) = 0.75$ (de Bruijne 2012). For $G = 20$ mag, this yields a lower limit in σ_μ of about 0.3 mas/yr, and for $G = 18$ mag, it is close to 0.1 mas/yr.

3. Results

It is now possible to determine the expected contamination from stars with proper motions below the detection limit of *Gaia*.

In Fig. 1 we plotted the expected number of $G \le 20$ stars per square degree with proper motion less than μ as a function of μ in seven directions, of a total of 18 directions, as listed in Tables 1 to 4 of Sect. 3. For the plots of varying galactic latitude, b, we extracted a larger area of the sky of 3×3 or 5×5 deg^2, and afterward divided the total number of stars by 9 or 25, respectively, to normalize the y-axis since the 1×1 deg^2 area away from the galactic plane has a low density of stars.

To be conservative, we consider stars with proper motions measured with $S/N \le 5$ as possible contaminants. We also calculate the number of sources with $S/N \le 0.5$, which is the equivalent of $S/N \le 5$ for a data set based on *Gaia* plus a successor mission similar to *Gaia* operating about 20 years from now.

[1] http://vizier.u-strasbg.fr/viz-bin/VizieR-3

[2] Functionslistedat:http://www.cosmos.esa.int/web/gaia/science-performance

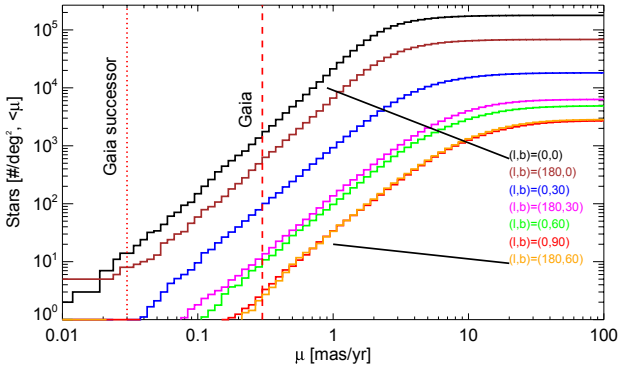

Fig. 1. Number of stars with a magnitude range in the G-band of $12 \le G \le 20$ per square degree versus the cumulative distribution of each of their proper motion as seen on the sky, listed in seven directions as given by the galactic coordinates (l, b). The values (l, b) are listed at the right in the same sequence as the curves are seen. The red dashed line at $\mu = 0.3$ mas/yr represents the estimated error of the proper motions from *Gaia* at $G = 20$ mag. The red dotted line at $\mu = 0.03$ mas/yr represents the estimated error of the proper motions derived from the positions obtained from *Gaia* and the proposed *Gaia* successor mission, also at $G = 20$ mag.

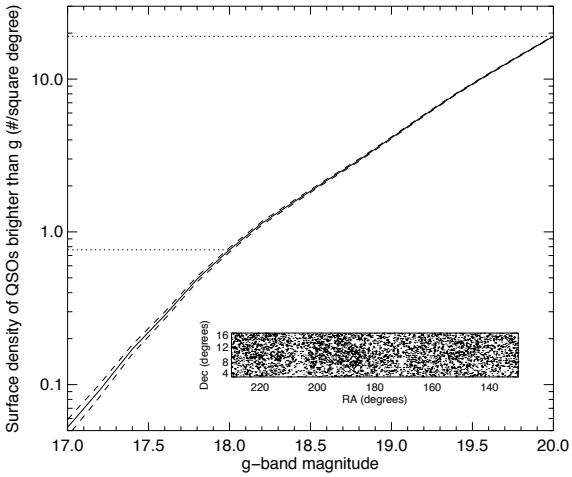

Fig. 2. Surface densities of QSOs at given magnitudes in the g-band from the BOSS catalog. The insert shows the celestial region we used to generate the plot, i.e., a region well away from the Galactic disk where the distribution is uniform. The two dotted lines show the QSO surface density for one square degree, which is found to be 19 and 0.76 when observing at a limited range of $g = 20$ and $g = 18$ mag, respectively. In the present context, we consider the bands g and G to be equivalent, although the effective wavelengths differ by about 100 nm. They vary greatly with spectral type, however, because both bands are very wide.

This kind of *Gaia* successor mission was proposed in May 2013 by Høg (2014a) as being crucial for the astrometric foundation of astrophysics and the proposal was further refined in Høg (2014b).

We show the results found when analyzing how many of the total number of stars in each direction in one square degree have $S/N \le 5$ and $S/N \le 0.5$, both for $G \le 20$ mag and $G \le 18$ mag. This is shown graphically in Fig. 3, whereas the listed values are shown in Tables 1–4. The points for $G = 20$ mag, shown with black points in Figs. 3, show that the number of contaminating stars is reduced by a factor 100 with the proposed *Gaia* successor mission, precisely what was expected with 10 times smaller errors of proper motions in the two celestial coordinates.

Table 1. Results of data when only varying l, in the galactic plane for $G \leq 20$ mag.

Longitude [deg]	180	135	90	45	0	315	270	225
$N_{\rm tot}$	68 375	86 061	210 314	200 141	178 152	196 128	26 844	95 276
$N_{\mu,0.3}$	2254	12631	1007	991	6917	358	61	9712
$N_{\rm SN,5}$	604	3991	258	238	1616	101	10	3072
$N_{\rm SN,0.5}$	9	54	2	6	12	2	0	36
$N_{\rm QSO}/(N_{\rm SN,5}+N_{\rm QSO})$	0.030	0.005	0.069	0.074	0.012	0.158	0.655	0.006
$N_{\rm QSO}/(N_{\rm SN,0.5}+N_{\rm QSO})$	0.679	0.260	0.905	0.760	0.613	0.905	1	0.345

Table 2. Results of data when only varying b, observing away from the galactic plane for $G \leq 20$ mag, beginning at anticenter.

Latitude [deg]	(180, 0)	+30	+60	+90	+60	+30	(0, 0)	–30	–60	–90	–60	–30
$N_{\rm tot}$	68 375	6323	2851	2720	4889	18 145	178 152	25 244	5174	2852	2953	5511
$N_{\mu,0.3}$	2254	48.7	13.1	12.0	38.9	345.3	6917	544	32.11	11.52	12.11	36
$N_{\rm SN,5}$	604	18.76	4.80	4.96	15.44	159	1616	257	12.89	4.88	5.33	10.33
$N_{\rm SN,0.5}$	9	0.16	0.08	0	0.44	1.44	12	2	0.22	0.08	0.11	0
$N_{\rm QSO}/(N_{\rm SN,5}+N_{\rm QSO})$	0.030	0.503	0.798	0.793	0.552	0.107	0.012	0.069	0.596	0.796	0.781	0.648
$N_{\rm QSO}/(N_{\rm SN,0.5}+N_{\rm QSO})$	0.679	0.992	0.996	1	0.977	0.930	0.613	0.905	0.989	0.996	0.994	1

Table 3. Results of data when only varying l, in the galactic plane for $G \leq 18$ mag.

Longitude [deg]	180	135	90	45	0	315	270	225
$N_{\rm tot}$	40 156	48 071	110 018	115 174	107 542	113 205	16 761	53 235
$N_{\mu,0.1}$	125	771	77	65	426	27	4	598
$N_{\rm SN,5}$	91	608	61	53	356	20	1	481
$N_{\rm SN,0.5}$	0	9	0	0	3	0	0	11
$N_{\rm QSO}/(N_{\rm SN,5}+N_{\rm QSO})$	0.008	0.001	0.012	0.014	0.002	0.037	0.432	0.002
$N_{\rm QSO}/(N_{\rm SN,0.5}+N_{\rm QSO})$	1	0.078	1	1	0.202	1	1	0.065

Table 4. Results of data when only varying b, observing away from the galactic plane for $G \leq 18$ mag, beginning at anticenter.

Latitude [deg]	(180, 0)	+30	+60	+90	+60	+30	(0,0)	–30	–60	–90	–60	–30
$N_{\rm tot}$	40 156	3761	1673	1542	2564	7938	107 542	10 828	2731	1629	1744	3360
$N_{\mu,0.1}$	125	2.76	0.44	0.52	1.22	10.33	426	12	1	0.20	0.33	1.78
$N_{\rm SN,5}$	91	2.56	0.24	0.48	1.22	8.33	356	4	0.67	0.44	0.33	1.11
$N_{\rm SN,0.5}$	0	0	0	0	0.33	0	3	0	0	0	0	0
$N_{\rm QSO}/(N_{\rm SN,5}+N_{\rm QSO})$	0.008	0.229	0.760	0.613	0.384	0.084	0.002	0.160	0.531	0.633	0.697	0.406
$N_{\rm QSO}/(N_{\rm SN,0.5}+N_{\rm QSO})$	1	1	1	1	0.697	1	0.202	1	1	1	1	1

The surface density of known QSOs at each limiting magnitude from the BOSS catalog (see, e.g., Pâris et al. 2012, for the full catalog description) is plotted in Fig. 2. We plotted as a function of g-band magnitude as we do not have G-band magnitudes for the BOSS QSOs. The density of BOSS QSOs is shown as the two dotted lines (assuming $g \approx G$) in Fig. 3 to indicate the relative frequency of known QSOs and galactic stars for each pointing direction.

It can be concluded from Fig. 3 that when observing with *Gaia* at $G \leq 20$ mag, the probability that a point source with proper motion detected at less than 5σ is a QSO drops rapidly when observing below $|b| = 30^{\rm o}$. We have the highest probability to select a QSO with *Gaia* at $S/N \leq 5$ for $G \leq 20$ at $(l, b) = (180, 60)$ where, according to Table 2:

$$\frac{N_{\rm QSO}}{(N_{\rm QSO}+N_{\rm SN,5})} = 0.798 = 79.8\%. \quad (2)$$

The probability is just above 50% at $|b| = 30^{\rm o}$, which means that this way of selecting extragalactic point sources clearly is feasible. Also shown in Fig. 3 is that with a *Gaia* successor mission 20 years after the current *Gaia* mission the contamination from apparently stationary stars essentially would be eliminated.

When restricting the analysis to a brighter limiting magnitude of $G \leq 18$ instead, the contamination from apparently stationary stars is slightly higher. The first line of Tables 1 to 4 denotes the total number of stars per square degree in the listed direction. The next three lines show the number of stars with values lower than $\mu \leq 0.3$ mas/yr, $S/N \leq 5$ and $S/N \leq 0.5$, respectively. The final two lines shows the QSO fraction, when observing point sources in the limit of $S/N = 5$ and $S/N = 0.5$, respectively. The numbers in last line of Table 1 demonstrate that QSOs can be extracted with high probability at the longitudes 90, 270, and 315 degrees, even in the galactic plane, but these numbers do not take interstellar absorption into account.

4. Discussion and conclusions

We used the object simulator prepared for the *Gaia* mission, GUMS, to determine the expected contamination from galactic stars in a search for extragalactic point sources based on astrometric measurements from *Gaia*.

By analyzing GUMS, we determine the frequency of selecting a QSO based on the density inferred from BOSS against the background of apparently stationary stars. This provides a

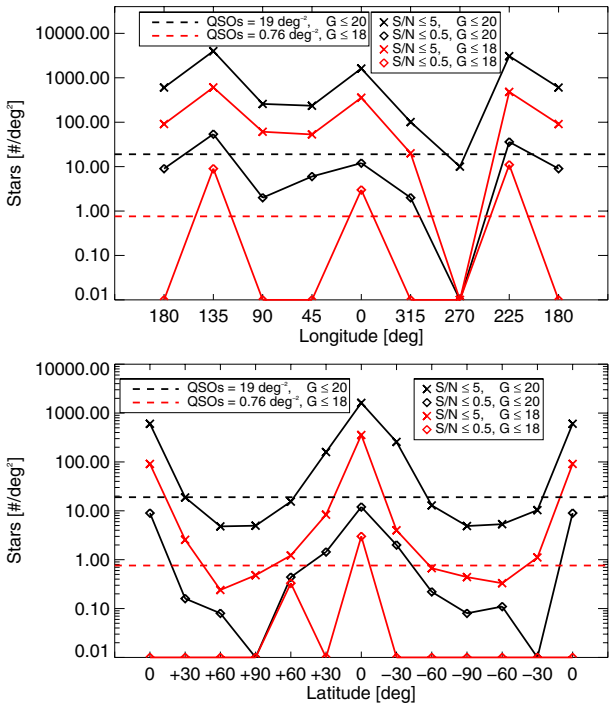

Fig. 3. *Top panel*: results of the analyzed stellar proper motions, when observing at $b = 0$ and varying galactic longitudes, with a $S/N \leq 5$ for *Gaia* (marked with crosses) and a $S/N \leq 0.5$ for a combination of *Gaia* and a proposed *Gaia* successor mission (marked with diamonds), both for $G \leq 20$ mag and $G \leq 18$ mag (shown with black and red lines, respectively). *Bottom panel*: results of the analyzed stellar proper motions, when observing at $b = 0$ and varying galactic latitudes, with a $S/N \leq 5$ for *Gaia* and a $S/N \leq 0.5$ for a combination of *Gaia* and a proposed *Gaia* successor mission, both for $G \leq 20$ mag and $G \leq 18$ mag (with same use of crosses, diamonds, black, and red lines as in the *top panel*). Black and red dashed lines represent the number of QSOs at $G = 20$ and $G = 18$ mag, respectively, from the BOSS catalog for comparison.

conservative estimate of the relative number of QSOs and apparent stationary stars, as the BOSS survey does not contain all QSOs down to the flux limit of the survey (examples of missed QSOs can be found in Fynbo et al. 2013, Krogager et al. 2015).

At $|b| > 30^{\circ}$ the ratio of QSOs relative to stars is above 50% when observing down to $G \leq 20$ mag. When decreasing the magnitude range to $G \leq 18$ mag a lower number of stellar contamination is obtained but the relative QSO surface density in that magnitude range decreases as well, yielding a sightly higher level of stellar contamination. When observing below $|b| = 30^{\circ}$, close to the galactic plane, the contamination increases rapidly.

With a *Gaia* successor mission, i.e., a mission similar to *Gaia* launched in about 20 years from now, the standard error on the measurement of the proper motions would decrease by about a factor of ten, resulting in 100 times improvement in the ability to select extragalactic point sources against the background of apparently stationary stars.

Since the method we analyze here is unbiased in terms of color, this method has the potential to discover new, exotic types of QSOs and even in principle new classes of extragalactic point sources. Also, this method would allow the construction of an unbiased QSO sample limited only in its flux limit. This would be very valuable for adressing several issues, e.g., the true metallicity distribution of foreground damped Lyman-α absorber galaxies (e.g., Fall & Pei 1993) or the redshift distribution of broad absorption line QSOs (Saturni et al. 2015).

We also note that the astrometric information from *Gaia* will be very useful to remove contaminating stellar sources from other more targeted searches for red QSOs. Often such contaminating sources are M-dwarfs, which due to their small distances should have significant proper motions.

We assumed that QSOs are point sources, but we are aware that this is not always the case. Variability of a QSO with changing centres could introduce observed proper motions. We are aware that proper motions of quasars may be significant. In the catalog by Titov et al. (2011) with 555 radio sources, the motions are typically 0.1 mas/yr and some even 1 mas/yr, but the 40 most frequently observed sources shown in Fig. 2 of the paper all have much smaller motions of less than 0.025 mas/yr. One can argue that optical QSOs should be more stable than radio sources, more compact, etc., but we do not know for sure until *Gaia* data become available.

Acknowledgements. The data from GUMS, the *Gaia* Universe Model Snapshot, were aquired with kind help from Carine Babusiaux and they were used for simulation of observations as expected from *Gaia*. We thank Coryn Bailer-Jones, Sergei Klioner, and Palle Møller for helpful comments. The Dark Cosmology Centre is funded by the DNRF. The research leading to these results has received funding from the European Research Council under the European Union's Seventh Framework Program (FP7/2007-2013)/ERC Grant agreement No. EGGS-278202.

References

de Bruijne, J. H. J. 2012, Ap&SS, 341, 31
Fall, S. M., & Pei, Y. C. 1993, ApJ, 402, 479
Fynbo, J. P. U., Krogager, J.-K., Venemans, B., et al. 2013, ApJS, 204, 6
Høg, E. 2014a, ArXiv e-prints [arXiv:1408.3299]
Høg, E. 2014b, ArXiv e-prints [arXiv:1408.2122]
Krawczyk, C. M., Richards, G. T., Gallagher, S. C., et al. 2015, AJ, 149, 203
Krogager, J.-K., Geier, S., Fynbo, J. P. U., et al. 2015, ApJS, 217, 5
Luri, X., Palmer, M., Arenou, F., et al. 2014, A&A, 566, A119
Pâris, I., Petitjean, P., Aubourg, É., et al. 2012, A&A, 548, A66
Richards, G. T., Nichol, R. C., Gray, A. G., et al. 2004, ApJS, 155, 257
Robin, A. C., Reylé, C., Derrière, S., & Picaud, S. 2003, A&A, 409, 523
Robin, A. C., Reylé, C., Derrière, S., & Picaud, S. 2004, A&A, 416, 157
Robin, A. C., Luri, X., Reylé, C., et al. 2012, A&A, 543, A100
Saturni, F. G., Møller, P., Freudling, W., et al. 2015, MNRAS, submitted
Schmidt, M. 1963, Nature, 197, 1040
Titov, O., Lambert, S. B., & Gontier, A.-M. 2011, A&A, 529, A91

Bibliography

Aihara, H., Allende Prieto, C., An, D., et al. 2011, Astrophysical Journal, Supplement, 193, 29

Arnaboldi, M., Neeser, M. J., Parker, L. C., et al. 2007, The Messenger, 127, 28

Arp, H. C., Khachikian, E. Y., Lynds, C. R., & Weedman, D. W. 1968, Astrophysical Journal, Letters, 152, L103

Assef, R. J., Kochanek, C. S., Brodwin, M., et al. 2010, Astrophysical Journal, 713, 970

Assef, R. J., Stern, D., Kochanek, C. S., et al. 2013, Astrophysical Journal, 772, 26

Banerji, M., McMahon, R. G., Hewett, P. C., et al. 2012, Monthly Notices of the Royal Astronomical Society, 427, 2275

Becker, R. H., White, R. L., & Helfand, D. J. 1995, Astrophysical Journal, 450, 559

Boyle, B. J., Croom, S. M., Smith, R. J., et al. 2001, in Deep Fields, ed. S. Cristiani, A. Renzini, & R. E. Williams, 282

Brandt, W. N. & Hasinger, G. 2005, Annual Review of Astronomy and Astrophysics, 43, 827

Brunzendorf, J. & Meusinger, H. 2001, Astronomy and Astrophysics, 373, 38

Brunzendorf, J. & Meusinger, H. 2002, Astronomy and Astrophysics, 390, 879

Brusa, M., Civano, F., Comastri, A., et al. 2010, Astrophysical Journal, 716, 348

Capak, P., Aussel, H., Ajiki, M., et al. 2007, Astrophysical Journal, Supplement, 172, 99

Cappelluti, N., Brusa, M., Hasinger, G., et al. 2009, Astronomy and Astrophysics, 497, 635

Civano, F., Elvis, M., Brusa, M., et al. 2012, Astrophysical Journal, Supplement, 201, 30

Croom, S. M., Smith, R. J., Boyle, B. J., et al. 2004, Monthly Notices of the Royal Astronomical Society, 349, 1397

Croom, S. M., Warren, S. J., & Glazebrook, K. 2001, Monthly Notices of the Royal Astronomical Society, 328, 150

Cutri, R. M., Nelson, B. O., Francis, P. J., & Smith, P. S. 2002, in Astronomical Society of the Pacific Conference Series, Vol. 284, IAU Colloq. 184: AGN Surveys, ed. R. F. Green, E. Y. Khachikian, & D. B. Sanders, 127

Cutri, R. M., Wright, E. L., Conrow, T., et al. 2013, Explanatory Supplement to the AllWISE Data Release Products, Tech. rep.

Dawson, K. S., Schlegel, D. J., Ahn, C. P., et al. 2013, Astronomical Journal, 145, 10

de Bruijne, J. H. J. 2012, Astrophysics and Space Science, 341, 31

de Grijp, M. H. K., Lub, J., & Miley, G. K. 1987, Astronomy and Astrophysics, Supplement, 70, 95

de Jong, J. T. A., Verdoes Kleijn, G. A., Boxhoorn, D. R., et al. 2015, Astronomy and Astrophysics, 582, A62

Donley, J. L., Koekemoer, A. M., Brusa, M., et al. 2012, Astrophysical Journal, 748, 142

Elvis, M., Civano, F., Vignali, C., et al. 2009, Astrophysical Journal, Supplement, 184, 158

Fan, X. 1999, Astronomical Journal, 117, 2528

Fynbo, J. P. U., Krogager, J.-K., Venemans, B., et al. 2013, Astrophysical Journal, Supplement, 204, 6

Fynbo, J. P. U., Ledoux, C., Noterdaeme, P., et al. 2011, Monthly Notices of the Royal Astronomical Society, 413, 2481

Gillessen, S., Eisenhauer, F., Trippe, S., et al. 2009, Astrophysical Journal, 692, 1075

Glikman, E., Helfand, D. J., White, R. L., et al. 2007, Astrophysical Journal, 667, 673

Glikman, E., Urrutia, T., Lacy, M., et al. 2012, Astrophysical Journal, 757, 51

Glikman, E., Urrutia, T., Lacy, M., et al. 2013, Astrophysical Journal, 778, 127

Gordon, K. D., Clayton, G. C., Misselt, K. A., Landolt, A. U., & Wolff, M. J. 2003, Astrophysical Journal, 594, 279

Graham, M. J., Djorgovski, S. G., Drake, A. J., et al. 2014, Monthly Notices of the Royal Astronomical Society, 439, 703

Grazian, A., Cristiani, S., D'Odorico, V., Omizzolo, A., & Pizzella, A. 2000, Astronomical Journal, 119, 2540

Green, R. F., Schmidt, M., & Liebert, J. 1986, Astrophysical Journal, Supplement, 61, 305

Greenstein, J. L. & Matthews, T., A. 1963, Nature, 197, 1041

Gregg, M. D., Lacy, M., White, R. L., et al. 2002, Astrophysical Journal, 564, 133

Hasinger, G., Cappelluti, N., Brunner, H., et al. 2007, Astrophysical Journal, Supplement, 172, 29

Heintz, K. E., Fynbo, J. P. U., & Høg, E. 2015, Astronomy and Astrophysics, 578, A91

Hewett, P., Irwin, M., Bunclark, P., et al. 1984, in Astrophysics and Space Science Library, Vol. 110, IAU Colloq. 78: Astronomy with Schmidt-Type Telescopes, ed. M. Capaccioli, 137

Hewett, P. C., Warren, S. J., Leggett, S. K., & Hodgkin, S. T. 2006, Monthly Notices of the Royal Astronomical Society, 367, 454

Hopkins, P. F., Strauss, M. A., Hall, P. B., et al. 2004, Astronomical Journal, 128, 1112

Hubble, E. P. 1925, Astrophysical Journal, 62

Ivezić, Ž., Menou, K., Knapp, G. R., et al. 2002, Astronomical Journal, 124, 2364

Jansen, F., Lumb, D., Altieri, B., et al. 2001, Astronomy and Astrophysics, 365, L1

Kaplan, K. F., Prochaska, J. X., Herbert-Fort, S., Ellison, S. L., & Dessauges-Zavadsky, M. 2010, Publications of the ASP, 122, 619

Koo, D. C. & Kron, R. G. 1988, Astrophysical Journal, 325, 92

Krogager, J.-K. 2016, ArXiv e-prints [[arXiv]1604.06230]

Krogager, J.-K., Fynbo, J. P. U., Noterdaeme, P., et al. 2016, Monthly Notices of the Royal Astronomical Society, 455, 2698

Krogager, J.-K., Geier, S., Fynbo, J. P. U., et al. 2015, Astrophysical Journal, Supplement, 217, 5

Lacy, M., Petric, A. O., Sajina, A., et al. 2007, Astronomical Journal, 133, 186

Lacy, M., Storrie-Lombardi, L. J., Sajina, A., et al. 2004, Astrophysical Journal, Supplement, 154, 166

Lawrence, A., Warren, S. J., Almaini, O., et al. 2007, Monthly Notices of the Royal Astronomical Society, 379, 1599

Low, J. & Kleinmann, D. E. 1968, Astronomical Journal, 73, 868

Lynden-Bell, D. 1969, Nature, 223, 690

Maddox, N., Hewett, P. C., Péroux, C., Nestor, D. B., & Wisotzki, L. 2012, Monthly Notices of the Royal Astronomical Society, 424, 2876

Maddox, N., Hewett, P. C., Warren, S. J., & Croom, S. M. 2008, Monthly Notices of the Royal Astronomical Society, 386, 1605

Mateos, S., Alonso-Herrero, A., Carrera, F. J., et al. 2012, Monthly Notices of the Royal Astronomical Society, 426, 3271

McCracken, H. J., Milvang-Jensen, B., Dunlop, J., et al. 2012, Astronomy and Astrophysics, 544, A156

Meusinger, H., Brunzendorf, J., & Laget, M. 2003, Astronomische Nachrichten, 324, 474

Mo, H., van den Bosch, F. C., & White, S. 2010, Galaxy Formation and Evolution

Momjian, E., Carilli, C. L., Walter, F., & Venemans, B. 2014, Astronomical Journal, 147, 6

Nikutta, R., Hunt-Walker, N., Nenkova, M., Ivezić, Ž., & Elitzur, M. 2014, Monthly Notices of the Royal Astronomical Society, 442, 3361

Noterdaeme, P., Petitjean, P., Carithers, W. C., et al. 2012, Astronomy and Astrophysics, 547, L1

Noterdaeme, P., Petitjean, P., Ledoux, C., et al. 2010, Astronomy and Astrophysics, 523, A80

Noterdaeme, P., Petitjean, P., Ledoux, C., & Srianand, R. 2009, Astronomy and Astrophysics, 505, 1087

Oke, J. B. 1974, Astrophysical Journal, Supplement, 27, 21

Osmer, P. S. & Hewett, P. C. 1991, Astrophysical Journal, Supplement, 75, 273

Pâris, I., Petitjean, P., Aubourg, É., et al. 2014, Astronomy and Astrophysics, 563, A54

Pei, Y. C. 1992, Astrophysical Journal, 395, 130

Peterson, B. M. 1997, An Introduction to Active Galactic Nuclei (Cambridge University Press)

Richards, G. T., Fan, X., Newberg, H. J., et al. 2002, Astronomical Journal, 123, 2945

Richards, G. T., Fan, X., Schneider, D. P., et al. 2001, Astronomical Journal, 121, 2308

Richards, G. T., Hall, P. B., Vanden Berk, D. E., et al. 2003, Astronomical Journal, 126, 1131

Ross, N. P., Hamann, F., Zakamska, N. L., et al. 2015, Monthly Notices of the Royal Astronomical Society, 453, 3932

Ross, N. P., Myers, A. D., Sheldon, E. S., et al. 2012, Astrophysical Journal, Supplement, 199, 3

Sadler, E. M., Jackson, C. A., Cannon, R. D., et al. 2002, Monthly Notices of the Royal Astronomical Society, 329, 227

Salpeter, E. E. 1964, Astrophysical Journal, 140, 796

Salvato, M., Hasinger, G., Ilbert, O., et al. 2009, Astrophysical Journal, 690, 1250

Salvato, M., Ilbert, O., Hasinger, G., et al. 2011, Astrophysical Journal, 742, 61

Salzer, J. J., Gronwall, C., Lipovetsky, V. A., et al. 2000, Astronomical Journal, 120, 80

Sandage, A. 1965, Astrophysical Journal, 141, 1560

Sandage, A. R. 1971, in Study Week on Nuclei of Galaxies, ed. D. J. K. O'Connell, 271

Sargent, W. L. W. 1970, Astrophysical Journal, 160, 405

Schlegel, D. J., Finkbeiner, D. P., & Davis, M. 1998, Astrophysical Journal, 500, 525

Schmidt, K. B., Marshall, P. J., Rix, H.-W., et al. 2010, Astrophysical Journal, 714, 1194

Schmidt, M. 1963, Nature, 197, 1040

Schmidt, M. & Green, R. F. 1983, Astrophysical Journal, 269, 352

Schmidt, M. & Matthews, T. A. 1964, Astrophysical Journal, 139, 781

Schneider, D. P., Richards, G. T., Hall, P. B., et al. 2010, Astronomical Journal, 139, 2360

Scoville, N., Aussel, H., Brusa, M., et al. 2007, Astrophysical Journal, Supplement, 172, 1

Secrest, N. J., Dudik, R. P., Dorland, B. N., et al. 2015, Astrophysical Journal, Supplement, 221, 12

Selsing, J., Fynbo, J. P. U., Christensen, L., & Krogager, J.-K. 2016, Astronomy and Astrophysics, 585, A87

Skrutskie, M. F., Cutri, R. M., Stiening, R., et al. 2006, Astronomical Journal, 131, 1163

Skrutskie, M. F., Schneider, S. E., Stiening, R., et al. 1997, in Astrophysics and Space Science Library, Vol. 210, The Impact of Large Scale Near-IR Sky Surveys, ed. F. Garzon, N. Epchtein, A. Omont, B. Burton, & P. Persi, 25

Stern, D., Assef, R. J., Benford, D. J., et al. 2012, Astrophysical Journal, 753, 30

Stern, D., Eisenhardt, P., Gorjian, V., et al. 2005, Astrophysical Journal, 631, 163

Urrutia, T., Becker, R. H., White, R. L., et al. 2009, Astrophysical Journal, 698, 1095

Usher, P. D. & Mitchell, K. J. 1978, Astrophysical Journal, 223, 1

van Dokkum, P. G. 2001, Publications of the ASP, 113, 1420

Veron, P. & Hawkins, M. R. S. 1995, Astronomy and Astrophysics, 296, 665

Wang, J.-G., Zhou, H.-Y., Ge, J., et al. 2012, Astrophysical Journal, 760, 42

Ward, M., Penston, M. V., Blades, J. C., & Turtle, A. J. 1980, Monthly Notices of the Royal Astronomical Society, 193, 563

Warren, S. J., Hewett, P. C., & Foltz, C. B. 2000, Monthly Notices of the Royal Astronomical Society, 312, 827

Webster, R. L., Francis, P. J., Petersont, B. A., Drinkwater, M. J., & Masci, F. J. 1995, Nature, 375, 469

Weisskopf, M. C., Brinkman, B., Canizares, C., et al. 2002, Publications of the ASP, 114, 1

Werner, M. W., Roellig, T. L., Low, F. J., et al. 2004, Astrophysical Journal, Supplement, 154, 1

White, R. L., Becker, R. H., Gregg, M. D., et al. 2000, Astrophysical Journal, Supplement, 126, 133

Wilson, A. S. 1979, Proceedings of the Royal Society of London Series A, 366, 461

Wolfe, A. M., Gawiser, E., & Prochaska, J. X. 2005, Annual Review of Astronomy and Astrophysics, 43, 861

Wright, E. L., Eisenhardt, P. R. M., Mainzer, A. K., et al. 2010, Astronomical Journal, 140, 1868

York, D. G., Adelman, J., Anderson, Jr., J. E., et al. 2000, Astronomical Journal, 120, 1579